MULTI-FREQUENCY FLUXGATE MAGNETIC FORCE MICROSCOPY

A THESIS

SUBMITTED TO THE DEPARTMENT OF PHYSICS

AND THE INSTITUTE OF ENGINEERING AND SCIENCE

OF BILKENT UNIVERSITY

IN PARTIAL FULFILLMENT OF THE REQUIREMENTS

FOR THE DEGREE OF

MASTER OF SCIENCE

By

Ozan Aktaş

September, 2008

I certify that I have read this thesis and that in my opinion it is fully adequate, in scope and in quality, as a thesis for the degree of Master of Science.

Assist. Prof. Dr. Mehmet Bayındır (Supervisor)

I certify that I have read this thesis and that in my opinion it is fully adequate, in scope and in quality, as a thesis for the degree of Master of Science.

R. Assist. Prof. Dr. Aykutlu Dâna (Co-Supervisor)

I certify that I have read this thesis and that in my opinion it is fully adequate, in scope and in quality, as a thesis for the degree of Master of Science.

Prof. Dr. Salim Çıracı

I certify that I have read this thesis and that in my opinion it is fully adequate, in scope and in quality, as a thesis for the degree of Master of Science.

Assist. Prof. Dr. M. Özgür Oktel

I certify that I have read this thesis and that in my opinion it is fully adequate, in scope and in quality, as a thesis for the degree of Master of Science.

Assist. Prof. Dr. Ali Kemal Okyay

Approved for the Institute of Engineering and Science:

Prof. Dr. Mehmet B. Baray
Director of the Institute Engineering and Science

ABSTRACT

MULTI-FREQUENCY FLUXGATE MAGNETIC FORCE MICROSCOPY

Ozan Aktaş
M.S. in Physics
Supervisor: Assist. Prof. Dr. Mehmet Bayındır
Co-supervisor: R. Assist. Prof. Dr. Aykutlu Dâna
September, 2008

In the recent years, progress in atomic force microscopy (AFM) led to the multifrequency imaging paradigm in which the cantilever-tip ensemble is simultaneously excited by several driving forces of different frequencies. By using multifrequency excitation, various interaction forces of different physical origin such as electronic interactions or chemical interactions can be simultaneously mapped along with topography. However, a multifrequency magnetic imaging technique has not been demonstrated yet. The difficulty in imaging magnetic forces using a multifrequency technique partly arises from difficulties in modulation of the magnetic tip-sample interaction. In the traditional unmodulated scheme, measurement of magnetic forces and elimination of coupling with other forces is obtained in a double pass measurement technique where topography and magnetic interactions are rapidly measured in successive scans with different tip-sample separations. This measurement scheme may suffer from thermal drifts or topographical artifacts. In this work, we consider a multifrequency magnetic imaging method which uses first resonant flexural mode for topography signal acquisition and second resonant flexural mode for measuring the magnetic interaction simultaneously. As in a fluxgate magnetometer, modulation of magnetic moment of nickel particles attached on the apex of AFM tip can be used to modulate the magnetic forces which are dependent on external DC fields through the nonlinear magnetic response of the nickel particles. Coupling strength can be varied by changing coil current or setpoint parameters of Magnetic Force Microscopy (MFM) system. Special MFM tips were fabricated by using Focused Ion Beam (FIB) and magnetically characterized for the purpose of multifrequency imaging. In this work, the use of such a nano-flux-gate system for simultaneous topographic and magnetic imaging is experimentally demonstrated. The excitation and detection scheme can be also used for high sensitivity cantilever magnetometry.

Keywords: Magnetic Force Microscopy (MFM), Multi-frequency Imaging, Fluxgate Magnetometry.

ÖZET

ÇOK FREKANSLI AKIGEÇİŞ MANYETİK KUVVET MİKROSKOPİSİ

Ozan Aktaş
Fizik, Yüksek Lisans
Tez Yöneticisi: Doç. Dr. Mehmet Bayındır
Yrd. Tez Yöneticisi: Yrd. Doç. Dr. Aykutlu Dâna
Eylül, 2008

Son yıllarda atomik kuvvet mikroskopisinde (AKM) ortaya çıkan gelişmeler, asılı uç sisteminin aynı anda farklı frekanslarda kuvvetler ile uyarıldığı çok frekanslı görüntüleme akımını doğurmuştur. Çok frekanslı uyarılma ile elektronik veya kimyasal etkileşimler gibi farklı fiziksel kökene sahip birçok etkileşim kuvvetleri yüzey topografisi ile aynı anda ölçülebilinir. Fakat, çok frekanslı manyetik görüntüleme tekniği ise henüz gösterilmemiştir. Çok frekanslı görüntüleme tekniği ile manyetik kuvvetlerin ölçülmesindeki zorluk kısmen manyetik uç ve örnek arasındaki etkileşimin modulasyonundaki zorluktan kaynaklanmaktadır. Geleneksel modulasyon kullanılmayan yöntemde, manyetik kuvvetlerin ölçülmesi ve diğer kuvvetlerden ayrılması farklı örnek-uç mesafelerinde arka arka yapılan iki geçişli tekniğin kullanılmasıyla olur. Fakat bu teknikte termal kayma ve topografik yan etkiler gibi sorunlarla karşılasabilinir. Bu çalışmada, yüzey topolojisi sinyalinin birinci salınımsal resonans moduyla, manyetik etkileşimin ise ikinci salınımsal resonans moduyla aynı anda elde edildiği çok frekanslı bir manyetik görüntüleme tekniği geliştirilmiştir. Akıgeçiş manyetometrisinde olduğu gibi AKM asılı ucu üzerine takılan nikel parçacıkların manyetik momentlerinin modulasyonu kullanılarak, nikel parçacıkların doğrusal olmayan manyetik tepkileri aracılığıyla harici DC alanlara baglı olan manyetik etkileşimlerin module edilmesi mümkündür. Sargı akımının veya Manyetik Kuvvet Mikroskopi (MKM) sistemin atanmış parametrelerinin değiştirilmesi ile etkileşmenin şiddeti değiştirilebilinir. Özel olarak MKM uçları FIB kullanılarak üretilmiş ve çok frekanslı görüntüleme amacı için manyetik olarak karakterize edilmiştir. Bu çalışmada böyle bir nano akgeçiş sisteminin ayn anda topografi ve manyetik görüntülemede kullanılması deneysel olarak gösterilmiştir. Kullanlan uyarma ve algılama yöntemi, yüksek duyarlıklı asılı uç manyetometrisinde kullanılması olanağını doğurmuştur.

Anahtar sözcükler: Manyetik Kuvvet Mikroskopisi (MKM), Çok frekanslı Görüntüleme, Akıgeçiş Manyetometrisi.

Acknowledgement

First of all, i would like to express my gratitude to my supervisors Assist. Prof. Dr. Mehmet Bayındır and R. Assist. Prof. Dr. Aykutlu Dâna for their instructive comments in the supervision of this thesis. I would like to thank especially Assist. Prof. Dr. Mehmet Bayındır for his motivation and guidance during my graduate study and my co-supervisor R. Assist. Prof. Aykutlu Dâna for sharing his deep experience on AFM techniques and innovative thinking.

I would like to thank some engineers of Institute of Materials Science and Nanotechnology (UNAM): A. Koray Mızrak for the fabrication of special MFM tips with FIB system, Emre Tanır for TEM imaging and Burkan Kaplan for his help with AFM system.

I would like to thank my friends Hasan Güner, M.Kurtuluş Abak, Sencer Ayas, Özlem Yeşilyurt and Dr. Abdullah Tülek not only for their help in lab but also their friendship and kindness they showed to me during my stay in Bilkent University.

I would like to thank Dr. Mecit Yaman for reviewing my thesis.

I would like to thank my commander Captain Çetin A. Akdoğan at 5^{th} Main Maintanance Command Center for his kindness and support for my graduate study.

I appreciate The Scientific and Technological Research Council of Turkey, TUBITAK-BIDEB for the financial support during my graduate study.

I especially would like to thank Prof. Dr. Salim Çıraçı, director of Materials Science and Nanotechnology Institute (UNAM), for giving us the opportunity to study at UNAM and to benefit from all equipments for my thesis.

Finally, I would like to thank my family for their support and belief in me to success.

Contents

List of Figures

List of Tables

Chapter 1

Introduction

1.1 Motivation

Nanomagnetism is a current area of research today. In the past, using magnetometers such as Vibrating Sample Magnetometer [1] only average magnetization of samples could be measured, but after the invention of techniques such as Magnetic Force Microscopy (MFM) [2], Scanning Hall Microscopy [3], Scanning SQUID Microscopy [4] micro and nano scale magnetism are no more out of reach of the researchers. By using these new tools, investigation of ultra thin films or single domain magnetic particles is expected to pave the way for potential applications of data storage mediums [5], spintronics [6], Magnetic Resonance Force Imaging(MRFI) [7].

After its first demostration in 1987 [2], MFM was extensively used for the observation of magnetic domain patterns, investigation of data storage mediums such as thin films with perpendicular magnetic anisotropy or patterned magnetic nanoparticle arrays, and also for vortex manipulation in superconductors at low temperatures. Actually MFM is an offspring of a more general tecnique called Scanning Probe Microscopy (SPM) which was originated from AFM invented by Binig and et al in 1982 [8].

Using cantilevers coated with magnetic materials such as permaloy or SmCo as force/force gradient sensing element, stray fields of samples can be detected and much information about magnetization of the sample can be obtained. But for an exact interpretation and good quantitative analysis, there are two fundamental problems hindering MFM

1. Lack of a priori information of magnetization of cantilever tips,
2. Coupling of magnetic force with other short and long range forces of a typical tip-sample interaction.

For the calibration of tips with magnetic coatings, generally two simplified models, i.e., single dipole moment and monopole moment approximations are used. But recently it has been shown that calibration of tips with these models depends on calibration samples because effective magnetic volume of interaction depends on characteristic decay length of the calibration samples [9, 10, 11]. As for the decoupling of magnetic forces from other forces of the tip-sample interaction, two-pass $Lift^{TM}$ mode MFM technique is generally used [12] and this technique may suffer from thermal drifts or topographical artifacts.

In this thesis we consider single domain particles attached to the cantilever tips as opposed to cantilevers fully coated with magnetic materials in order to circumvent the problem of dependance on characteristic decay length of calibration samples. For this purpose, a nickel thin film was built by evaporation on silicon wafer (also on S_3N_4) and then attached to the apex of a commercial cantilever tip by using standard Transmision Electron Microscopy (TEM) sample preparation techniques in a Focused Ion Beam (FIB) system. Also for the magnetic characterization of tips, magnetic field scans as in cantilever magnetometry [13, 14] were conducted and hysteresis curves obtained.

As for the decoupling of magnetic forces from other forces of tip-sample interaction such as *van der Waals* or repulsive atomic forces, we consider conventional AFM multifrequency imaging methodes in which the cantilever-tip ensemble is simultaneously excited by several driving forces[15]. We use first resonant flexural mode for topography signal acquisition, second resonant flexural mode for

measuring magnetic field interaction simultaneously. The sinusoidal voltage is applied to piezo bimorph to drive cantilever at the first resonant flexural mode and a magnetic field generated by a coil underneath the tip is used to exite second resonant flextural mode. Modulation of magnetic particle attached to tip as in fluxgate magnetometers [16, 17] can be used to decouple the interactions. Coherent rotation of magnetic moment is considered as basic switching mechanism [18].

1.2 Organization of the Thesis

The thesis is organized as follows: Chapter 2 gives an introduction to magnetism and hysterisis mechanism of the coherent rotation. In Chapter 3, a general theory of tip-sample interaction and Magnetic Force Microscopy (MFM) are given. Chapter 4 introduces the concept of mutifrequency imaging in Scaning Probe Microscopy. In Chapter 5, fluxgate principle and cantilever magnetomerty are considered. In Chapter 6, experimental results are given and comparisons to theoretical arguments are made. Finally, Chapter 7 concludes the thesis and gives future perspective on the subject.

Chapter 2

Introduction to Magnetism

The goal of this chapter to give the reader information about magnetism and relevant energy concepts. SI units are used throughout this thesis. Although it is well known that magnetism is inherently a quantum mechanical phenomena, discussion about energies given in classical way will be adequate for the scope of this thesis. Especially ferromagnetism will be dealt in some depth since most of magnetic phenemon such as hysteresis shows its richness and beauty in ferromagnetism. For more information about magnetism, reader is suggested to consult the following references [18, 19, 20].

2.1 Types of Magnetism

The best way to introduce different types of magnetism is to describe how materials respond to magnetic fields. All materials behave in a different way when exposed to an external magnetic field. In order to understand the mechanism of this difference, an atomic scale picture is more convenient. Magnetism at the atomic scale can arise from two different origins, i.e. the orbital motion of the electrons and the electron spin for incompletely filled orbitals. In an external magnetic field, a magnetic moment opposing the field is induced in a solid as a

result of *Lenz law* [21]. This diamagnetic effect is often superimposed by paramagnetism, which results from unfilled electron orbitals. In some materials there is a very strong interaction between atomic moments, and this coupling can result in different types of magnetism.

The magnetic behavior of materials can be classified into the following five major groups [22]:

1. Diamagnetism
2. Paramagnetism
3. Ferromagnetism
4. Antiferromagnetism
5. Ferrimagnetism

The induced magnetization $\vec{M}$ in materials, defined as the dipole moment per unit volume, is proportional to the external magnetic field $\vec{H}$ (isotropic and homogeneous) [21]:

$$\vec{M} = \chi \vec{H} \tag{2.1}$$

where χ is the magnetic susceptibility of the material. The relation between the magnetic inductance $\vec{B}$ and the magnetization $\vec{M}$ is then

$$\vec{B} = \mu_0 \left(\vec{H} + \vec{M}\right) = \mu_0 \left(\vec{H} + \chi \vec{H}\right) = \mu_0 \left(1 + \chi\right) \vec{H} = \mu_0 \mu_r \vec{H} \tag{2.2}$$

Here μ_0 is the vacuum permeability and $\mu_r = 1 + \chi$ the magnetic permeability, which is a material dependant parameter. Depending on the sign and magnitude of χ different types of magnetism are distinguished.

- Diamagnetism: Albeit it is usually very weak, diamagnetism is a fundamental property of all matter. It is due to the non-cooperative opposing behavior of orbiting electrons when exposed to an applied magnetic field. Diamagnetic substances are composed of atoms which have no net magnetic moments (i.e., all the orbital shells are filled leaving no unpaired electrons).

However, when exposed to a magnetic field, a negative magnetization is produced, so the susceptibility χ is negative.

- Paramagnetism: In this class of materials some of the atoms or ions in the material have a net magnetic moment due to unpaired electrons in partially filled orbitals. However, the individual magnetic moments do not interact magnetically, and the magnetization is zero when the field is removed. In the presence of a magnetic field, there is a partial alignment of the atomic magnetic moments in the direction of the field resulting in a net positive magnetization and positive susceptibility χ. In addition the efficiency of the field in aligning the moments is opposed by the randomizing effects of temperature. This results in a temperature dependent susceptibility known as the Curie Law.

- Ferromagnetism: Strong quantum mechanical coupling between atomic moments can result in different orderings. In ferromagnetic materials, aligned atomic moments give rise to a spontaneous magnetic moment called the *saturation magnetic moment* (M_s). The internal interaction tending to line up the magnetic moment is called the *exchange field* or *Weiss molecular field*. The exchange field is not a real magnetic field, i.e. corresponding to a current density, nevertheless one can deal with it as an equivalent magnetic field $\vec{H}_w = \lambda\vec{M}$. The value of this equivalent field can be as big as $\vec{B}_w \approx 10^3$ T which is much larger than external fields in normal conditions [18]. The alignment effect of the exchange field is reduced by thermal agitation. Above a certain temperature, the *Curie temperature* (T_C), the spontaneous magnetization vanishes and the spins are no longer ordered. Thus, the sample changes from ferromagnetic phase to paramagnetic phase at T_c . The temperature dependance of the susceptibility for ferromagnetic material follows *Curie-Weiss Law*:

$$\chi = \frac{C}{T - T_c}. \tag{2.3}$$

In ferromagnets, $\vec{M}$ is not proportional to $\vec{H}$, but depends in a complex way on the history of the magnetization. The relation between the magnetization along the direction of the external field $\vec{M}_H$ and $\vec{H}$ shows hysteresis as

can be seen in Fig. 2.1.

The various hysteresis parameters are not only intrinsic properties but also depend on grain size, domain state, stresses, and temperature. Explanation of hysteresis parameters is given below (Fig. 2.1).

Saturation Magnetization (Ms) Starting with the initial magnetization curve at an unmagnetized state, at a certain external field $\vec{H}$, the ferromagnet is saturated with the saturation magnetization Ms. Now all magnetic moments are aligned in the direction of the external magnetic field, so that the saturation magnetization is the largest magnetization, which can be achieved in the material.

Remnant Magnetization (Mr) After the external field is removed, a net magnetization will remain in the ferromagnet, called remanence, Mr.

Coercive Field (Hc) The negative external field at which the magnetization is reduced to zero is called coercive field $\vec{H}c$. Depending on the magnitude of $\vec{H}c$ hard and soft magnetic materials can be classified as $Hc \geq 100$ Oe $= 7958$ A/m, and $Hc \leq 5$ Oe $= 398$ A/m respectively [24].

- Antiferromagnetism: In an antiferromagnet spins are ordered as in ferromagnets but antiparallel with zero net magnetic moment. However, as in a ferromagnet, temperature plays a key role. The antiferromagnetic order is disappeared for temperatures above the *Neel temperature* (T_N).

- Ferrimagnetism: More complex forms of magnetic ordering (in some oxides such as NiO) called ferrimagnetism can occur as a result of the crystal structure. The magnetic structure is composed of two magneticaly ordered sublattices separated by the oxygen atoms. The exchange interactions are mediated by the oxygen anions. So these interactions are called indirect or superexchange interactions which result in an antiparallel alignment of spins between the sublattices. In ferrimagnets, the magnetic moments of the different sublattices are not equal and result in a net magnetic moment. Ferrimagnetism exhibits all the characteristics of ferromagnetism like

spontaneous magnetization, Curie temperature, hysteresis, and remanence. However ferro- and ferrimagnets have very different magnetic ordering.

2.2 Magnetic Energy Contributions

Two basic mechanisms are responsible for the behavior of magnetic materials, exchange and anisotropy [18]. Exchange mechanism results from the combination of the electrostatic interaction between electron orbitals and the Pauli exclusion principle. It results in spin-spin interactions that is favorable for long-range spin ordering over macroscopic distances. Anisotropy is mainly related to interactions of electron orbitals with the potential of the hosting lattice. Lattice symmetry reflected in the symmetry of the potential results in spin orientation along certain symmetry axes of the hosting lattice so that it is energetically favored.

2.2.1 Exchange Energy

For the explanation of ferromagnetism phenomenological molecular field approach is proposed. In fact for the microscopic interpretation of the molecular field, one needs quantum mechanical results in terms of the so-called *exchange interaction*. According to this theory two electrons that carry parallel spins (which corresponds to a symmetric spin wave function) cannot stay close to each other because of the property of antisymmetric two-electron wave function in real space. The fact that they never come close reduces the average energy of electrostatic interaction which favors the parallel spin configuration. In terms of *Heisenberg Hamiltonian* exchange energy density e_{Ex} can be written as

$$e_{Ex} = -2J \sum_{ij} \vec{S}_i \vec{S}_j \tag{2.4}$$

where J is called exchange constant. The exchange coupling is a short range interaction so only spins close to each other are effected. For $J > 0$ a parallel arrangement is energetically favored as seen in ferromagnetism, but it is an antiparallel configuration for $J < 0$.

2.2.2 Magnetocrystalline Anisotropy

As seen from Eq. 2.4 exchange interactions are isotropic in space which means the exchange energy of a given system is the same for any orientation of the magnetization vector whose strength remains the same. In reality this rotational symetry is always broken by anisotropy effects which make particular spatial directions energetically favored. For a certain volume V with uniform magnetization $\vec{M}$ dependence of magnetic anisotropy enegy can be written in terms of $\vec{m} = \vec{M}/\left|\vec{M}\right|$. $\vec{m}$ can be described by its Cartesian components m_x, m_y, m_z (same as direction cosines) or spherical cordinates θ,ϕ (Fig. 2.2).

$$\begin{aligned} m_x &= \sin(\theta)\cos(\phi) \\ m_y &= \sin(\theta)\sin(\phi) \\ m_z &= \cos(\theta). \end{aligned} \tag{2.5}$$

Magnetic anisotropy energy density $e_{AN}(\vec{m})$, can be graphically represented as a surface in space. The distance between the point of the surface and origin along the direction $\vec{m}$ is just $e_{AN}(\vec{m})$. In this representation isotropic exchange energy gives rise to a sphere (Fig. 2.3).

Since absolute value of the magnetic anisotropy energy density plays no role $e_{AN}(\vec{m})$ can be defined as a constant independent of $\vec{m}$. The presence of depressions in the energy surface immediately show the space directions that are energetically favored. These directions called easy magnetization axes represent the directions along which the magnetization is naturally oriented to minimize the system magnetic energy (Fig. 2.3).

The equilibrium points of $\vec{m}$ directions satisfying the equilibrium condition

$$\frac{\partial e_{AN}(\vec{m})}{\partial \vec{m}} = 0 \tag{2.6}$$

under the constraint $|\vec{m}| = 1$ can be local minima, saddle points, or local maxima of the energy surface. A local minimum corresponds to an magnetic easy axis. On the other hand the terms medium-hard axis and hard axis are sometimes used to refer to a saddle point or to a local maximum, respectively. There are

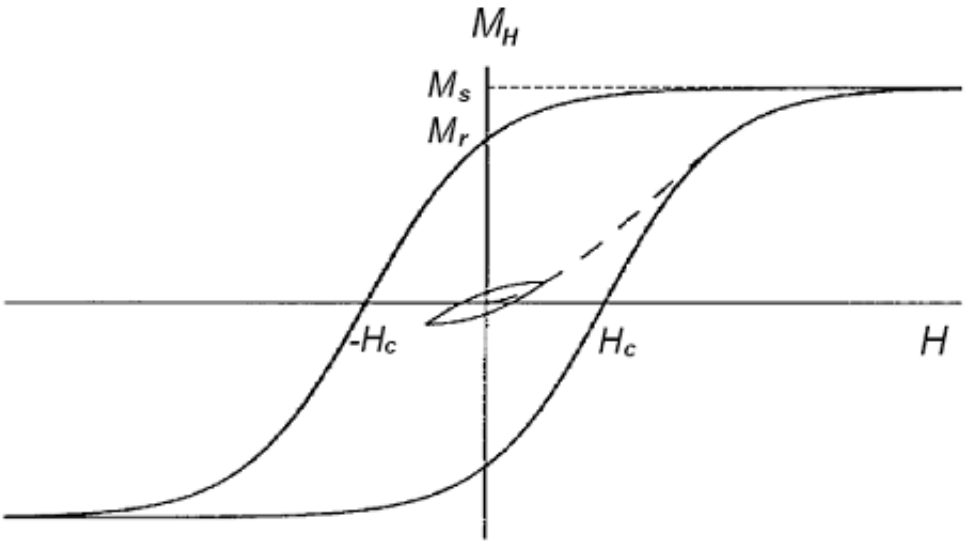

Figure 2.1: Hysteresis curve for ferromagnetic materials, showing magnetization $\vec{M}$ in the direction of the external field as a function of $\vec{H}$ [23].

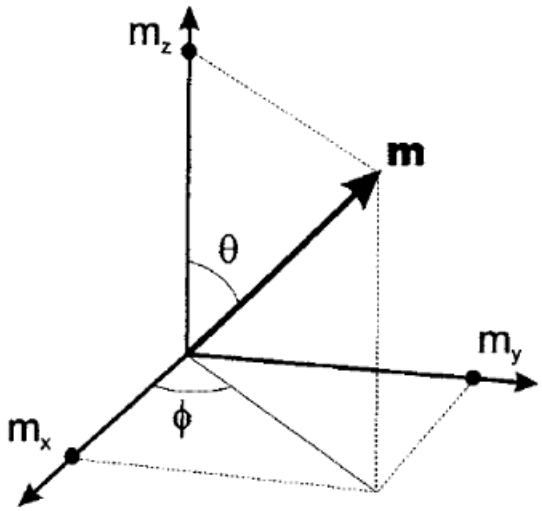

Figure 2.2: Magnetization unit vector $\vec{m}$, with definition of direction cosines and spherical angle coordinates.

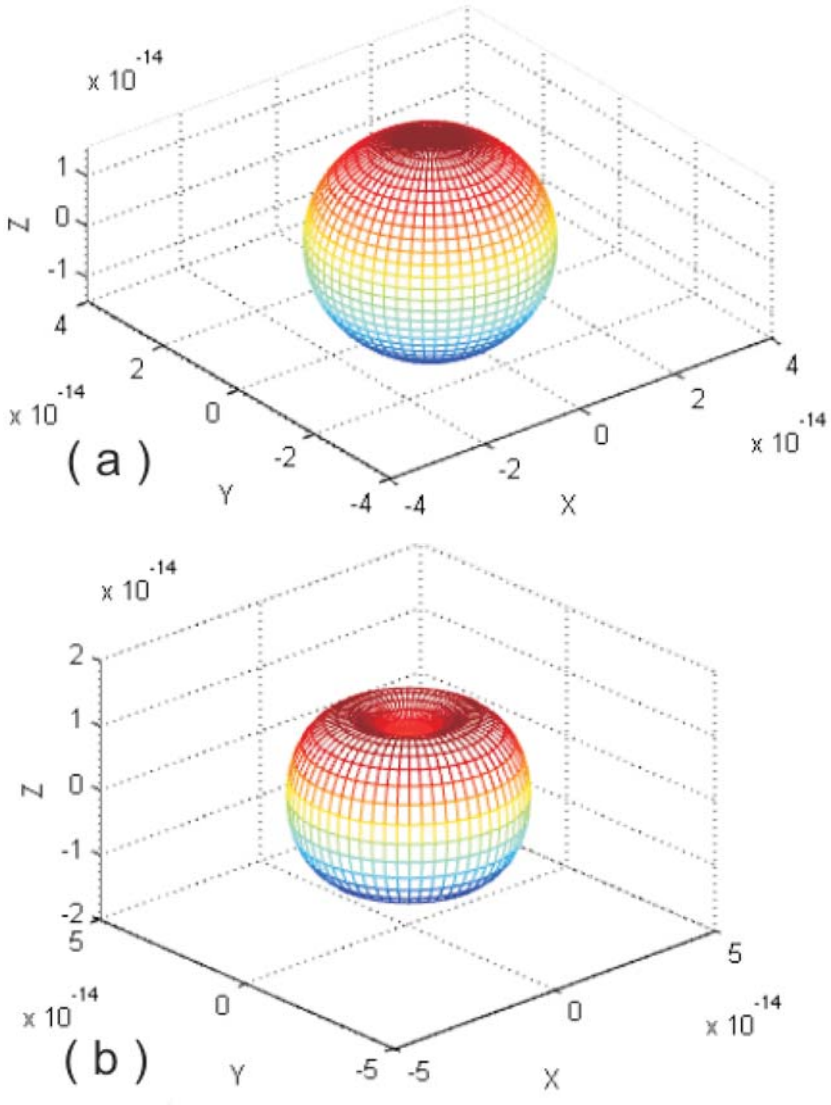

Figure 2.3: (a) The surface of exchange energy density e_{EX}, and (b) broken spherical symmetry with formation of easy magnetization axis ($\vec{z}$ axis).

generally two basic symetry breaking magnetic anisotropy, i.e. *uniaxial* and *cubic* anisotropy.

2.2.2.1 Uniaxial Anisotropy

There is one special direction in space in uniaxial anisotropy and $\vec{z}$ axis can be selected as this direction. The anisotropy energy is invariant with respect to rotations around this anisotropy axis, and depends only on the relative orientation of $\vec{m}$ with respect to the axis (cobalt is an example having uniaxial anisotropy). To satisfy symetry considerations, the anisotropy energy is defined with an even function of the magnetization component along $\vec{z}$ as $m_z = \cos\theta$. Generally $m_x^2 + m_y^2 = 1 - m_z^2 = 1 - \cos\theta^2 = \sin\theta^2$ is used instead of $\cos^2\theta$ as the expansion variable. Thus the energy density $e_{AN}(\vec{m})$ will have the general expansion

$$e_{AN}(\theta) = K_0 + K_1 \sin^2\theta + K_2 sin^4\theta + K_3 sin^6\theta + \cdots \tag{2.7}$$

where the anisotropy constants K_1, K_2, K_3 have the dimensions of energy per unit volume ($\mathrm{J/m^3}$). When $K_1 > 0$, there are two energy minima at $\theta = 0$ and $\theta = \pi$ corresponding to the magnetization along the anisotropy axis with no preferential orientation. The anisotropy axis is an energetically favourable axis for $\vec{m}$ (Fig. 2.4). This type of anisotropy is known as *easy-axis anisotropy*. Conversely, when $K_1 < 0$, the energy is at a minimum for $\theta = \pi/2$ which corresponds to $\vec{m}$ perpendicular to the axis pointing anywhere in the x-y plane which is described by the term easy-plane anisotropy (Fig. 2.5).

For the case where $K_1 > 0$ and $\vec{m}$ lies along the easy axis, the anisotropy energy density of small deviations of the magnetization vector from the equilibrium position can be approximated to second order in θ as

$$\begin{aligned} e_{AN}(\theta) \approx K_1\theta^2 &\approx K_1 2(1 - \cos\theta) \\ &= 2K_1 - \mu_0 M_s \frac{2K_1}{\mu_0 M_s}\cos\theta = 2K_1 - \mu_0 M_s \cdot H_{AN}. \end{aligned} \tag{2.8}$$

The angular dependence of the energy is the same as if there was a field of strength

$$H_{AN} = \frac{2K_1}{\mu_0 M_s} \tag{2.9}$$

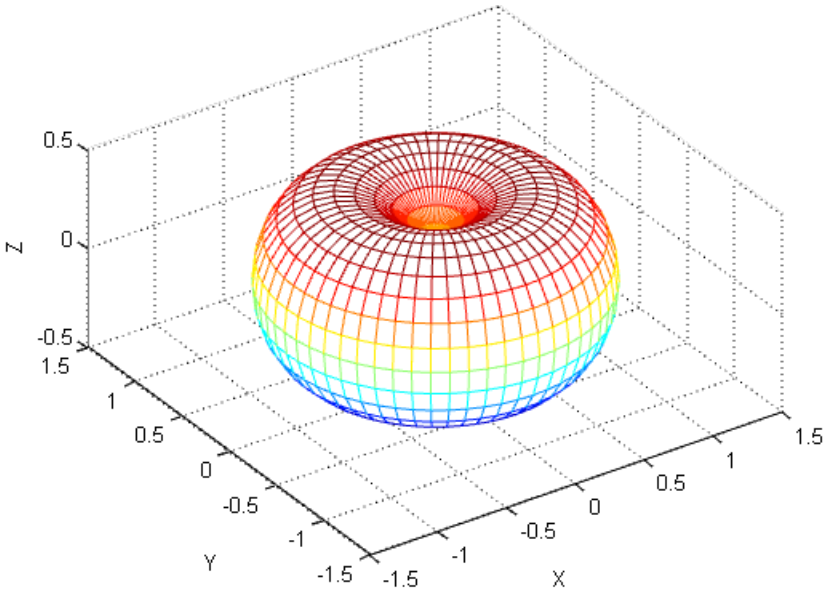

Figure 2.4: Uniaxial anisotropy with $K_1 > 0$. Energy surface associated with Eq. 2.7, when $K_0 = 0.1$, $K_1 = 1$, $K_2 = K_3 = 0$. The $\vec{z}$ axis is an easy magnetization axis.

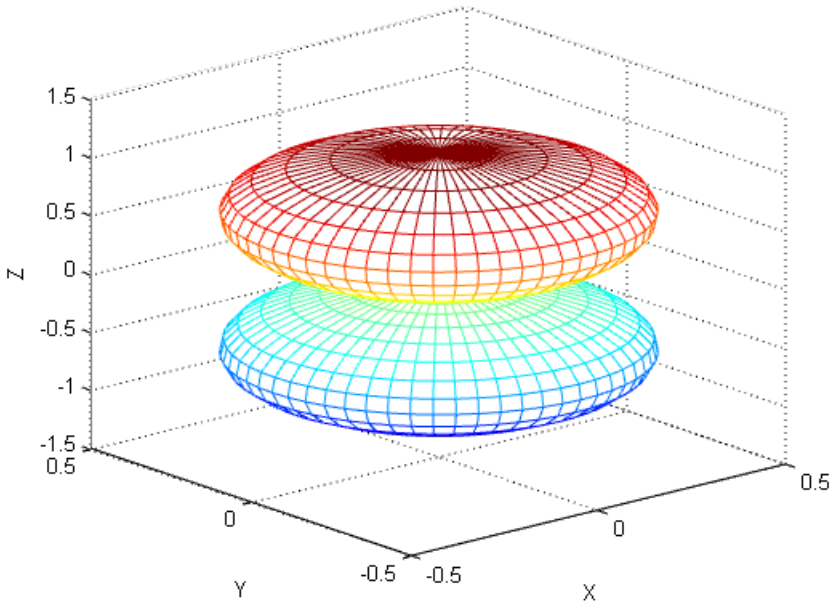

Figure 2.5: Uniaxial anisotropy with $K_1 < 0$. Energy surface associated with Eq. 2.7, when $K_0 = 1.1, K_1 = -1, K_2 = K_3 = 0$. The x-y plane is an easy magnetization plane.

acting along the easy axis. The *anisotropy field* H_{AN} gives a measure of the strength of the anisotropy effect.

2.2.2.2 Cubic Anisotropy

This anisotropy typically originates from spin-lattice coupling in cubic crystals such as nickel and iron. This anisotropy implies the existence of three special directions (4 for Ni), which can be taken as the x-y-z axes. The lowest order combinations of $\vec{m}$ components constrained with the required symmetry are the fourth-order combination $m_x^2 m_y^2 + m_y^2 m_z^2 + m_z^2 m_x^2$ and the sixth-order one, i.e. $m_x^2 m_y^2 m_z^2$. The combination $m_x^4 + m_y^4 + m_z^4$ is dependent on the previous ones as

$$m_x^4 + m_y^4 + m_z^4 + 2(m_x^2 m_y^2 + m_y^2 m_z^2 + m_z^2 m_x^2) = m_x^2 + m_y^2 + m_z^2 = 1, \qquad (2.10)$$

so it is not used. The expression of the anisotropy energy takes the form

$$e_{AN} = K_0 + K_1(m_x^2 m_y^2 + m_y^2 m_z^2 + m_z^2 m_x^2) + K_2(m_x^2 m_y^2 m_z^2) + \cdots. \qquad (2.11)$$

The equivalent expression in terms of spherical coordinates is

$$\begin{aligned} e_{AN} = K_0 &+ K_1 \left(\frac{\sin^2\theta \sin^2 2\phi}{4} + \cos^2\theta \right) \sin^2\theta \\ &+ K_2 \left(\frac{\sin^2 2\phi}{16} \right) \sin^2\theta + \cdots. \end{aligned} \qquad (2.12)$$

When only the fourth-order term is important (i.e. $K_2 = 0$), the behavior of $e_{AN}(\vec{m})$ is shown in Fig. 2.6 ($K1 > 0$) and Fig. 2.7 ($K1 < 0$). When $K_1 > 0$, there are six equivalent energy minima when the magnetization points along the x, y, or z axes, in the positive or negative direction which identify easy magnetization axes. The easy axes are $< 100 >$ axes. $< 110 >$ directions are saddle points of the energy surface (medium-hard axes), whereas the $< 111 >$ directions are local maxima (hard axes) as can seen in Fig. 2.6.

When $K_1 < 0$ (Fig. 2.7) there are now eight equivalent energy minima when the magnetization points along the $< 111 >$ directions. The $< 110 >$ directions are medium-hard axes, the $< 100 >$ directions are hard axes.

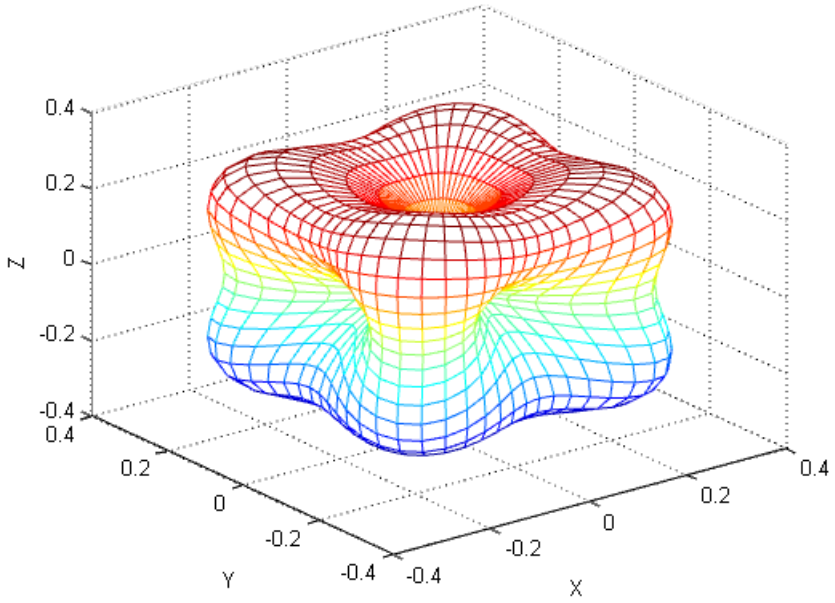

Figure 2.6: Cubic anisotropy with $K_1 > 0$. Energy surface associated with Eq. 2.11, when $K_0 = 0.1, K_1 = 1, K_2 = 0$.

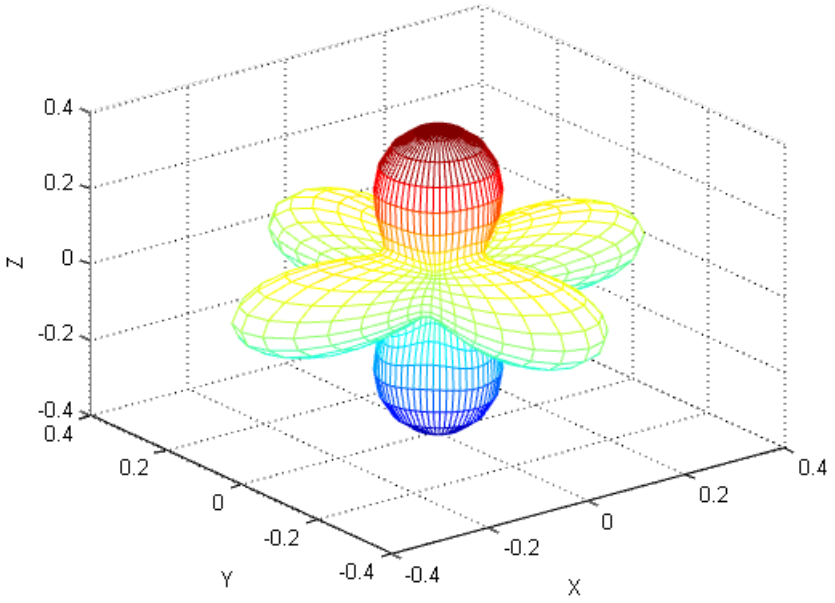

Figure 2.7: Cubic anisotropy with $K_1 < 0$. Energy surface associated with Eq. 2.11, when $K_0 = 0.4, K_1 = -1, K_2 = 0$.

2.2.3 Magnetostatics

When spatial distribution of magnetization $\mathbf{M}(\vec{\mathbf{r}})$ of materials is known in advance, solution of magnetostatic equations can be represented equivalently as [18]:

$$\mathbf{A_M}(\vec{\mathbf{r}}) = \frac{\mu_0}{4\pi}\int_V \frac{\nabla \times \mathbf{M}(\vec{\mathbf{r}}')}{|\vec{r}-\vec{r}'|}d^3r' - \frac{\mu_0}{4\pi}\oint_S \frac{\mathbf{n}\times\mathbf{M}(\vec{\mathbf{r}}')}{|\vec{r}-\vec{r}'|}da' \tag{2.13}$$

$$\mathbf{\Phi_M}(\vec{\mathbf{r}}) = -\frac{\mu_0}{4\pi}\int_V \frac{\nabla \cdot \mathbf{M}(\vec{\mathbf{r}}')}{|\vec{r}-\vec{r}'|}d^3r' + \frac{\mu_0}{4\pi}\oint_S \frac{\mathbf{n}\cdot\mathbf{M}(\vec{\mathbf{r}}')}{|\vec{r}-\vec{r}'|}da' \tag{2.14}$$

These fields are the consequence of the existence of a certain magnetization $\mathbf{M}(\vec{\mathbf{r}})$ in the system, so the subscript in $\mathbf{A_M}(\vec{\mathbf{r}})$ and $\mathbf{\Phi_M}(\vec{\mathbf{r}})$ is used. In both equations, the first integral is a volume integral over the body volume V, and the second is a surface integral over the boundary surface S. $\vec{\mathbf{n}}$ is the unit vector normal to the surface element da' pointing out of the body. The quantities

$$\begin{aligned}\vec{k}_M &= -\vec{n}\times\vec{\mathbf{M}}\\ \sigma_M &= \vec{n}\cdot\vec{\mathbf{M}}\end{aligned} \tag{2.15}$$

describe effect of singularities at the body surface. They play the same role of surface magnetization current $\vec{k}_M$ and of surface magnetic charge density σ_M (see Fig. 2.8).

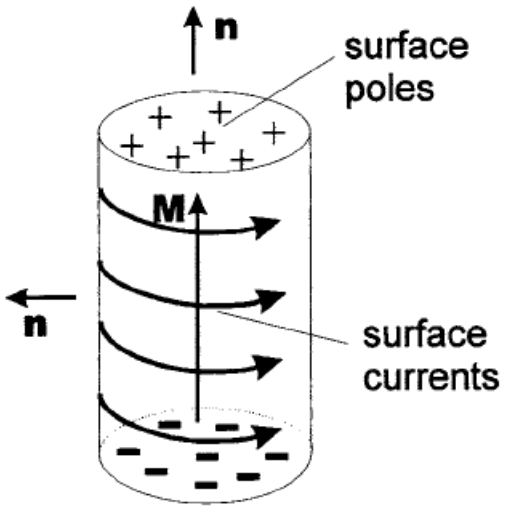

Figure 2.8: Uniformly magnetized cylinder with representation of surface poles and surface currents (Eq. 2.15) [18].

Among the situations where the magnetic state of the system is known in advance, the simplest situation is the one where the magnetization is uniform everywhere inside the body, so that it can be described by a single vector $\vec{M}$. Since $\nabla \cdot \vec{\mathbf{M}} = 0$ everywhere inside the body, only the surface integral of Eq. 2.14 contributes to the scalar potential:

$$\mathbf{\Phi}(\vec{\mathbf{r}})_{\mathbf{M}} = \frac{1}{4\pi}\vec{\mathbf{M}} \cdot \oint_S \frac{\vec{\mathbf{n}}}{|\vec{r} - \vec{r'}|} da'. \tag{2.16}$$

Equation 2.16 shows that, apart from the overall proportionality on $\vec{\mathbf{M}}$, the scalar potential is determined uniquely by the geometrical shape of the body. In the case of uniform $\vec{\mathbf{M}}$ the field $\vec{\mathbf{H}}_{\mathbf{M}} = -\nabla \cdot \Phi$ is itself uniform everywhere inside the body if the body is of ellipsoidal shape. If $\vec{\mathbf{M}}$ lies along one of the principal axes of the ellipsoid, then the field $\vec{\mathbf{H}}$ is antiparallel to it, and has an intensity proportional to $\vec{\mathbf{M}}$ (see Fig. 2.9).

$$\vec{\mathbf{H}}_{\mathbf{M}} = -N\vec{\mathbf{M}} \tag{2.17}$$

Under these circumstances, the magnetic field $\vec{\mathbf{H}}_{\mathbf{M}}$ inside the body is usually termed the demagnetizing field, as the name implies it opposes the magnetization, and the coefficient N is called the *demagnetizing factor*. The value of N depends on which ellipsoid axis $\vec{\mathbf{M}}$ lies along. In general case there are three demagnetizing factors, N_a, N_b, N_c, associated with each of the three ellipsoid principal axes, a, b, c. These demagnetizing factors obey the general constraint

$$N_a + N_b + N_c = 1. \tag{2.18}$$

The magnetostatic energy of a magnetized body is

$$U_{MS} = -\frac{\mu_0}{2}\int_V \mathbf{H}_M \cdot \mathbf{M} d^3r \tag{2.19}$$

In the case of an ellipsoidal body uniformly magnetized along an arbitrary magnetization orientation, Eq. 2.19 can be written in terms of *demagnetizing constants* as

$$\begin{aligned} e_{MS} = U_{MS}/V &= \frac{1}{2}\mu_0(N_a M_x^2 + N_b M_y^2 + N_c M_z^2) \\ &= \frac{1}{2}\mu_0 M_s^2(N_a m_x^2 + N_b m_y^2 + N_c m_z^2) \end{aligned} \tag{2.20}$$

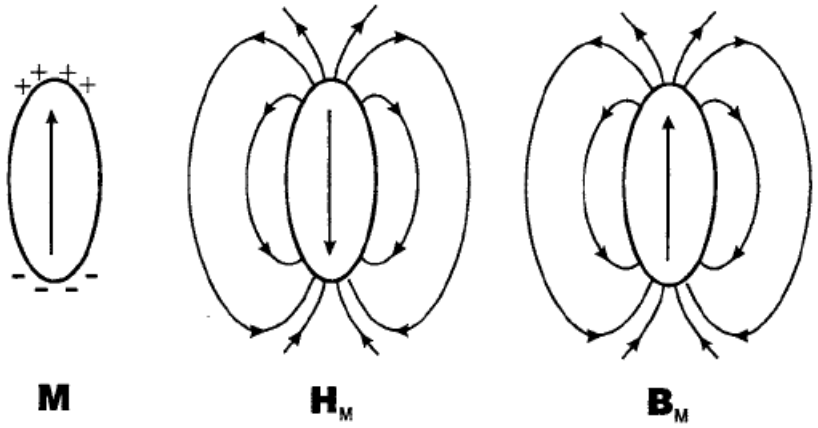

Figure 2.9: Magnetization, magnetostatic field, and induction for uniformly magnetized ellipsoid [18].

where N_a, N_b, and N_c are the demagnetizing factors related to the three principal axes. The origin of shape anisotropy is this magnetostatic energy. It can be as important as magnetocrystalline anisotropy for the magnetization process under some circumstances. In the case of a spheroid, where two principal axes are equal, the body has rotational symmetry around the third, so Equation 2.20 becomes

$$\begin{aligned} e_{MS} &= \frac{1}{2}\mu_0 M_s^2 \left(N_\perp(m_x^2 + m_y^2) + N_\parallel m_z^2\right) = \frac{1}{2}\mu_0 M_s^2 \left(N_\perp sin^2\theta + N_\parallel cos^2\theta\right) \\ &= \frac{1}{2}\mu_0 M_s^2 N_\parallel + \frac{1}{2}\mu_0 M_s^2 (N_\perp - N_\parallel) sin^2\theta \end{aligned} \tag{2.21}$$

Equation 2.21 has the same symmetry characteristic of uniaxial anisotropy. The term shape anisotropy is used because originates from the geometrical shape of the body.

2.2.4 Magnetoelastic Energy

In addition to magnetocrystalline anisotropy there is also another effect related to spin-orbit coupling called magnetostriction. It arises from the strain dependence of the anisotropy constants. A previously demagnetized crystal can experience a strain upon magnetization therefore change its dimension. For example in Ni $\lambda_{100} = -46 \cdot 10^{-6}$ and $\lambda_{111} = -25 \cdot 10^{-6}$ which means magnetization of nickel contracts the crystal in the magnetization direction. The contraction is bigger in

the $< 100 >$ direction. The inverse affect, the change of magnetization with stress also occurs. A uniaxial stress can produce a unique easy axis of magnetization if it is strong enough to overcome all other anisotropies.

The magnitude of the stress anisotropy is described by two or more empirical constants called the magnetostriction constants (λ_{111} and λ_{100}) and the level of stress. The magnetoelastic anisotropy energy density [18] can be written as

$$e_{ME} = \frac{3}{2}\lambda\sigma \sin^2\theta \tag{2.22}$$

where θ is the angle between the magnetization and the stress σ direction, and λ is the appropriate magnetostriction constant. The stress creates an uniaxial anisotropy along the direction of stress applied. The associated anisotropy constant is

$$K_{ME} = \frac{3}{2}\lambda\sigma. \tag{2.23}$$

Respectively depending on whether $\lambda\sigma > 0$ *or* $\lambda\sigma < 0$.

For cubic materials [25], magnetoelastic anisotropy energy density e_{ME} is given by another expression

$$e_{ME} = B_1(m_x^2\epsilon_{xx} + m_y^2\epsilon_{yy} + m_z^2\epsilon_{zz}) + B_2(m_x m_y\epsilon_{xy} + m_y m_z\epsilon_{yz} + m_z m_x\epsilon_{zx}) \tag{2.24}$$

where m_i are components of the magnetization $\vec{\mathbf{M}}$, ϵ_{ij} is the strain tensor and B_i are the magnetoelastic coeffcients. The latter expresses the coupling between the strain tensor and the direction of the magnetization.

2.2.5 Zeeman Energy

The Zeeman energy is the potential energy of a magnetic moment in a field, or the potential energy per unit volume for a large number of moments [25] :

$$e_Z = -\mu_0\vec{M}\cdot\vec{H} = -\mu_0 MH\cos\theta \tag{2.25}$$

where θ is the angle between the magnetization and the applied magnetic field. Orientation of magnetic moment in the direction of applied field results in lowest energy configuration (see Fig. 2.10).

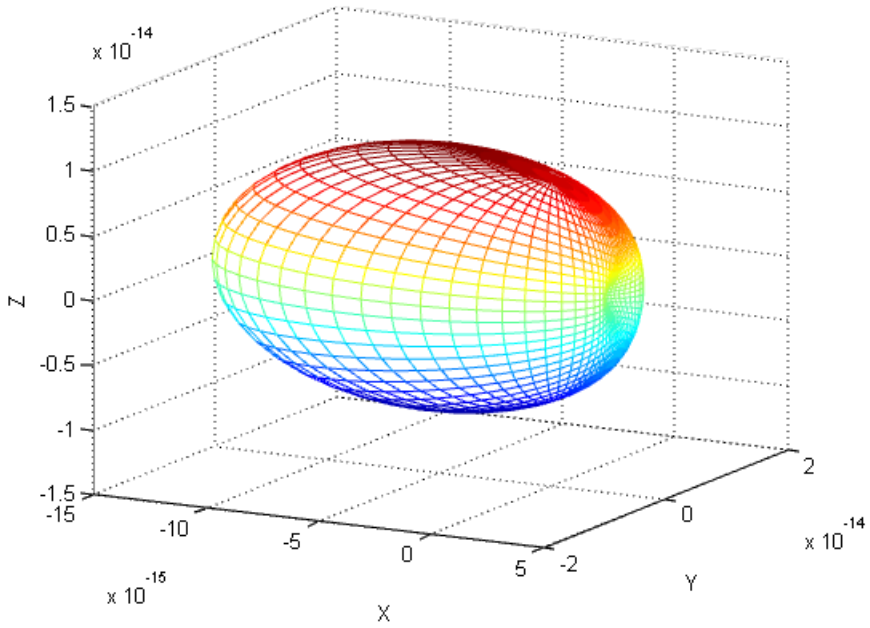

Figure 2.10: The lowest energy orientation in the direction of applied field $\vec{B} = b\vec{x}$ is shown as a depression on the energy surface.

2.3 Coherent Rotation

According to theory of coherent rotation[1] a single magnetization $\vec{m} = \vec{M}/|M|$ vector is sufficient to describe the state of a whole system [18]. When the magnetization rotates under the action of the external field, the change is spatially uniform. The most natural example is that of a magnetic particle small enough to be a single domain. The particle may exhibit magnetocrystalline anisotropy and shape anisotropy. We consider the particular case of a elipsoidal particle made up of a material with uniaxial magnetocrystalline anisotropy, and the crystal anisotropy axis coincides with the symmetry axis of the elipsoid. According to Eq. 2.7 and Eq. 2.21 the magnetocrystalline and shape anisotropy energies have the same dependence on $\vec{M}$ orientation and can be summed up to give a total anisotropy energy density of the form

$$e_{AN}(\vec{m}) = K_{eff} \sin^2 \phi \tag{2.26}$$

[1]Stoner-Wohlfarth Model

where ϕ is the angle between $\vec{m}$ and the anisotropy axis, and the effective anisotropy constant K_{eff} is equal to

$$K_{eff} = K_1 + K_{MS} = K_1 + \frac{\mu_0 M_s^2}{2}(N_\perp - N_\parallel). \tag{2.27}$$

K_1 is the uniaxial magneto-crystalline anisotropy constant, and K_{MS} is the shape anisotropy constant. if it is assumed that $K_{eff} > 0$, then the anisotropy axis is the easy direction of magnetization. Under zero field conditions, $\vec{m}$ is aligned to the easy axis. In an applied external field $\vec{H}$, $\vec{M}$ rotates magnetization away from the easy axis by an angle depending on the relative strength of anisotropy and field. Because of symmetry arguments $\vec{m}$ will lie in the plane containing the anisotropy axis and the external field. For the description of two-dimensional problem in this plane we call ϕ and θ the angles made by $\vec{m}$ and $\vec{H}$ with the easy axis (see Fig. 2.11). The magnetic energy of the particle is then sum of magnetic anisotropy energy (Eq: 2.7) and Zeeman energy (Eq. 2.25)

$$e(\theta, \vec{H}) = VK_{eff}\sin^2\phi - \mu_0 M_s V H cos(\theta - \phi), \tag{2.28}$$

where V is the particle volume. The system is described by three parameters,

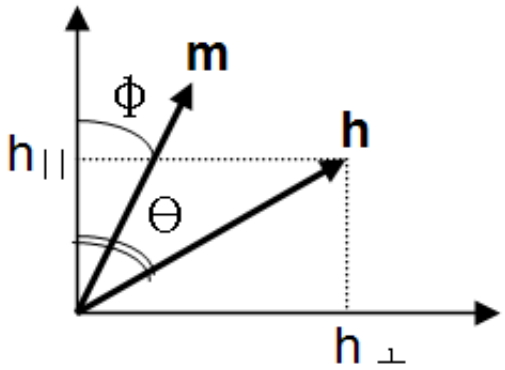

Figure 2.11: Relations between uniaxial anisotropy axis, magnetization unit vector, $\vec{M}$ and external field, $\vec{H}$.

i.e. the angles ϕ, θ , and H. Eq. 2.28 can be written in dimensionless form, by introducing

$$\bar{e}(\phi, \vec{h}) = \frac{e(\phi, \vec{H})}{2K_{eff}V} \qquad and \qquad h = \frac{\mu_0 M_S}{2K_{eff}}H = \frac{H}{H_{AN}} \tag{2.29}$$

where H_{AN} is the anisotropy field (see Eq. 2.9). We obtain

$$\bar{e}(\phi, \vec{h}) = \frac{1}{2} sin^2\phi - hcos(\theta - \phi). \tag{2.30}$$

Instead of $(\phi, \vec{h})$ it will be more convenient to use the field components perpendicular and parallel to the easy axis defined as

$$\begin{aligned} h_\perp &= hsin\theta \\ h_\parallel &= hcos\theta. \end{aligned} \tag{2.31}$$

In terms of these variables, Eq. 2.30 becomes

$$\bar{e}(\phi, \vec{h}) = \frac{1}{2} sin^2\phi - h_\perp \sin\phi - h_\parallel \cos\phi. \tag{2.32}$$

For $\theta = 0$ energy surface $\bar{e}(\phi, h)$ is shown in Fig. 2.12.

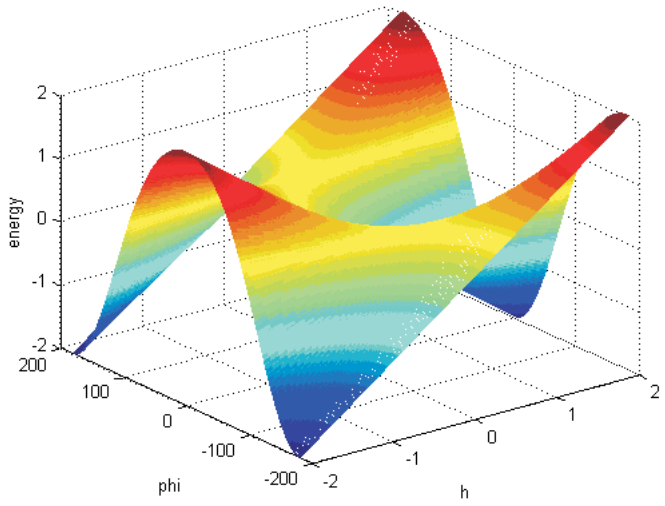

Figure 2.12: Energy surface showing minimum, maximum and saddle point (calculated with Eq: 2.30, $\theta = 0$).

Under zero field, there exist two energy minima, corresponding to $\vec{m}$ pointing up or down along the easy axis. For small fields around zero, one stable and one metastable states are available to the system. Conversely, when $\vec{h}$ is very large, there is one stable state available, in which $\vec{m}$ is closely aligned to the field. Therefore, there must exist two different regions, two-energy minima low-field region

and one-energy-minimum outer region. The boundary curve represents the bifurcation set for magnetization problem where discontinuous changes (*Barkhausen jumps*) in the state of the system may take place [18]. By calculating $\partial\bar{e}(\phi,\vec{h})/\partial\phi$ from Eq. 2.32 and by imposing the condition $\partial\bar{e}(\phi,\vec{h})/\partial\phi = 0$ one obtains the equation

$$\frac{h_\perp}{sin\phi} - \frac{h_\parallel}{cos\phi} = 1 \tag{2.33}$$

By calculating $\partial^2\bar{e}(\phi,\vec{h})/\partial^2\phi$ and using the stability criteria $\partial^2\bar{e}(\phi,\vec{h})/\partial^2\phi = 0$ in addition to Eq. 2.33, one further obtains

$$\frac{h_\perp}{sin^3\phi} + \frac{h_\parallel}{cos^3\phi} = 0. \tag{2.34}$$

Eliminating in turn $h_\perp$ and $h_\parallel$, from Eq. 2.33 and Eq. 2.34, the following parametric representation of the boundary curve is obtained:

$$\begin{aligned} h_\perp &= sin^3\phi \\ h_\parallel &= -cos^3\phi, \end{aligned} \tag{2.35}$$

where ϕ represents the orientation of $\vec{M}$ in the state of instability at the point considered. This curve is the *astroid* shown in Fig. 2.13. Various energy profiles also can be seen on the h space, ($\tilde{h} = h_\perp$,$h_\parallel$).

Each equilibrium state obeys Eq. 2.33. By writing Eq. 2.33 as in the form

$$h_\perp = h_\parallel \tan\phi + \sin\phi \tag{2.36}$$

the following conclusion can be arrived: The set of all points of the $\tilde{h}$ plane where $\bar{e}(\phi,\vec{h})$ has a minimum or maximum in correspondence of a given orientation ϕ_0, $\vec{m}$ is represented by the straight line tangent to the astroid at the point of coordinates calculated by Eq. 2.35. And considering second-order derivative $\partial^2\bar{e}(\phi,\vec{h})/\partial^2\phi$ stable orientations can be found.

In the magnetization process under alternating (AC) field, the field point moves back and forth in $\tilde{h}$ space along a fixed straight line. The $\vec{m}$ orientation at each point is obtained by the tangent construction discussed. If the field oscillation were all contained inside the astroid $h < 1$, the magnetization would reversibly oscillate around the orientation initially occupied on past history. If

field amplitude is large enough to cross the astroid boundary, then the state occupied by the system loses stability when the field representative point exits the astroid. At that moment a *Barkhausen jump* takes place and some energy is dissipated. For various θ orientations of magnetic field $\vec{h}$, hysterisis curves can be obtained as in Fig. 2.14.

2.4 Domain Walls

In real materials at temperatures below the Curie temperature, an external field is needed to drive the sample to saturation, due to the presence of domains. Although the electronic magnetic moments are aligned on atomic scale different regions of magnetization direction can coexist. These are called domains and the magnetization is saturated in each domain. If the area covered by both domains is equal, the overall magnetization is zero (Fig. 2.15). The anisotropy energy defines the direction of magnetization inside the domains, which will be parallel to the easy axes. On the other hand the exchange energy, it causes neighboring spins to be parallel to each other. Regarding these two energy contributions a one-domain configuration with the magnetization pointing in the direction of the easy axis seems energetically favored (see Fig. 2.15). However, when the demagnetization energy is taken into account, it can be seen that it counteracts a large stray field resulting from the domain configuration of the ferromagnetic particle.

Various types of domain wall structure exist (see Fig. 2.16). Domain structures always arise from the possibility of lowering total energy of the system, by going from a saturated domain configuration with high magnetic energy to a domain configuration with a lower energy.

2.5 Properties of Nickel

Nickel is hard grey-silver metal. It is a transition metal. Like cobalt and iron it belongs to period IV and is ferromagnetic. The main nickel parameters are given

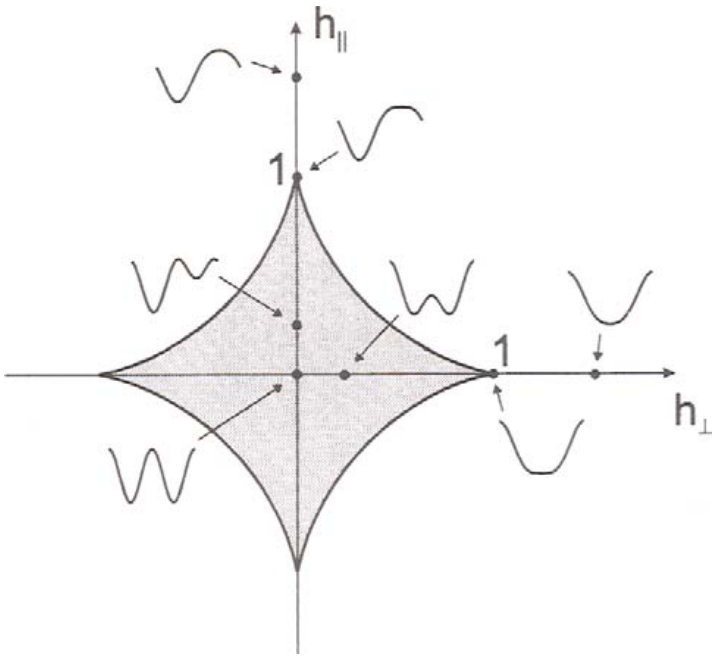

Figure 2.13: Control plane of coordinates $h_{\|}$ and $h_{\perp}$. The border of shaded region is the astroid curve defined by Eq. 2.35. Examples of the dependence of the system energy $\bar{e}(\phi, \vec{h})$ (Eq. 2.32) on ϕ at different points in control space $\tilde{h}$ are shown [18].

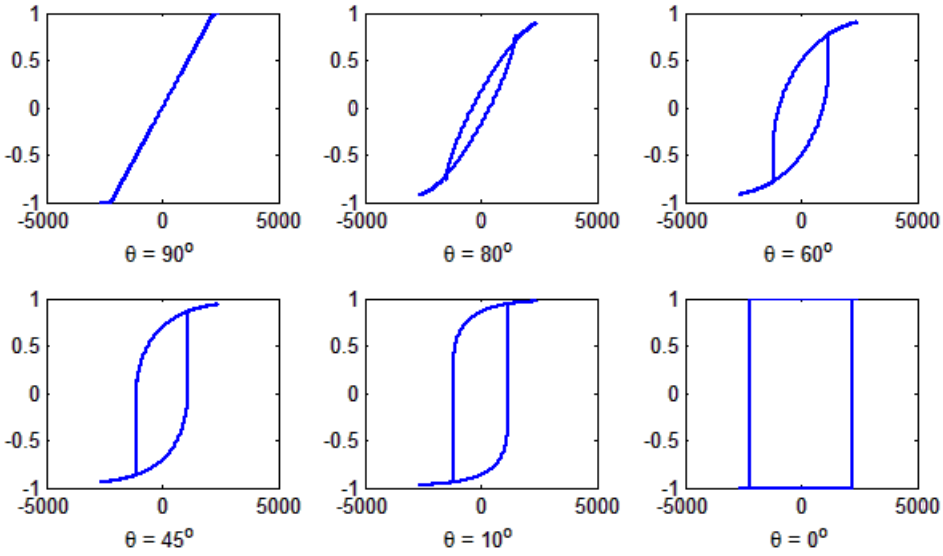

Figure 2.14: Hysteresis curves of a single domain particle having uniaxial unisotropy are shown for different values of θ, angle between $\vec{m}$ and $\vec{B}$ (Gauss).

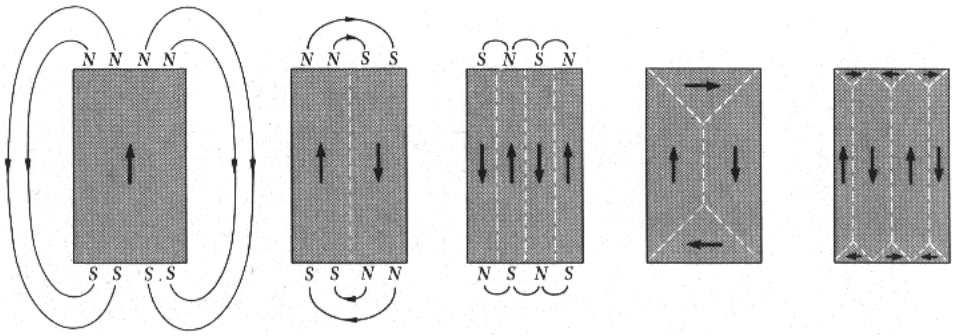

Figure 2.15: Domain patterns in small ferromagnetic particles. From left to right, the demagnetization energy is reduced by the formation of domains especially by closure domains [25].

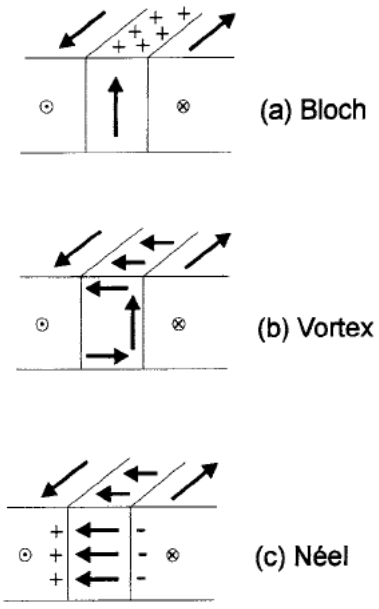

Figure 2.16: Various types of domain walls can be realised [18].

in the Tab. 2.2. A schematic of the cubic lattice is shown in Fig. 2.17.a. Note that [111] is the easy magnetization direction (Cubic anisotropy) [25]. Magnetization in other directions can also be seen in Fig. 2.17.b.

The nickel magnetocrystalline anisotropy has a temperature dependant character [26]. The strong temperature dependance of the three anisotropy factors K_1, K_2 and K_3 can be seen in Fig. 2.18. It also can be seen that K_2 and K_3 are large enough to have considerable effect. They also can change sign.

We choose nickel as a magnetic fluxgate element because of its intrinsic magnetic properties such as the small saturation magnetization (resulting in a relatively small magnetostatic energy density) and the rather small magnetocrystalline anisotropies at room temperature.

Relative importance of the energies for Ni is given in Tab. 2.1. A strain of only 0.1% in nickel gives rise to a magnetoelastic anisotropy comparable to K_1. To have a magnetoelastic anisotropy comparable to the magnetostatic anisotropy strains of 2.4% are needed in Ni films.

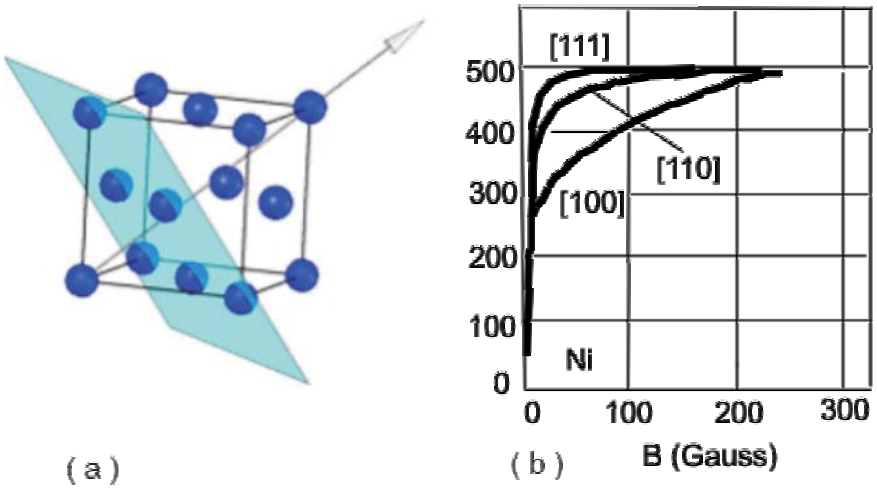

Figure 2.17: (a) Schemetic of a fcc cubic lattice of nickel. The arrow represents magnetic easy axis ⟨111⟩ direction of nickel [25]. (b) Magnetization curves for single crystal of nickel [19].

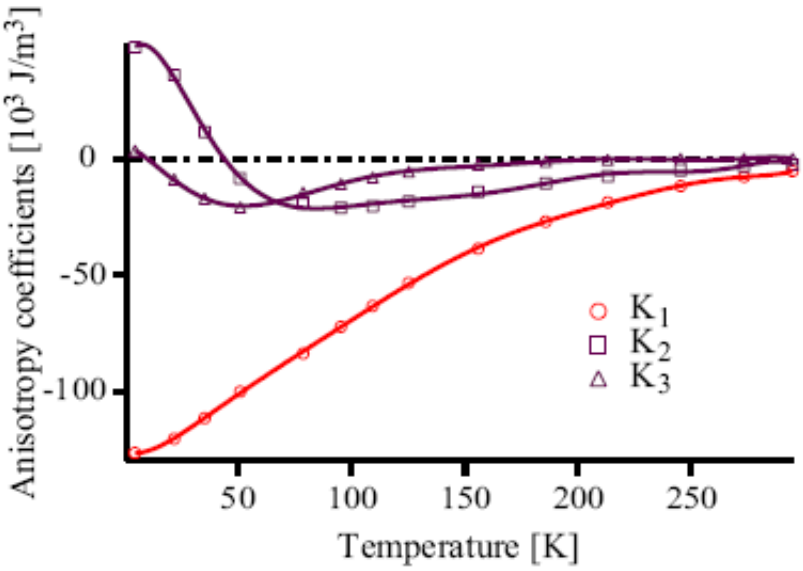

Figure 2.18: Temperature dependance of the anisotropy constants of Ni [26].

Energy Term		Ni
Magnetostatic	$\frac{1}{2}\mu_0 M_s^2$	$+0.14 \cdot 10^6$ J/m^3
Magnetocrystalline	K_1	$-4.45 \cdot 10^4$ J/m^3
Magnetoelastic	B_1	$+6.2 \cdot 10^6$ J/m^3
Magnetocrystalline≈Magnetoelastic	$\frac{K_1}{B_1}$	Strain of 0.1%
Magnetocrystalline≈Magnetoelastic	$\mu_0 \frac{M_s^2}{2B_1}$	Strain of 2.4%

Table 2.1: First order anisotropy coffcients for Ni. The two last columns represent the strain necessary to have magnetoelastic energy comparable to magnetocrystalline and magnetostatic energies [25].

Symbol		Ni	
Atomic Number		28	
Electron configuration		$[Ar]\,3d^8 4s^2$	
Crystal structure (Fig. 2.17)		fcc	
Easy magnetization axis (Fig. 2.17)		$\langle 111 \rangle$	
Magnetic coupling		ferromagnetic	
Oxide (NiO) magnetic coupling		antiferromagnetic	
Magnetic moment per atom		0.6	μ_b
Exchange energy [20]	A =	$\approx 1 \cdot 10^{-11}$	J/m
Curie Temperature		627	K
Density		8908	kg/m^3
Saturation magnetization @ 4K [27]	M_s =	$0.49 \cdot 10^6$	A/m
Saturation magnetization @ 293K [27]	M_s =	$0.52 \cdot 10^6$	A/m
Melting temperature		1726	K
Lattice constant		0.352	nm
Magnetocrystalline anisotropy coefficients @ 300K [26]	K_1 =	$-4.5 \cdot 10^3$	J/m^3
	K_2 =	$-2.3 \cdot 10^3$	
Magnetocrystalline anisotropy coefficients @ 4.2K [26]	K_1 =	$-12 \cdot 10^4$	J/m^3
	K_2 =	$3 \cdot 10^4$	
Magnetoelastic coupling cofficients @RT [20]	B_1 =	$6.2 \cdot 10^6$	Pa
	B_2 =	$4.3 \cdot 10^6$	

Table 2.2: Crystallographic, electronic, magnetic and atomic properties of nickel [25].

Chapter 3

Magnetic Force Microscopy

This chapter is aimed to give an introduction to *MFM* principles used in this thesis. Our commercial AFM/MFM system[1] is retrofitted with a coil in order to apply vertical magnetic fields (AC+DC) up to ±50 Gauss (calibrated with a Hall probe) to the samples under investigation. Also a variable magnetic field module *VFM* of the system is used for creating horizontal fields up to ±2500 Gauss (0.25 T).

3.1 Introduction to MFM

Magnetic force microscopy is a special mode of operation of the scanning force microscope [12]. The technique employs a magnetic probe, which is brought close to a sample and interacts with the magnetic stray fields near the surface. The magnetic probe is standard silicon cantilever (or silicon nitride cantilever) coated by magnetic thin film (Fig. 3.1.b). The strength of the local magnetostatic interaction affects the vertical motion of the tip as it scans across the sample. This vertical motion can be detected by various techniques, the beam deflection methode used in our commercial AFM system can be seen schematically in Fig. 3.1.a. Other system components of a magnetic-force microscope is shown in Fig. 3.2

[1]MFP-3D AFM, Asylum Research, Inc.

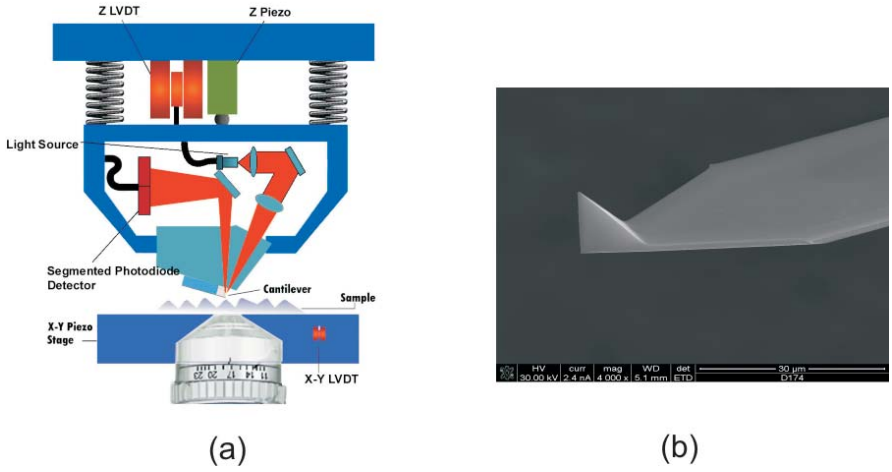

Figure 3.1: (a) Commercial AFM system with beam deflection detection. (b) A typical AFM cantilever with pyramidal tip.

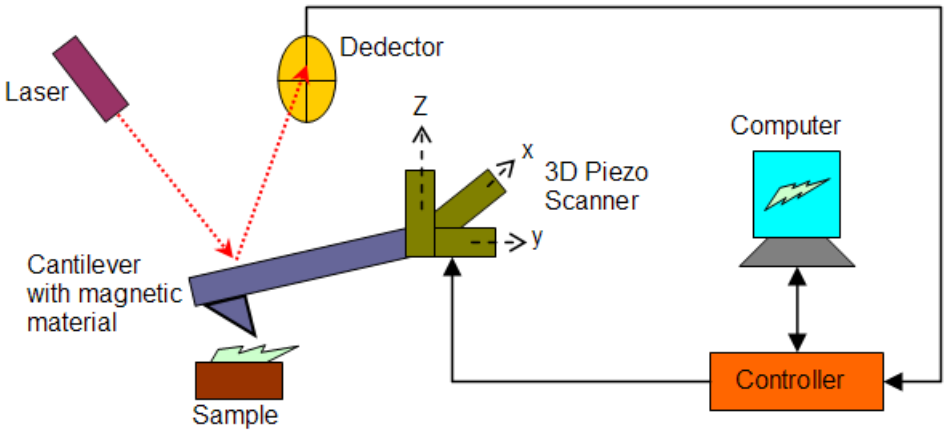

Figure 3.2: System components of a magnetic-force microscope.

Magnetic measurements are conducted by means of two-pass method to separate the magnetic image from the topography (See Fig. 3.3). As in standart non-contact [28] or semi-contact [29] AFM imaging, topography of sample is constructed at first. While cantilever is vibrating at its first resonant mode, it is raster scanned over surface, and by means of some feedback mechanism (phase, amplitude or frequency) topograpy of surface is constructed by the software. After topography measurement in the second pass the cantilever is lifted to a selected height for each scan line and the stored topography is followed (without the feedback). As a result, the tip-sample separation during second pass is kept constant. This tip-sample separation must be large enough to eliminate the van der Waals force. During second pass the cantilever is affected by long-range magnetic forces. Both the height-image and the magnetic image are obtained with this method. In the second pass two methods are available:

1. DC MFM: This MFM mode detects the deflection of a nonvibrating cantilever due to the magnetic interaction between the tip and the sample (similar to contact mode). The magnetic force acting on the cantilever can be obtained by Hook's law

$$\boxed{F_{def} = k\delta z} \tag{3.1}$$

where δz is the deflection of the cantilever and k is the cantilever force constant. In order to use this methode, the magnetic fields must be strong enough to deflect cantilver or ultrasoft cantilevers must be used.

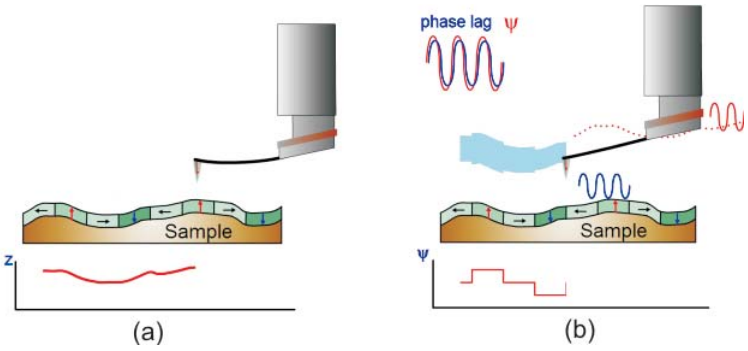

Figure 3.3: (a) 1 st pass: Topography acquisition. (b) 2nd pass : Magnetic field gradient acquisition.

2. AC MFM: During the second pass, phase shifts of resonance oscillations is used to detect the magnetic force derivative (see Fig. 3.3 [30, 12]. It is possible to record the following signals in the AC MFM for the magnetic image mapping:

   - The amplitude of cantilever oscillations.
   - The phase shift between vibrations of the piezoelectric actuator and the cantilever.

The AC MFM methods are more sensitive. A phase image of harddisk taken with AC MFM mode of our system is seen Fig. 3.4.

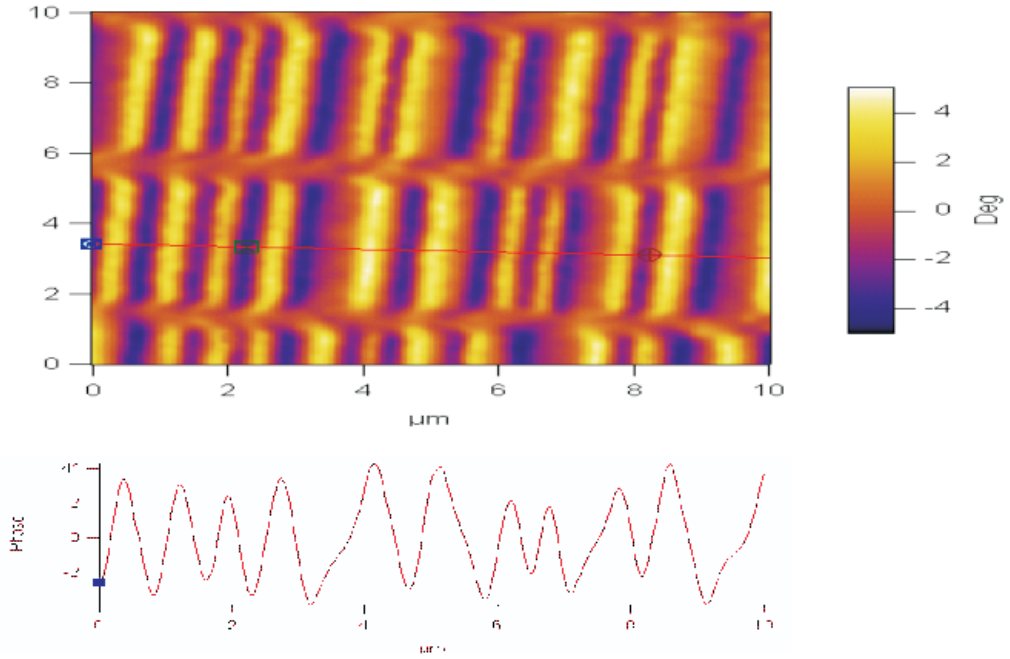

Figure 3.4: A typical MFM imaging of harddisk (Showing bits written by magnetic heads).

3.2 Cantilever Dynamics

Cantilever is an flexible beam, one end is clamped, the other is free. Motion of its free end can be satisfactorily modeled by damped simple harmonic oscillator with

sinusodial driving force. If tip-sample interaction force $F_{ts}(z)$ is also considered, vertical motion of the free end $z(t)$ can be expressed as

$$\ddot{z} + 2\delta\dot{z} + w_0^2 z = A_0 \cos\Omega t + F_{ts}(z)/m_{eff} \tag{3.2}$$

where $A_0 = F/m_{eff}$, w_0 is free resonance frequency, $m_{eff} = k/w_0^2$ is effective mass, $\delta = w_0/2Q$ is damping coefficient of the cantilever (Q is quality factor), Ω is driving frequency. For small oscillations one can write $F_{ts}(z)$ as aTaylor series expansion at point z_0 corresponding to the equilibrium position:

$$F_{ts}(z) = F_{ts}(z_0) + \frac{dF_{ts}(z_0)}{dz}\tilde{z}(t) + o(\tilde{z}(t)^2) \tag{3.3}$$

where $\tilde{z}(t)$ is expressed through $z(t)$ and z_0 as follows:

$$\tilde{z}(t) = z(t) - z_0, \tag{3.4}$$

and z_0 is determined from the following condition

$$w_0^2 z_0 = \frac{F_{ts}(z_0)}{m_{eff}}. \tag{3.5}$$

Changing $z(t)$ in Eq. 3.2 and taking into account Eq. 3.4, Eq. 3.5, we get

$$\tilde{z}'' + 2\delta\tilde{z}' + \tilde{w}^2\tilde{z} = A_0 cos\Omega t \tag{3.6}$$

where $\tilde{w} = \sqrt{\tilde{k}/m_{eff}}$ is the new frequency variable, $\tilde{k} = k - F'_{ts}$ is the effective spring constant, and $F'_{ts} = dF_{ts}/dz$ is the force gradient. A general solution of Eq. 3.6 is

$$\tilde{z}(t) = \tilde{z}_s(t) + Z_0 \cos(\Omega t + \phi) \tag{3.7}$$

where $z_s(t)$ is the solution in the absence of external force (oscillator natural damped oscillations). Due to the friction, natural oscillations are damped: $z_s(t) \to 0$ at $t \to +\infty$. Therefore, over the time $t \gg 1/\delta$ only forced oscillations will present in the system which are described by the second summand term in Eq. 3.7.

In Eq: 3.7, oscillations amplitude $\tilde{Z}_0$ and phase shift $\tilde{\phi}$ in the presence of external force gradient are given by

$$\tilde{Z}_0 = \frac{A_0}{\sqrt{(\tilde{w}^2 - \Omega^2) + \frac{w_0^2\Omega^2}{Q^2}}} \tag{3.8}$$

$$\tan\tilde{\phi} = \frac{w_0\Omega}{Q(\Omega^2 - \tilde{w}^2)}. \tag{3.9}$$

Maximum oscillation amplitude $\tilde{Z}_0$ occurs at resonant frequency $\tilde{\Omega}_R$ is

$$\tilde{Z}_{max} = \frac{2A_0Q^2}{\tilde{w}^2\sqrt{4Q^2-1}} \approx \frac{A_0Q}{\tilde{w}^2} \quad @\ \tilde{\Omega}_R = \sqrt{\tilde{w}^2 - 2\delta^2}. \tag{3.10}$$

Thus, the force gradient results in an additional shift of a vibrating system. Fig. 3.5 shows amplitude-frequency and phase-frequency curves at different values of force gradient F'_{ts}.

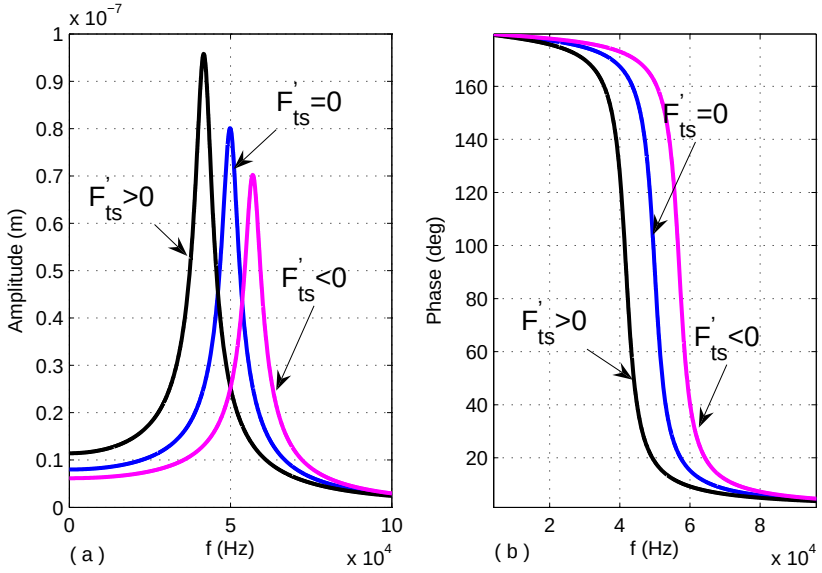

Figure 3.5: (a) Amplitude vs. Frequency curves and (b) Phase vs. Frequency at different values of force gradient F'_{ts}.

Resonant frequency $\tilde{\Omega}_R$ in the presence of external force F_{ts} can be written as

$$\tilde{\Omega}_R = w_0\sqrt{1 - \frac{F'_{ts}}{k} - \frac{1}{2Q^2}} = \sqrt{\Omega_R^2 - \frac{w_0^2F'_{ts}}{k}}. \tag{3.11}$$

Hence, the additional shift of the amplitude-frequency curve is (Fig. 3.6)

$$\Delta\Omega_R = \tilde{\Omega}_R - \Omega_R = \Omega_R\left(\sqrt{1 - \frac{w_0^2}{kF'_{ts}}} - 1\right). \tag{3.12}$$

If $\left|\frac{w_0^2}{k\omega_R^2}F'_{ts}\right| < 1$, we can further simplify Eq: 3.12

$$\boxed{\Delta\Omega_R \approx -\tfrac{w_0}{2k}F'_{ts}} \tag{3.13}$$

If oscillations occur under the driving force at frequency w_0, the phase shift is $\phi = \pi/2$. If the force gradient is present, the phase shift in accordance with Eq. 3.9 becomes:

$$\tilde{\phi}(w_0) = \arctan\left(\frac{k}{QF'_{ts}}\right). \tag{3.14}$$

If $\left|\frac{k}{QF'_{ts}} < 1\right|$, we can make a Taylors expansion of expression Eq. 3.14 as follows

$$\tilde{\phi}(w_0) = \frac{\pi}{2} - \frac{Q}{k}F'_{ts}. \tag{3.15}$$

Hence, the additional phase shift due to the force gradient is (Fig. 3.6)

$$\boxed{\Delta\phi = \tilde{\phi}(w_0) - \tfrac{\pi}{2} = -\tfrac{Q}{k}F'_{ts}} \tag{3.16}$$

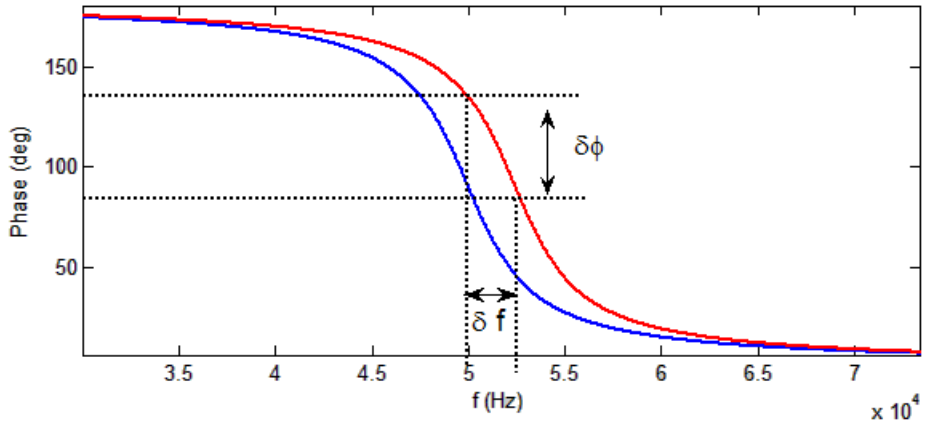

Figure 3.6: Variation of the phase of oscillations with resonant frequency.

The maximum change of ΔA in case of the resonant frequency variation (Eq: 3.13), takes place at the maximum slope of amplitude vs. frequency curve. The maximum change in oscillations amplitude in Fig. 3.7 is then

$$\boxed{\Delta A = \left(\tfrac{3A_0Q}{3\sqrt{3}k}\right)F'_{ts} \;\; @\;\Omega_A = w_0\sqrt{1-\tfrac{F'_{ts}}{k}}\left(1 \pm \tfrac{1}{\sqrt{8}Q}\right)} \tag{3.17}$$

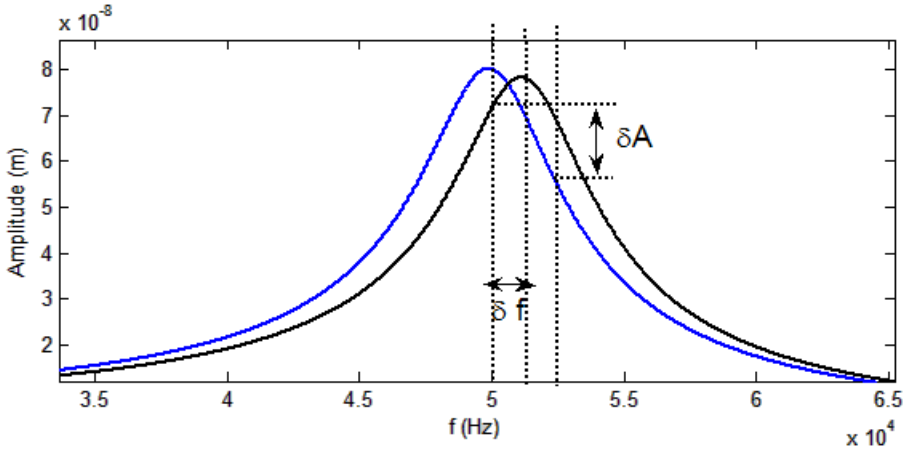

Figure 3.7: Variation of the amplitude oscillations with resonant frequency.

3.3 Tip-sample Interaction (DMT Model)

The interaction between tip and sample is determined by two regions of surface potentials, i.e. repulsive region and attractive region. The instantaneous distance between tip and sample is $D = z_s + z$ where z is the tip deflection and z_s is the distance between the undeflected cantilever and the sample. Van der Waals forces dominate the interaction in the attractive regime ($D \geq a_0$). In the repulsive regime ($D < a_0$) the tip-sample forces are calculated from the *Derjaguin-Muller-Toporov* (DMT) model [31]. For the DMT model energy dissipation due to tip-sample contact is negligible. The parameter a_0 corresponding to the interatomic distance is introduced to avoid an unphysical divergence. The tip sample forces are given by

$$F_{ts}(z) = \begin{cases} -\frac{HR}{6(z_s+z)^2} & D \geq a_0 \\ -\frac{HR}{6a_0^2} + \frac{4}{3}E^*\sqrt{R}(a_0 - z_s - z)^{3/2} & D < a_0 \end{cases} \tag{3.18}$$

where H is the Hamaker constant and R the radius of the tip. The effective contact stiffness is calculated from $E^* = [(1-\nu_t^2)/E_t + (1-\nu_s^2)/E_s]^{-1}$, where E_t and E_s are the respective elastic moduli and ν_t and ν_s the *Poisson* ratios of the tip and the sample, respectively (see the force curve in Fig: 3.8). For very small oscillations around an equilibrium position z_0, Eq: 3.18 can be linearized as

$$k_{ts} = \frac{\partial}{\partial z}F_{ts}(z)\bigg|_{z=z_0} = \begin{cases} -\frac{HR}{3(z_s+z_0)^3} & D \geq a_0 \\ 2E^*\sqrt{R}(a_0 - z_s - z)^{1/2} & D < a_0 \end{cases} \tag{3.19}$$

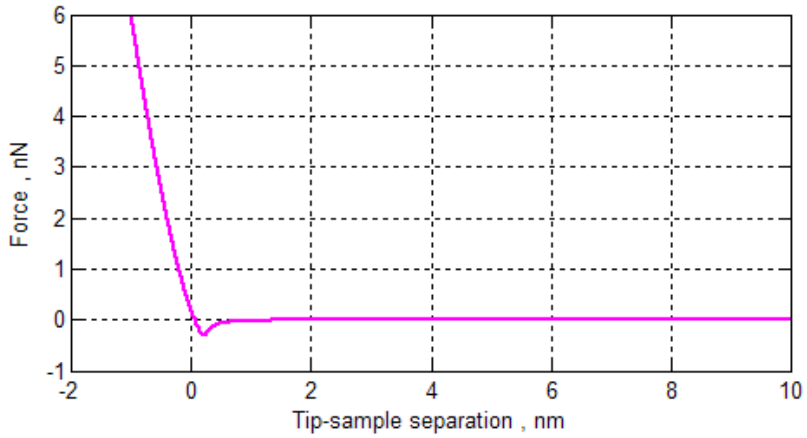

Figure 3.8: DMT force curve with parameters $E_t = 180 * 10^9$ Pa, $E_s = 10^9$ Pa, $H = 10^{-20}$ J, $a_0 = 1.36$ nm, $R = 10$ nm, $\nu = 0.3$.

3.4 Calibration of MFM Tips

In atomic force microscopy, force derivative dF/dz can originate from a wide range of sources, including electrostatic tip-sample interactions, van der Waals forces, damping, or capillary forces. However, MFM relies on those forces that arise from a long-range magnetostatic coupling between tip and sample. This coupling depends on the internal magnetic structure of the tip, which greatly complicates the explanation of contrast formation.

In general, a magnetized body, brought into the stray field of a sample, will have the magnetic potential energy E [21]

$$E = -\mu_0 \int \vec{\mathbf{M}}_{tip} \cdot \vec{\mathbf{H}}_{sample} \, dV_{tip} \tag{3.20}$$

where μ_0 is the permeability of free space. The force acting on an MFM tip can thus be calculated by:

$$F = -\nabla \cdot E = \mu_0 \int \nabla \cdot \left(\vec{\mathbf{M}}_{tip} \cdot \vec{\mathbf{H}}_{sample} \right) \, dV_{tip} \tag{3.21}$$

The integration has to be carried out over the tip volume, or rather its magnetized part. Simplified models for the tip geometry and its magnetic structure are often used in order to simplify these calculations.

A limitation in the use of MFM is that the magnetic configuration of the sensing probe is rarely known in detail. So a model of MFM tips is required. The simplest model a MFM tip is the point-tip approximation [9, 10]. The effective monopole and dipole moments of the tip are located at a certain distance away from the sample surface (Fig. 3.9). The unknown magnetic moments as well as the effective probe-sample separation are treated as free parameters to be fitted to experimental data. The force acting on the tip in the local magnetic field of the sample is given by

$$\vec{\mathbf{F}} = \mu_0(-q_{tip} + \vec{\mathbf{m}}_{tip} \cdot \nabla)\vec{\mathbf{H}}_{sample} \tag{3.22}$$

Combining both contributions, the resulting force in one dimensional case (for

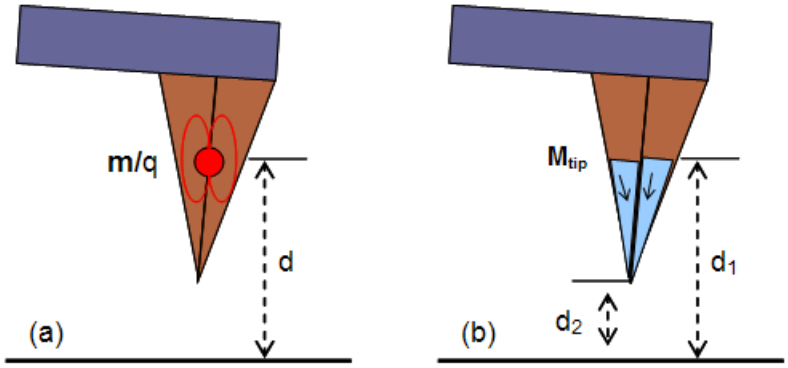

Figure 3.9: The most widespread models of MFM tips: (a) MFM tip is approximated by a single dipole $\vec{m}$ or single pole q model (b) Extended charge model. One implementation is shown, pyramidal active imaging volume with different magnetized facets.

direction $\vec{z}$) can be expressed as

$$F_z = \mu_0 \left(-qH_z + m_x \frac{\partial H_x}{\partial z} + m_y \frac{\partial H_y}{\partial z} + m_z \frac{\partial H_z}{\partial z} \right) \tag{3.23}$$

and force derivative dF/dz as

$$\frac{dF}{dz} = \mu_0 \left(-q \frac{\partial H_z}{\partial z} + m_x \frac{\partial^2 H_x}{\partial z^2} + m_y \frac{\partial^2 H_y}{\partial z^2} + m_z \frac{\partial^2 H_z}{\partial z^2} \right) \tag{3.24}$$

When the frequency that drives the MFM tip is kept constant, using Eq: 3.16 and Eq: 3.24 the phase shift due to the force between the sample stray field and the MFM tip can be expressed as

$$\Delta\Phi = -\mu_0 \frac{Q}{k}\left(-q\frac{\partial H_z}{\partial z} + m_x\frac{\partial^2 H_x}{\partial z^2} + m_y\frac{\partial^2 H_y}{\partial z^2} + m_z\frac{\partial^2 H_z}{\partial z^2}\right) \tag{3.25}$$

where Q is the quality factor of the MFM tip cantilever resonance, k is the spring constant of cantilever, q is the effective magnetic mopole of the tip, m_i is the effective dipole moment of the tip, and H_z is the vertical component of the sample stray field. Assuming magnetic moment of tip has m_z component only, we can consider only the terms with H_z.

Using these models MFM tips are calibrated with current carrying metal stripes or coils which produce well controllable and regular magnetic fields [9, 10, 11]. Generally magnetic fields have an analytic form which can be used to fit experimantal data. These metal stripes or coils are manufactured by e-beam lithography which enables submicron features.

3.5 External Magnetic Field Sources

In cantilever magnetometry (see Chapter 5), variable field module (VFM) of the MFM system was used for generating in-plane fields of ±2500 Gauss. VFM relies on a rare-earth permanent magnet to apply a field to the sample. By rotating the magnet, different amounts of magnetic flux through the gap can be adjusted (Fig. 3.10). The magnet rotation is controlled by a motor and various rate of rotation, i.e. rpms, can be selected.

For applications of vertical AC/DC magnetic fields of ±50 Gauss, voice coil of head actuator (removed from a hard disk drive) is used. It was placed on sample plate of MFM system. Calibration of this coil was done by using a Hall sensor with reference to applied excitation voltage . Calibration data with linear curve fit

$$B_{ver} = 10.29V + 3.429 \text{ (Gauss)} \tag{3.26}$$

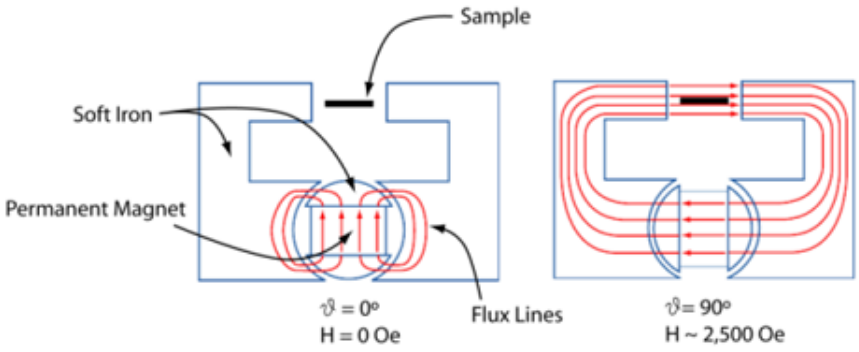

Figure 3.10: The strength and sign of the magnetic field applied to the sample depends on the rotation angle of the magnet [32].

is shown on Fig. 3.11. V is excitation voltage applied by a function generator (Standford Reseach Systems, DS345). Hall sensor was found to have an offset of 3.429 Gauss.

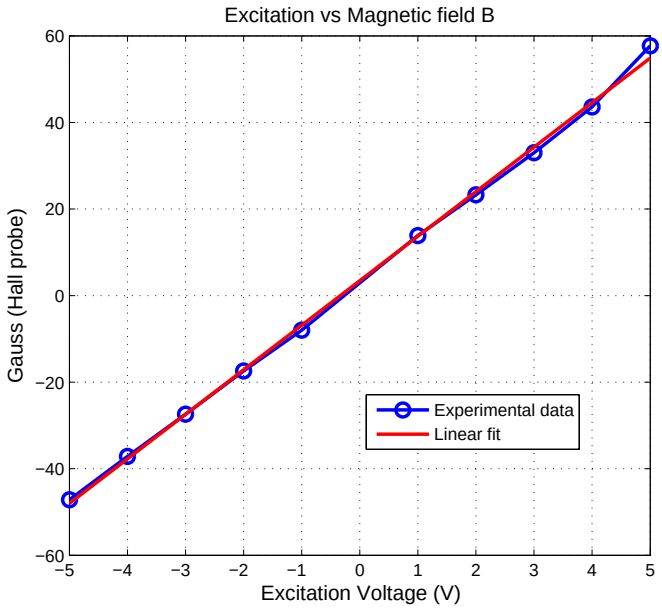

Figure 3.11: Calibration of the coil creating vertical magnetic field was done using a Hall sensor with reference to applied exitation voltage.

Chapter 4

Multifrequency Imaging Methods in SPM

The current interpretation of AFM is based on point-mass models [33], i.e., the cantilever-tip system is considered as a damped harmonic oscillator having single resonance frequency. This approximation has been successful to describe the complex nonlinear dynamics of cantilever. However, point-mass models ignore higher oscillation modes of the cantilever. When spectral characteristics of the AFM signal is analysed, a broad band signal of higher harmonics can be observed. If the nonlinearity of the tip-sample interaction, and the multiple flextural modes of the cantilever are taken into account, then a deeper understanding of the AFM signal can be reached.

4.1 Multimodal Model of AFM Cantilever

The equation of motion for the flexural vibrations of a freely vibrating and undamped cantilever beam can be approximated by the EulerBernoulli equation [33, 34]

$$EI\frac{\partial^4 z(y,t)}{\partial y^4} + \rho A\frac{\partial^2 z(y,t)}{\partial t^2} = 0 \tag{4.1}$$

where $z(y,t)$ is the vertical displacement, y is the position along the cantilever, t is the time , E is the modulus of elasticity, I is the area moment of inertia, ρ is the volume density, and A is the uniform cross sectional area of the cantilever. By assuming solution of form $z(y,t) = \phi(y)\cos(w_n t)$, it is found that the resonant frequency of the nth eigenmode w_n is related to the respective eigenvalues κ_n by

$$EI\kappa_n^4 - \rho A w_n^2 = 0. \tag{4.2}$$

The modal shapes $\phi(y)$ are determined by imposing boundary conditions (clamped-free) for solutions. The cantilever is clamped at $y = 0$. The boundary conditions are $\phi(0) = 0$ for the displacement and derivative of displacement $\phi'(0) = 0$ for the deflection slope. At $y = L$ the cantilever is free, there are no external torques or shear forces; $\phi''(L) = 0$ and $\phi'''(L) = 0$, respectively. The

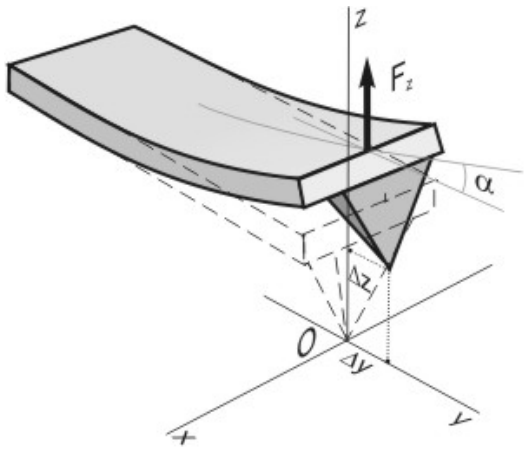

Figure 4.1: Cantilever as an extended object (rectangular beam) [30].

eigenvalues can be obtained from the characteristic equation which is found after appling boundary conditions on modal shapes

$$\cos\kappa_n L \cosh\kappa_n L = -1. \tag{4.3}$$

Solutions for the first five wavenumbers are $\kappa_n L = 1.875$, 4.694, 7.855, 10.996, 14.137 (n=1,2,3,4,5). The eigenvectors of the free cantilever are given by:

$$\phi_n(y) = \frac{R}{2}\left[\cos(\kappa_n y) - \cosh(\kappa_n y) - \frac{\cos(\kappa_n L) + \cosh(\kappa_n L)}{\sin(\kappa_n L) + \sinh(\kappa_n L)}\left(\sin(\kappa_n y) - \sinh(\kappa_n y)\right)\right] \tag{4.4}$$

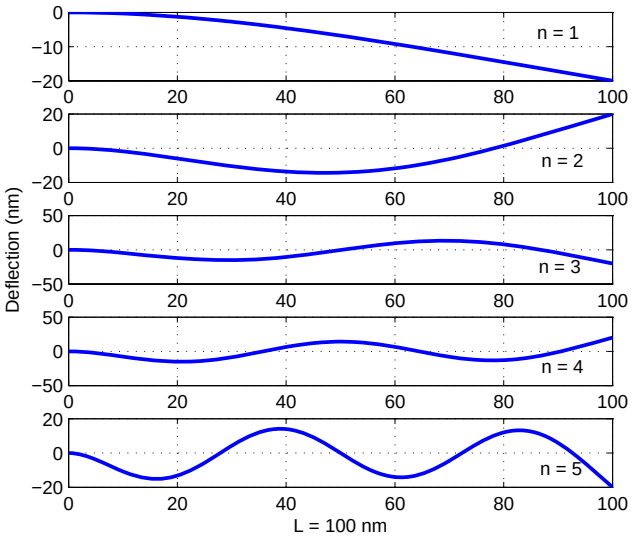

Figure 4.2: Illustration of the first five flexural eigenmodes of a freely vibrating cantilever beam.

where R is amplitude. The rectangular beam and its first five flexural eigenmodes are illustrated in Fig. 4.1 and Fig. 4.2, respectively.

Euler-Bernoulli partial differential equation of the cantilever can be also approached by a system of n second order differential equations, one for each eigenmode of the cantilever [15]. We also assume that dynamics of the system is mostly contained in the first two eigenmodes. Then we obtain a system of two differential equations (See Fig. 4.3),

$$m_1\ddot{z}_1 = -k_1 z_1 - \frac{m_1 w_1}{Q_1}\dot{z}_1 + F_1 \cos w_1 t + F_2 \cos w_2 t + F_{ts}(z_1 + z_2) \tag{4.5}$$

$$m_2\ddot{z}_2 = -k_2 z_2 - \frac{m_2 w_2}{Q_2}\dot{z}_2 + F_1 \cos w_1 t + F_2 \cos w_2 t + F_{ts}(z_1 + z_2) \tag{4.6}$$

where $m_i = k_i/w_i^2$ is the effective mass of mode i; Q_i, k_i, A_{0i}, F_i, and $w_i = 2\pi f_i$ are, respectively, the quality factor, force constant, free amplitude, external excitation force ($F_i = k_i A_{0i} Q_i$), and angular frequency of the i eigenmode. The solution of the above system can be approached by,

$$z(t) = z_1(t) + z_2(t) \approx A_1 \cos(w_1 - \phi_1) + A_2 \cos(w_2 - \phi_2) \tag{4.7}$$

where A_i is the amplitude and ϕ_i is the phase shift of the i^{th} eigenmode.

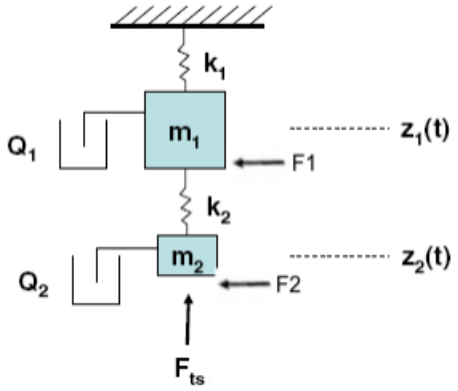

Figure 4.3: (a) Mechanical model for first two modes of cantilever as a coupled two harmonic oscillators [35].

4.2 Multifrequency Exitation and Imaging

In multi-frequency imaging methode, the cantilever is both driven and measured at two (or more) frequencies [33, 36]. To drive cantilever a sum of voltages at frequencies f_1 and f_2 is generally applied on shake piezo. But there are also other means of driving the mechanical oscillations, i.e. using the electrical force between biased tip and sample [37] or the magnetic force created by a coil on a small magnet attached to tip [38]. AC deflection contains information at both of those frequencies, as shown in Fig. 4.4. The output of the lockin amplifiers, polar amplitudes and phases (A_1, ϕ_1, A_2, ϕ_2,...) of two or more frequencies can be used for imaging or can be combined with other signals and used in feedback loops.

The controller can use one or both of the resonant frequencies to operate a feedback loop. If the amplitude of the fundamental frequency A_1 is used as the feedback error signal, then fundamental phase ϕ_1, the second resonant frequency amplitude A_2 and phase ϕ_2 can be used as an independant source channels. So while measuring the topography, some other kind of physical feature of sample, such as contact potential difference in Kelvin Probe Microscopy [39] or charging hysteresis of silicon nanocrystals as in Electrostatic Force Microscopy [37], can be simultaneously acquired. Amplitude and phase of higher frequency modes can show an increased contrast on the sample [29] or a strong dependence on a

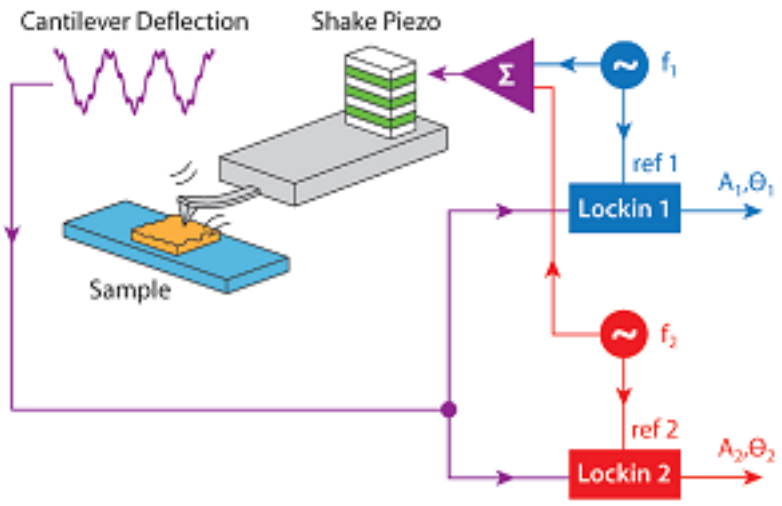

Figure 4.4: In multi-frequency imaging, the cantilever is both driven and measured at two (or more) frequencies of resonant flextural modes. [36]

physical parameter such as Hamaker constant of the sample [40].

Chapter 5

Fluxgate and Cantilever Magnetometry

Fluxgate principle is used to measure local field strength B_{sample} of the samples in this thesis, so a brief introduction to this principle is given in the first section of this chapter. Cantilever magnetometry is used extensively to characterize the MFM tips fabricated by FIB operations. Coercive field, total magnetic moment are physical parameters which can be measured by experimental fitting to the results of Cantilever Magnetometry. Simulations results with two working conditions, which we call characterization and measurement configurations, will be given and comparisons with actual experimental data will be made later in Chapter 5.1.

5.1 Fluxgate Magnetometry

Fluxgate principle is the working principle of Fluxgate Magnetometers [41, 42, 43, 44] which are sensors designed to measure magnetic fields. The most basic fluxgate detector is the single core sensor which consists of a nonlinear core (a soft magnetic material) surrounded by excitation and sensing coils. The geometry of configuration is shown in Fig. 5.1.

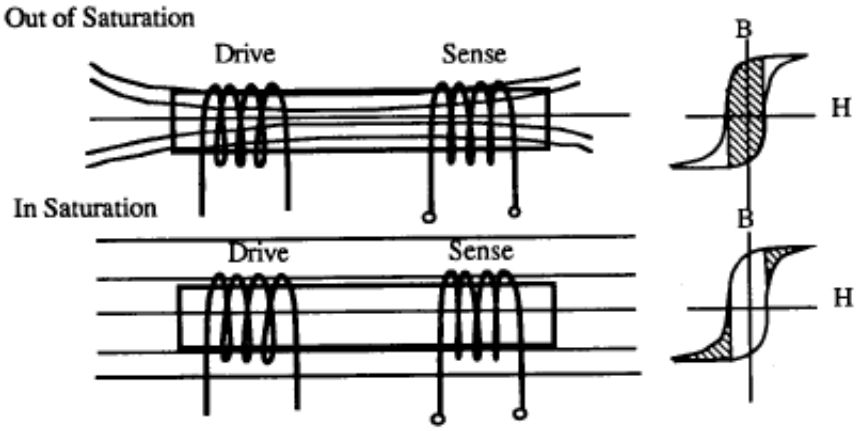

Figure 5.1: The fluxgate magnetometer configuration and operation. [41]

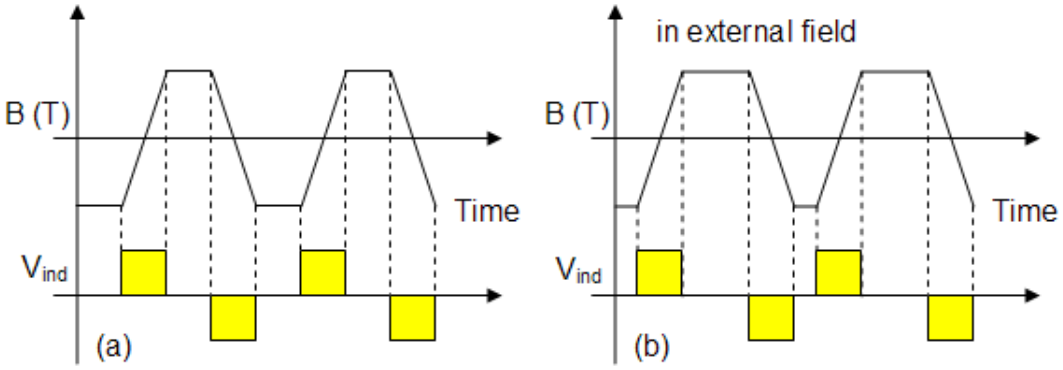

Figure 5.2: A typical fluxgate signal (a) at the absence of external field (b) at the presence of external field [45].

The excitation coils are driven by an alternating current that produces a magnetic field which varies the permability of core. The core saturated equally in both directions by the positive and negative cycles of excitation current in the absence of external field. The induced voltage at pick-up coils which is a result of *Faraday's Law* is thus symmetric (see Fig. 5.2.a).

When an external magnetic field H_{ex} is present, hysterisis curve of magnetic core will shift in the direction of external field H_{ex}. So the field produced by the excitation current will have an offset which will unbalance the time intervals during which the core is saturated. Induced voltage will be asymmetric in this case and can be used to measure external field H_{ex} (see Fig. 5.2.b).

5.2 Cantilever Magnetometry

Magnetic properties of nanoscale samples can be characterized using the technique of *Cantilever Magnetometry*. In this technique, sample is placed, attached or deposited on cantilever [46], and an external magnetic field is applied on sample-cantilever system. There are differents ways of conducting magnetometry measurements. In a DC magnetic field, torque on sample causes a deflection which can be used for magnetic measurements [47]. In an alternating gradient magnetometer (AGM) [48], an AC magnetic field gradient is applied and resultant amplitude of oscillations is used. Magnetometry measurements can also be made by measuring the resonant frequency of vibrating cantilevers in a DC magnetic field. Shifts in resonant frequency of cantilever oscillations give information about magnetic properties [49]. But in this technique, ultra-soft and high Q cantilevers must be used. So measurements are conducted in cyrogenic temperatures and under high vacuum conditions.

In this thesis, a different technique is used for cantilever magnetometry and measurements with standart cantilevers can be conducted in normal vacuum conditions and at room temperatures. Driving cantilever directly applying torque with uniform AC magnetic field in an adjustable horizontal DC magnetic field, changes in the magnetic states of sample can be translated into amplitude and phase variations. Characterization of FIB tailored tips (Chapter 6.1) can be made in *characterization configuration* and fluxgate magnetic field measurements can be made in *measurement configuration*.

5.2.1 Characterization Configuration

In characterization configuration, a vertical AC magnetic field (max. 10 Gauss) is used to oscillate the *cantilever-magnetic particle* system which has initial tilt angle θ_{eq}. Also a DC magnetic field ($\pm$2500 Gauss) is applied to deflect cantilever some angle θ from initial tilt (see Fig. 5.3). Magnetic particle is assumed to be a single domain Stoner-Wohlfarth particle [18] and have effective uniaxial

magnetic anisotropy. This anisotropy axis (magnetic easy axis) is also assumed to be oriented along the long symetry axis of the particle. As seen in Chapter 2.2, effective uniaxial magnetic unisotropy energy includes contributions from shape anisotropy energy (e_{MS}), magnetoelastic unisotropy energy (e_{ME}) and uniaxial magnetocrystalline unisotropy energy (e_{MC}). So effective magnetic anisotropy energy density e_{AN} can be written in terms of [18, 25]

$$\begin{aligned} e_{AN} &= e_{MC} + e_{MS} + e_{ME} = K_{eff} \sin^2 \phi \\ K_{eff} &= K_{MC} + K_{MS} + K_{ME} \\ E_{AN} &= K_{eff} V \sin^2 \phi \end{aligned} \tag{5.1}$$

where ϕ is the angle between magnetic easy axis $\vec{x}$ and total magnetic moment $\vec{m}$ of particle, and E_{AN} is total effective magnetic anisotropy energy of particle whose volume is V.

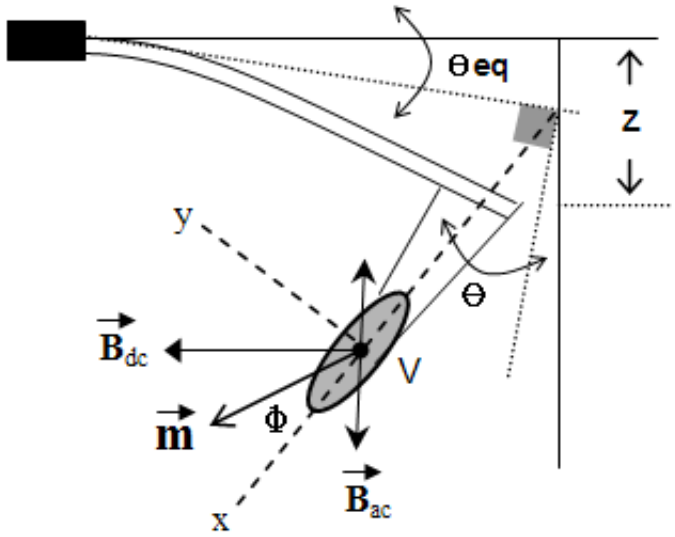

Figure 5.3: The cantilever magnetometry configuration used for characterization of magnetic tips. Magnetic moment $\vec{m}$ of single domain particle tilts some ϕ angle from easy axis $\vec{x}$ in a horizontal DC magnetic field $\vec{B}_{DC}$.

After some external DC magnetic field $\vec{B}_{DC}$ is applied, coherent rotation takes place and total magnetic moment $\vec{m}$ of particle tilts ϕ angle from easy axis $\vec{x}$ according to *Stoner-Wohlfarth* Model (Fig: 5.3). For the coordinate system shown in Fig. 5.3, total magnetic moment $\vec{m}$ of particle and applied DC magnetic

field $\vec{B}_{DC}$ can be written as

$$\vec{B}_{DC} = B_{DC}\left\{\sin(\theta_{eq}+\theta)\vec{i} + \cos(\theta_{eq}+\theta)\vec{j}\right\} \tag{5.2}$$

$$\vec{m} = M_s V\left\{\cos(\phi)\vec{i} + \sin(\phi)\vec{j}\right\} \tag{5.3}$$

where M_s is saturation magnetization and V is volume of the particle. The Zeeman Energy of particle can be written using Eq. 5.2 and Eq. 5.3 as

$$\begin{aligned} E_{Zeeman} &= -\vec{m}\cdot\vec{B}_{DC} \\ &= -M_s V B_{DC}\left[\cos\phi\sin(\theta_{eq}+\theta) + \sin\phi\cos(\theta_{eq}+\theta)\right] \\ &= -M_s V B_{DC}\sin(\theta_{eq}+\theta+\phi). \end{aligned} \tag{5.4}$$

The energy stored at cantilever deflected some angle θ from equilibrium tilt angle θ_{eq} is

$$E_{canti} = \frac{1}{2}kz^2 = \frac{1}{2}k(L_{eff}\theta)^2 \tag{5.5}$$

where static effective length $L_{seff} = L/\alpha_S$ of cantilever is defined by $\alpha_S = 1.5$, i.e. static deflection parameter which is calculated by using beam theory [50] (see Fig. 5.4).

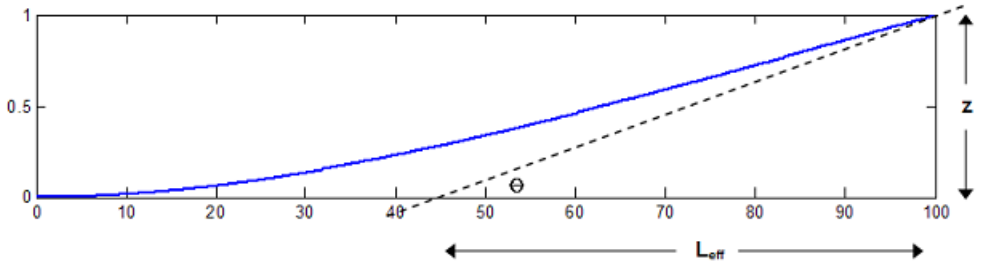

Figure 5.4: The slope of static deflection at the end of cantilever is used for calculation of effective length L_{seff}

The rotation of magnetic moment of particle and new equilibrium deflection of cantilever can be found by mimimizing the total energy $U(\theta,\phi)$ of system which is sum of effective magnetic anisotropy energy (Eq. 5.1), Zeeman energy (Eq. 5.4), and stored energy of deflected cantilever (Eq. 5.5)

$$U(\theta,\phi) = -M_s V B_{DC}\sin(\theta_{eq}+\theta+\phi) + K_{eff}V\sin^2\phi + \frac{1}{2}k(L_{seff}\theta)^2 \tag{5.6}$$

M_s	$0.52 \cdot 10^6$	Am^2
V	$1.18 \cdot 10^{-18}$	m^3
K_{eff}	$8.39 \cdot 10^4$	$\mathrm{J/m}^3$
k	10	N/m
Q	200	-
L	$150 \cdot 10^{-6}$	m
L_{eff}	L/α	m
L_{deff}	L/α_n	m
θ_{eq}	11^o	deg
B_{DC}	± 0.225	T
B_{AC}	± 0.5	mT

Table 5.1: Parameter values used in the cantilever magnetometry simulations are listed. See text for definitions of L/α and L/α_n parameters.

with respect to θ and ϕ. The equilibrium angles θ' and ϕ' must satisfy the conditions

$$\left.\frac{\partial U(\theta,\phi)}{\partial\theta}\right|_{\theta=\theta',\phi=\phi'} = 0 \quad and \quad \left.\frac{\partial U(\theta,\phi)}{\partial\phi}\right|_{\theta=\theta',\phi=\phi'} = 0. \tag{5.7}$$

Putting Eq. 5.6 in equilibrium conditions Eq. 5.7 and solving two resultant equation, we can find the relation between equilibrium values of θ and ϕ as

$$\theta = \frac{K_{eff}V}{kL_{seff}^2}\sin 2\phi. \tag{5.8}$$

Total energy of the system now can be written in terms of one variable ϕ after replacing θ with Eq. 5.8.

$$U(\phi) = -M_sVB_{DC}\sin(\theta_{eq} + n\sin 2\phi + \phi) + K_{eff}V\sin^2\phi$$

$$+ \frac{1}{2}k(L_{seff}n\sin 2\phi)^2 \tag{5.9}$$

where the proportionality coefficient $n = K_{eff}V/kL_{seff}^2$ is written instead. Total energy profiles at increasing or decreasing B_{DC} field values are shown in Fig. 5.5, and Fig. 5.6. Evolution of mimimum the points is in the direction of arrows. Parameters used for the simulations are listed in Tab. 5.1.

Taking initial conditions as $\phi = 0$ and $B_{DC} = 0$, successive calculations of new equilibrium angles ϕ' can be made numerically. The experimental B field

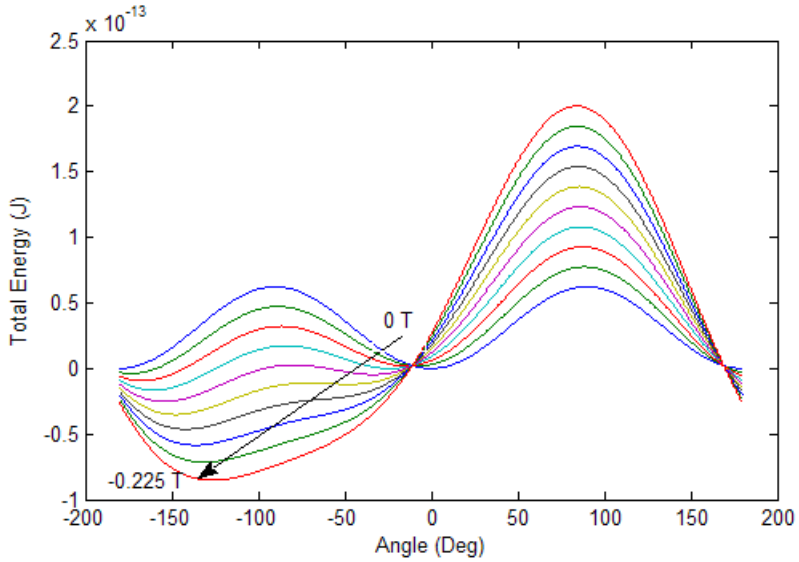

Figure 5.5: Total energy profile and moving equilibrium points at decreasing field values ($0 \rightarrow -0.225$ Tesla).

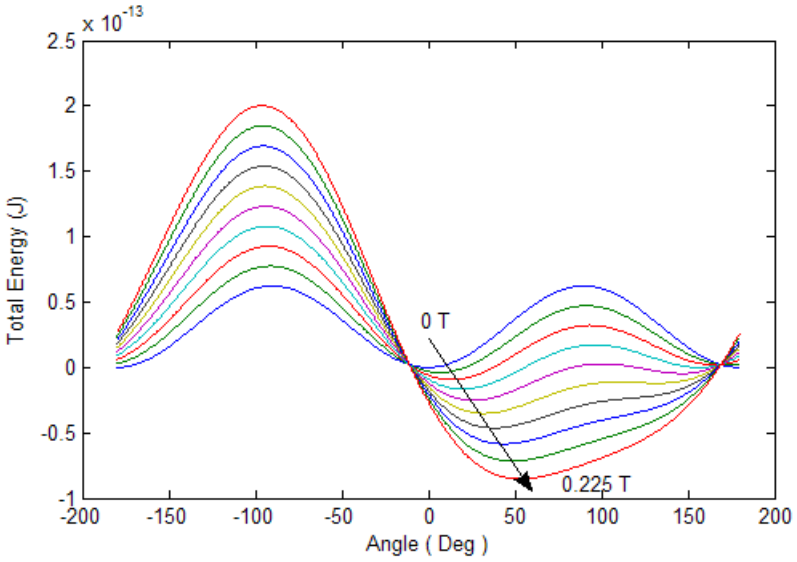

Figure 5.6: Total energy profile and moving equilibrium points at increasing field values ($0 \rightarrow 0.225$ Tesla).

curve shown in Fig. 5.7(a) was used for simulations. Time evolution of angle ϕ shown in Fig. 5.7(b) has sharp falls which are unstable points. Consequently a hysteresitic behaviour as shown in Fig. 5.8 happens. Also path of stable points on total energy surface can be seen in Fig. 5.9.

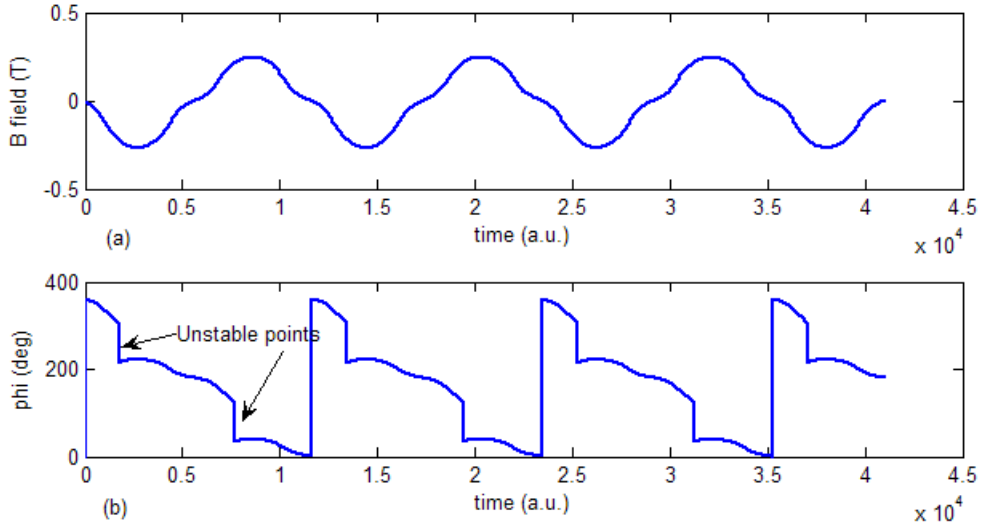

Figure 5.7: (a)The experimentally applied quasi-sinusoidal magnetic field B_{DC} shown in figure is used in simulations. (b) Unstable points are sudden change of angle ϕ (except 0-2π)

Change of magnetic state of the particle can be translated to amplitude and phase variations of cantilever oscillations if a vertical AC magnetic field $\vec{B}_{AC}$ of frequency Ω

$$\vec{B}_{AC} = B_{AC}\cos(\Omega t)\left\{-\cos(\theta_{eq}+\theta)\vec{i}+\sin(\theta_{eq}+\theta)\vec{j}\right\} \tag{5.10}$$

is applied on cantilever-particle system (see Fig. 5.3). It is assumed that small values of $\vec{B}_{AC}$ (0-10 Gauss) have negligible effect on the magnetic state of particle. To increase sensitivity, a resonant mode frequency is generally chosen. The alternating magnetic field applies an alternating torque on particle which drives cantilever. Kinematically equivalent force $\vec{F}_{eq} = \vec{\tau}/L_{deff}$ of this torque $\vec{\tau}$ can be calculated if dynamic effective length L_{deff} of cantilever is known as shown for only 2$^{\text{nd}}$ flextural mode in Fig. 5.10.

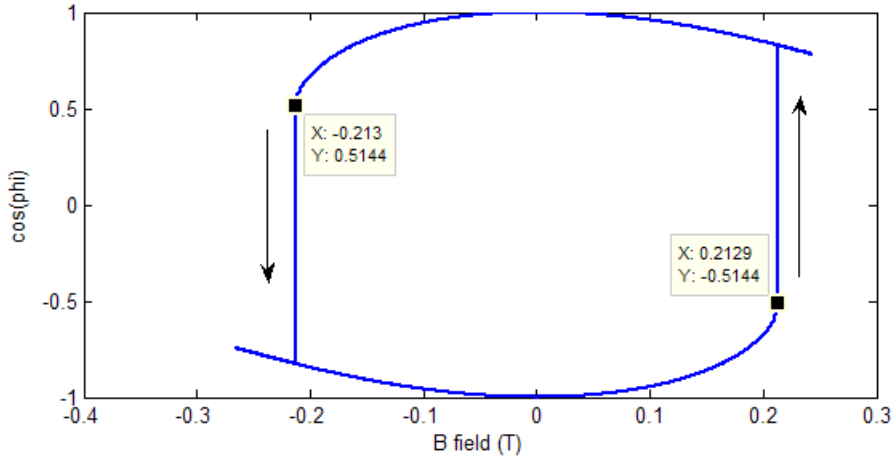

Figure 5.8: Easy axis component $\cos\phi$ of total magnetic moment $\vec{m}$ shows similar easy axis type hysteresis.

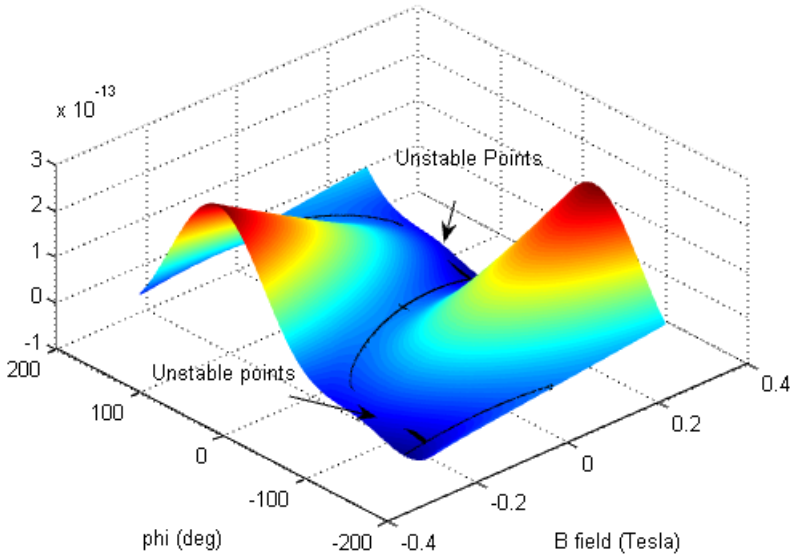

Figure 5.9: Total energy surface of cantilever-magnetic particle system. Path of stable equilibrium points is the black curve on the energy surface. Unstable points where Barkhausen jumps take place also are shown in figure.

The vertical displacement $z(y)$ and angular deflection $dz(y)/dz$ of vibrating beam is given by [14]

$$z(y) = \frac{A}{2}\left[\cos(\kappa_n y) - \cosh(\kappa_n y) - B\left(\sin(\kappa_n y) - \sinh(\kappa_n y)\right)\right] \tag{5.11}$$

$$\frac{dz(y)}{dy} = \frac{A\kappa_n}{2}\left[-\sin(\kappa_n y) - \sinh(\kappa_n y) - B\left(\cos(\kappa_n y) - \cosh(\kappa_n y)\right)\right] \tag{5.12}$$

$$B = \frac{\cos(\kappa_n L) + \cosh(\kappa_n L)}{\sin(\kappa_n L) + \sinh(\kappa_n L)} \tag{5.13}$$

where length L of cantilever and κ_n wave number of n^{th} vibration mode satisfy clamped-free boundary conditions $\cos(\kappa_n L)\cosh(\kappa_n L) = -1$ [34]. So dynamic effective length of cantilever can be defined by $L_{deff} = L/\alpha_{dn}$ using α_{dn} parameter which satisfies the equation

$$\left.\frac{dz(y)}{dy}\right|_{y=L} = \frac{\alpha_{dn} z(L)}{L} = \frac{z(L)}{L_{deff}}. \tag{5.14}$$

α_{dn} values for first four flextural modes of cantilever are 1.377, 4.788, 7.849, 11.996 [51].

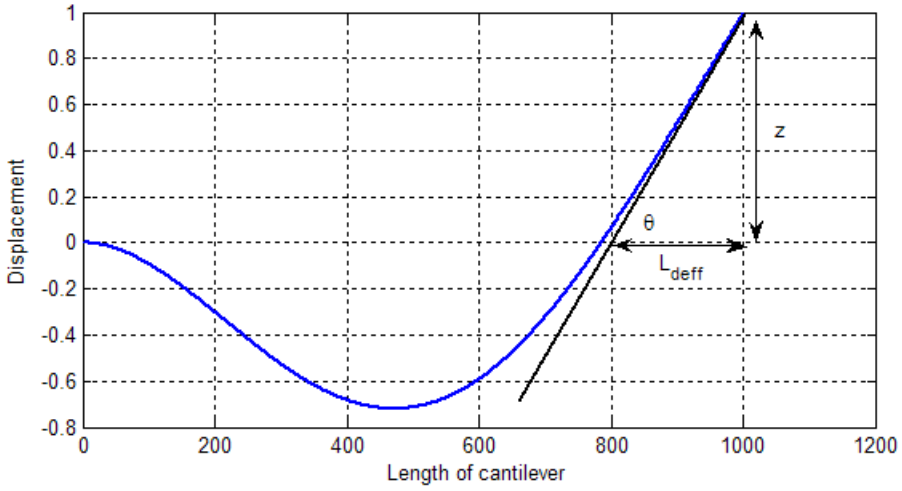

Figure 5.10: Dynamic effective length L_{deff} of second flextural mode of cantilever.

The torque on cantilever in field $\vec{B}_{AC}$ (Eq. 5.10) is

$$\begin{aligned}\vec{\tau} &= \vec{m} \times \vec{B}_{AC} \\ &= M_s V B_{AC} cos(wt)\left[\cos\phi \sin(\theta_{eq}+\theta) + \sin\phi\cos(\theta_{eq}+\theta)\right]\vec{k} \\ &= M_s V B_{AC} sin(\theta_{eq}+\theta+\phi) cos(\Omega t)\vec{k}.\end{aligned} \tag{5.15}$$

So kinematically equivalent driving force F_{eq} is

$$F_{eq} = \frac{|\vec{\tau}|}{L_{deff}} = \frac{M_s V B_{AC} sin(\theta_{AC} + \theta + \phi)}{L_{deff}} cos(\Omega t). \tag{5.16}$$

Effective spring constant k of cantilever vibrating in magnetic field $\vec{B}_{DC}$ is also changed. The change of k can be calculated using second derivative of total energy of the system (Eq. 5.6) and $\theta = z/L_{seff}$ as

$$k_{eff} = \frac{\partial^2 U}{\partial^2 z} = \frac{1}{L_{seff}^2} \left.\frac{\partial^2 U}{\partial^2 \theta}\right|_{\theta=\theta',\phi=\phi'} = \frac{M_s V B_{DC}}{L_{eff}^2} sin(\theta_{eq} + \theta' + \phi') + k \tag{5.17}$$

where θ' and ϕ' are the equilibrium angles calculated numerically. After determination of the effective spring constant k_{eff} (Eq. 5.17) and the torque equivalent force F_{eq} (Eq. 5.16) on the cantilever, equation of motion is turned out to be

$$\ddot{z} = -\frac{w_0}{Q}\dot{z} - \left(\frac{M_s V B_{DC}}{L_{seff}^2 m} sin(\theta_{eq} + \theta' + \phi') + \frac{k}{m}\right) z$$
$$+ \frac{M_s V B_{AC} sin(\theta_{eq} + \theta' + \phi')}{L_{deff} m} cos(\Omega t). \tag{5.18}$$

From the solution of equation of motion Eq. 3.8, amplitude R is

$$R = \frac{M_s V B_{AC} \left|\sin(\theta_{eq} + \theta' + \phi')\right| w_0^2 / k L_{deff}}{\sqrt{\left(\frac{M_s V B_{DC} \sin(\theta_{eq}+\theta'+\phi') w_0^2}{L_{eff}^2 k} + w_0^2 - \Omega^2\right)^2 + \frac{w_0^2 \Omega^2}{Q^2}}} \tag{5.19}$$

and phase ψ (See Eq. 3.9) is

$$\tan(\psi - \epsilon\,\pi) = \frac{w_0 \Omega}{Q\left(\Omega^2 - w_0^2 - M_s V B_{DC} \sin(\theta_{eq} + \theta' + \phi') w_0^2 / k L_{eff}^2\right)} \tag{5.20}$$

where $\epsilon = 1$ if $\theta_{eq} + \theta' + \phi' < 0$, otherwise $\epsilon = 0$. If we drive the cantilever at the zero-field ($B_{DC} = 0$) resonance frequence of $\Omega = w_0\sqrt{1 - 1/2Q^2}$, amplitude R and phase ψ can be rewritten independent of natural frequency w_0 as

$$R = \frac{M_s V B_{AC} \left|\sin(\theta_{eq} + \theta' + \phi')\right| / k L_{deff}}{\sqrt{\left(\frac{M_s V B_{DC} \sin(\theta_{eq}+\theta'+\phi')}{k L_{eff}^2} + \frac{1}{2Q^2}\right)^2 + \frac{1}{Q^2}\left(1 - \frac{1}{2Q^2}\right)}} \tag{5.21}$$

$$\tan(\psi - \epsilon\,\pi) = -\frac{\sqrt{1 - \frac{1}{2Q^2}}}{\frac{1}{2Q} + \frac{Q M_s V B_{DC}}{k L_{eff}^2} \sin(\theta_{eq} + \theta' + \phi')}. \tag{5.22}$$

Simulations were made for different values of effective magnetic anisotropy constant $K_{eff} = 5 \cdot 10^4,\ 7 \cdot 10^4,\ 9 \cdot 10^4,\ 1 \cdot 10^5,\ 2 \cdot 10^4,\ 4 \cdot 10^4$ J/m^3. The effect of different values of K_{eff} can be seen in Fig. 5.11. As K_{eff} decreases, coercive field H_c decrease. For some range of values of K_{eff}, hysteresis comes to play. Amplitude and phase of signals with or without hysteresis can be seen in Fig. 5.12, Fig. 5.14. Amplitude and phase of signals versus applied field B_{DC} with or without hysteresis can be seen in Fig. 5.13 and Fig. 5.15.

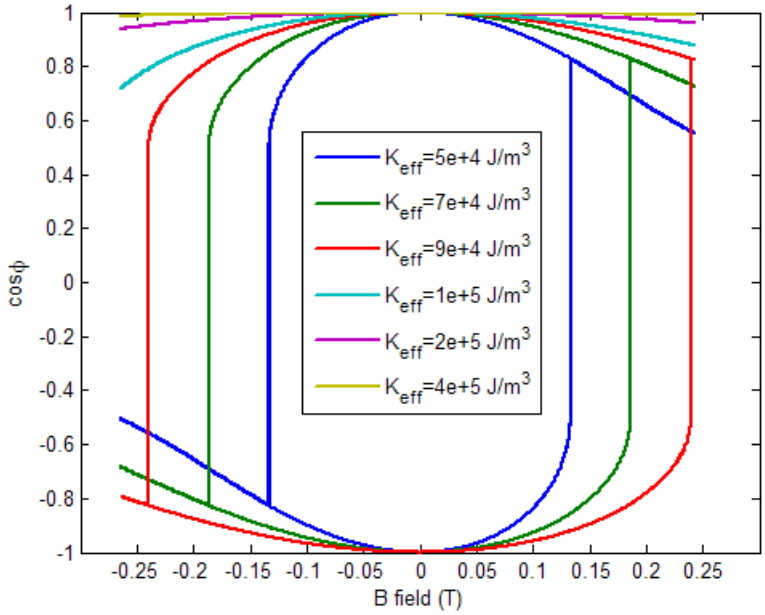

Figure 5.11: Easy axis type hysteresis curves with different values of magnetic anisotropy constant K_{eff}.

In derivation of equations Eq. 5.9 and Eq. 5.18, too much simplifications and assumptions about shape, orientation and type of magnetic anisotropy of the particle were made. In a realistic experiment, shape and crystalline anisotropy axises can be at an arbitrary orientation with respect to coordinate system of the cantilever tip whose $\hat{x} - \hat{z}$ plane is where oscillation takes place and magnetic fields are applied. Therefore a general configuration shown in Fig. 5.16 is used for modeling and 3D simulations [52].

Total magnetic moment $\vec{m}$ of the particle can be described in terms of direction

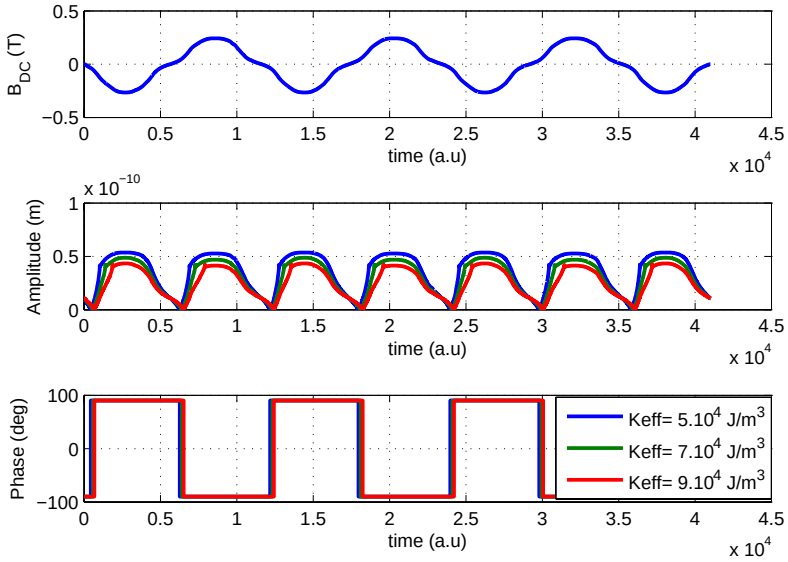

Figure 5.12: Calculated amplitude and phase of oscillation versus time curves with different values of magnetic anisotropy constant K_{eff} (with hysteresis).

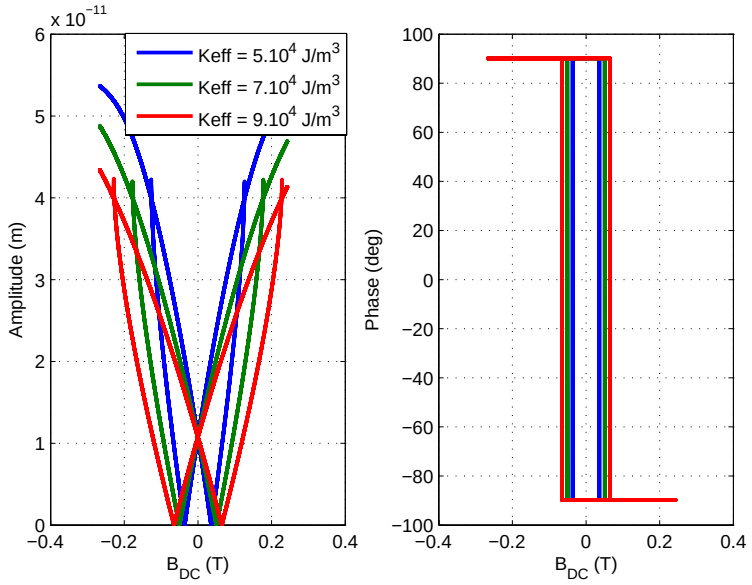

Figure 5.13: Calculated amplitude and phase of oscillation versus B_{DC} field curves with different values of magnetic anisotropy constant K_{eff} (with hysteresis).

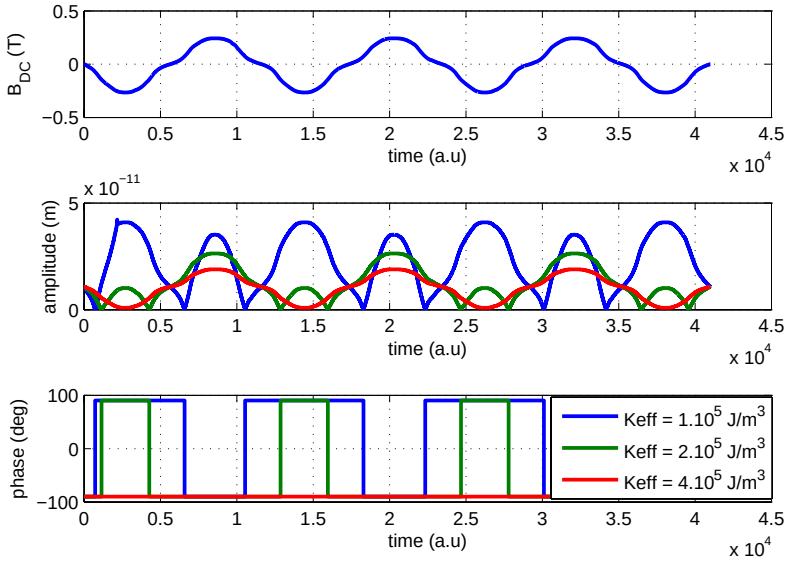

Figure 5.14: Calculated amplitude and phase of oscillation versus time curves with different values of magnetic anisotropy constant K_{eff} (without hysteresis).

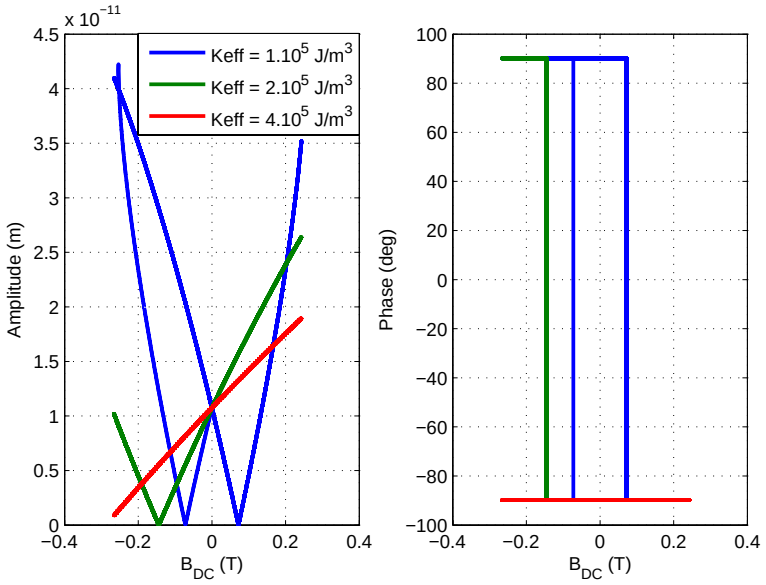

Figure 5.15: Calculated amplitude and phase of oscillation versus B_{DC} field curves with different values of magnetic anisotropy constant K_{eff} (without hysteresis).

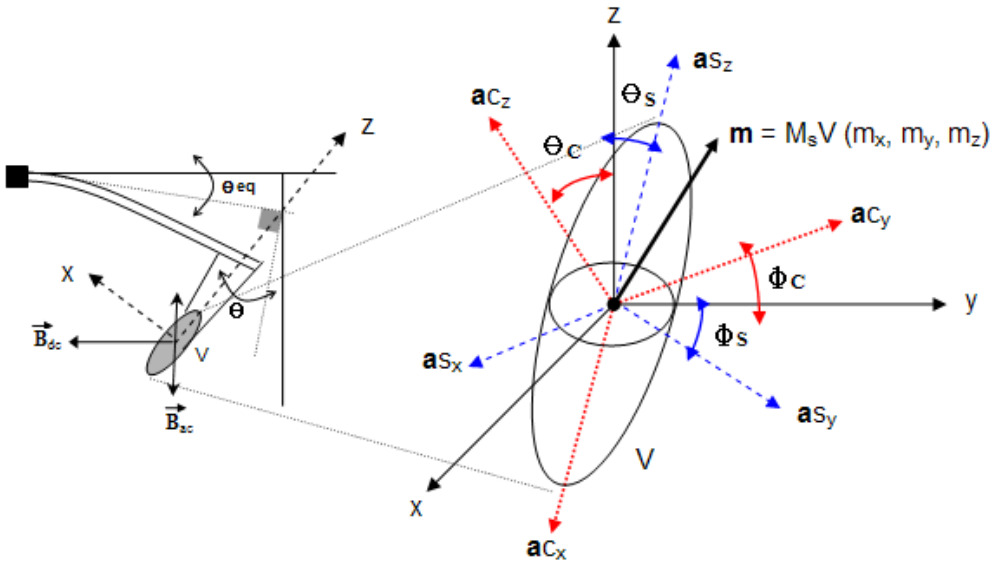

Figure 5.16: General configuration is shown for an arbitrary shape anisotropy axis $\vec{a}s$ and crystalline anisotropy axis $\vec{a}c$ orientations. $\hat{x} - \hat{z}$ plane is the oscillation plane of the cantilever tip in which magnetic fields are applied.

cosines m_x, m_y, m_z in coordinate system $\langle xyz \rangle$ of the cantilever tip as

$$\vec{m} = M_s V(m_x, m_y, m_z) \tag{5.23}$$

where

$$\begin{aligned} m_x &= \sin\theta_m \cos\phi_m \\ m_y &= \sin\theta_m \sin\phi_m \\ m_z &= \cos\theta_m. \end{aligned} \tag{5.24}$$

For the specifications of arbitrary shape and crystalline anisotropy coordinate axises, it is necessary to define two angle parameters θ and ϕ. New coordinate axises can be obtained by rotation of cantilever tip coordinate system $\langle xyz \rangle$ about $\vec{y}$ axis by θ and then about $\vec{z}$ axis by ϕ (Other way around can also be chosen but it defines a different coordinate system). Magneto-crystalline anisotropy axises shown in Fig. 5.16 can be written as

$$\begin{aligned} \vec{a}c_x &= (\cos\theta_C \cos\phi_C, \cos\theta_C \sin\phi_C, -\sin\theta_C) \\ &= (ac_{x1}, ac_{x2}, ac_{x3}) \end{aligned}$$

$$\begin{aligned}
\vec{a}c_y &= (-\sin\phi_C, \cos\phi_C, 0) \\
&= (ac_{y1}, ac_{y2}, ac_{y3}) \\
\vec{a}c_z &= (\sin\theta_C\cos\phi_C, \sin\theta_C\sin\phi_C, \cos\theta_C) \\
&= (ac_{z1}, ac_{z2}, ac_{z3})
\end{aligned} \tag{5.25}$$

and shape anisotropy axises can be written in a similar way as

$$\begin{aligned}
\vec{a}s_x &= (\cos\theta_S\cos\phi_S, \cos\theta_S\sin\phi_S, -\sin\theta_S) \\
&= (as_{x1}, as_{x2}, as_{x3}) \\
\vec{a}s_y &= (-\sin\phi_S, \cos\phi_S, 0) \\
&= (as_{y1}, as_{y2}, as_{y3}) \\
\vec{a}s_z &= (\sin\theta_S\cos\phi_S, \sin\theta_S\sin\phi_S, \cos\theta_S) \\
&= (as_{z1}, as_{z2}, as_{z3}).
\end{aligned} \tag{5.26}$$

By using Eq. 5.23 and Eq. 5.25, direction cosines of the magnetic moment $\vec{m}$ in the coordinate system of crystalline anisotropy can be computed as

$$\begin{aligned}
\alpha 1 &= ac_{x1}m_x + ac_{x2}m_y + ac_{x3} \\
\alpha 2 &= ac_{y1}m_x + ac_{y2}m_y + ac_{y3} \\
\alpha 3 &= ac_{z1}m_x + ac_{z2}m_y + ac_{z3}
\end{aligned} \tag{5.27}$$

and direction cosines of the magnetic moment $\vec{m}$ in the coordinate system of shape anisotropy are

$$\begin{aligned}
\beta 1 &= as_{x1}m_x + as_{x2}m_y + as_{x3} \\
\beta 2 &= as_{y1}m_x + as_{y2}m_y + as_{y3} \\
\beta 3 &= as_{z1}m_x + as_{z2}m_y + as_{z3}.
\end{aligned} \tag{5.28}$$

DC magnetic field $\vec{B}_{DC}$ applied on the plane of oscillation $\hat{x} - \hat{z}$ is written in terms of initial tilt θ_{eq} and deflection angle θ as

$$\vec{B}_{DC} = B_{DC}(\cos(\theta_{eq} + \theta), 0, -\sin(\theta_{eq} + \theta)). \tag{5.29}$$

All the above notations are defined for the purpose of simplifying the total energy expression which is sum of the Zeeman Energy (Eq. 2.25), the shape

anisotropy energy (Eq. 2.20), the cubic magneto-crystalline energy (Eq. 2.11) and the potential energy of deflected cantilever (Eq. 5.5). Total energy of the cantilever-nickel particle system in the magnetic field $\vec{B}_{DC}$ without constant terms is

$$\begin{aligned} U = & -B_{DC}M_sV\left(m_x\cos(\theta_{eq}+\theta)-m_z\sin(\theta_{eq}+\theta)\right) \\ & + \frac{u_oMs^2V}{2}\left(N_a\beta_1^2+N_b\beta_2^2+N_c\beta_3^2\right) \\ & + K_1V\left(\alpha_1^2\alpha_2^2+\alpha_3^2\alpha_2^2+\alpha_3^2\alpha_1^2\right)+K_2V\left(\alpha_1^2\alpha_2^2\alpha_3^2\right) \\ & + \frac{k(L_{eff}\theta)^2}{2}. \end{aligned} \tag{5.30}$$

As can be seen from Eq. 5.30 total energy of the system is characterized by tree parameters which are the deflection angle θ of the cantilever, the elevation angle θ_m and the azimuth ϕ_m angle of magnetization $\vec{m}$. The problem can be reduced to two dimensions using equilibrium condition on the deflection angle θ

$$\frac{\partial U}{\partial\theta} = B_{DC}MsV(m_x\sin(\theta_{eq}+\theta)+m_z\cos(\theta_{eq}+\theta))+kL_{seff}^2\theta = 0. \tag{5.31}$$

Assuming small angle approximation which is the case for the deflection and after making some manipulations, the deflection angle θ can be written as

$$\theta = -\frac{m_x\sin\theta_{eq}+m_z\cos\theta_{eq}}{m_x\cos\theta_{eq}-m_z\sin\theta_{eq}+kL_{seff}^2/(B_{DC}M_sV)}. \tag{5.32}$$

Substituting Eq. 5.32 in total energy equation Eq. 5.30 and then minimizing according to θ and ϕ, equilibrium orientation of the magnetization $\vec{m}$ can be found for various external field conditions. See Appendix A for MATLAB codes.

To convert equilibrium magnetic states into experimentally observed quantities, vertical AC magnetic field $\vec{B}_{AC}$ of form

$$\vec{B}_{AC} = B_{AC}\cos(\Omega t)(\sin(\theta_{eq}+\theta),0,cos(\theta_{eq}+\theta)) \tag{5.33}$$

is applied. Again it is assumed that AC magnetic field of 5-10 Gauss has negligible perturbation on system. The component of AC torque driving the cantilever in $\widehat{x}-\widehat{z}$ plane is

$$\begin{aligned} \vec{\tau}_y &= \left(\vec{m}\times\vec{B}_{AC}\right)_y \\ &= M_sVB_{AC}\cos(\Omega t)\left(m_z\sin(\theta_{eq}+\theta)-m_x\cos(\theta_{eq}+\theta)\right) \end{aligned} \tag{5.34}$$

and kinematically equivalent force (See Eq. 5.16) is

$$\begin{aligned} F_{eq} &= \frac{\tau_y}{L_{deff}} \\ &= M_s V B_{AC} \left(m_z \sin(\theta_{eq}+\theta) - m_x \cos(\theta_{eq}+\theta)\right) cos(\Omega t)/L_{deff}. \end{aligned} \quad (5.35)$$

Effective spring constant of the system in this general model is

$$k_{eff} = \frac{1}{L_{seff}^2}\frac{\partial^2 U}{\partial^2 \theta} = \frac{M_s V B_{DC}}{L_{seff}^2}\left[m_x \cos(\theta_{eq}+\theta) - m_z \sin(\theta_{eq}+\theta)\right] + k. \quad (5.36)$$

After finding driving force F_{eq} and effective spring constant k_{eff} of system, amplitude R and tangent of phase of oscillation $\tan\Phi$ can be computed as

$$R = \frac{M_s V B_{AC} \left|m_z \sin(\theta_{eq}+\theta) - m_x \cos(\theta_{eq}+\theta)\right| w_0^2/(kL_{deff})}{\sqrt{\left(\frac{w_0^2}{k}\frac{B_{DC}M_s V[m_x\cos(\theta_{eq}+\theta)-m_z\sin(\theta_{eq}+\theta)]}{L_{seff}^2} + w_0^2 - \Omega^2\right)^2 + \frac{w_0^2\Omega^2}{Q^2}}} \quad (5.37)$$

$$\tan(\Phi - \epsilon\,\pi) = \frac{w_0\Omega}{Q\left(w^2 - \Omega_0^2 - \frac{w_0^2}{k}\frac{B_{DC}M_s V[m_x\cos(\theta_{eq}+\theta)-m_z\sin(\theta_{eq}+\theta)]}{L_{seff}^2}\right)} \quad (5.38)$$

where $\epsilon = 1$ if $[m_z \sin(\theta_{eq}+\theta) - m_x \cos(\theta_{eq}+\theta)] < 0$, otherwise $\epsilon = 0$. Direction cosines m_x, m_y, m_z of the magnetic moment $\vec{m}$ are obtained minimizing the total energy of the ssytem Eq. 5.30 for a given magnetic field $\vec{B}_{DC}$.

Simulations for general model were made for the experimentally applied DC magnetic field $\vec{B}_{DC}$ shown in Fig. 5.7. Simulation parameters used are listed in table Tab. 5.2. Surface of total energy at DC magnetic field $\vec{B}_{Dc}$ of 400 Gauss can be seen in Fig. 5.17. Trace which total magnetic moment $\vec{m}$ of particle follows under varying DC magnetic field $\vec{B}_{Dc}$ is shown in Fig. 5.18. Also amplitude R response of cantilever-magnetic particle system is shown in Fig. 5.19. Another result of the simulations showing dependance on initial states is seen in Fig. 5.20 and Fig. 5.21. The parameters different from the ones listed in Tab. 5.2 for this simulation are $\theta_C = 0^o$, $\phi_C = 0^o$, $K1 = -5 * 10^3$, $V = 9 * 10^{-20}$ and $Keff = 10^5$.

M_s	$0.52 \cdot 10^6$	Am^2
V	$6 \cdot 10^{-20}$	m^3
K_{eff}	$7.7 \cdot 10^4$	$\mathrm{J/m}^3$
$K1$	$-5 \cdot 10^4$	$\mathrm{J/m}^3$
$K2$	0	$\mathrm{J/m}^3$
θ_S	0	deg
ϕ_S	0	deg
θ_C	40	deg
ϕ_C	170	deg
k	0.2	N/m
Q	92.6	-
L	$475 \cdot 10^{-6}$	m
L_{eff}	$3.1 \cdot 10^-4$	m
L_{deff}	$9.9 \cdot 10^-5$	m
θ_{eq}	11^o	deg
B_{DC}	± 0.225	T
B_{AC}	± 0.5	mT

Table 5.2: Parameter values used in the cantilever magnetometry simulations for the general model.

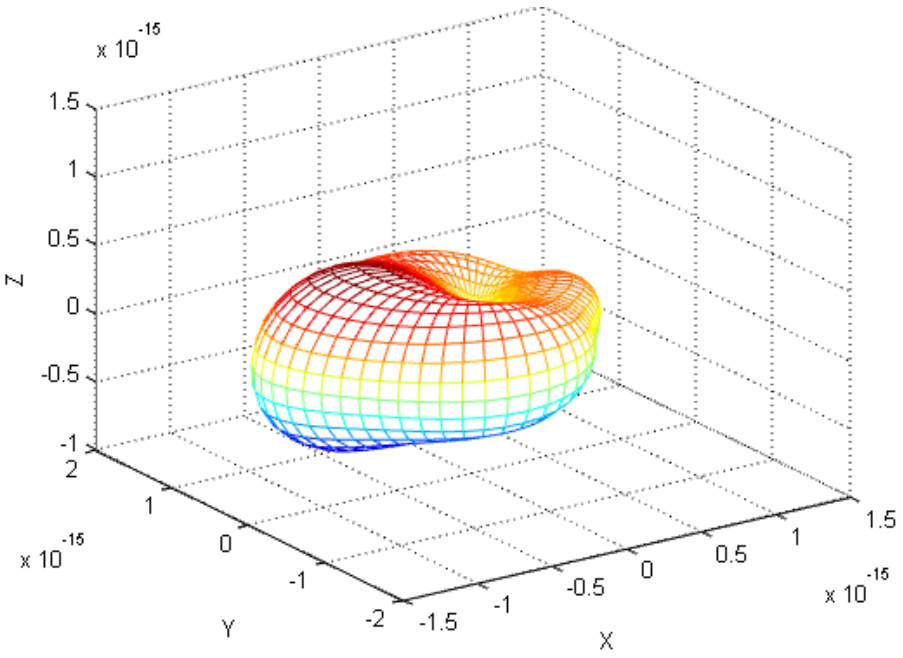

Figure 5.17: Calculated total energy surface at 400 Gauss is shown (calculated with parameters listed in Tab. 5.2).

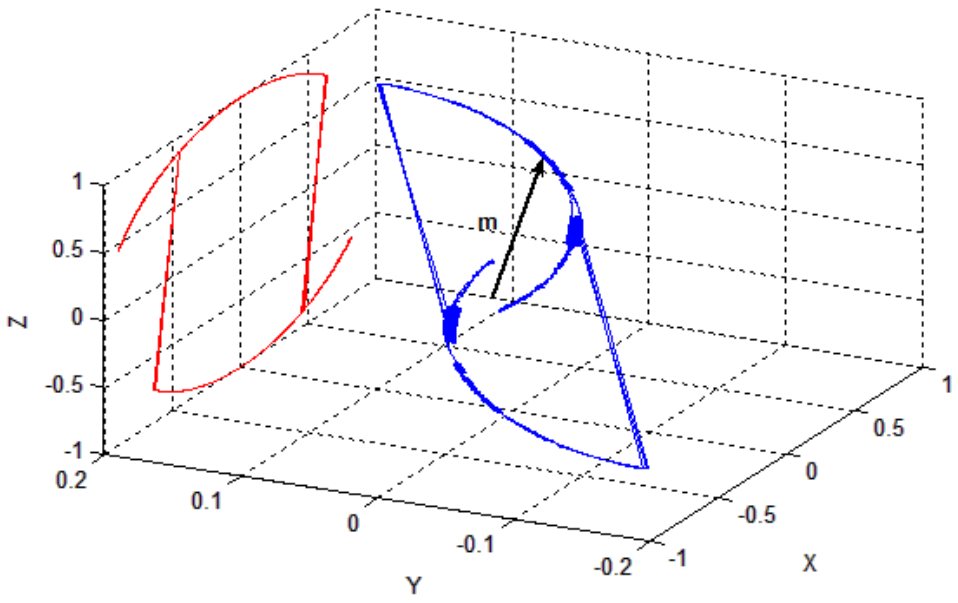

Figure 5.18: (Blue curve)Calculated trace of the total magnetic moment $\vec{m}$ of particle in 3D under varying DC magnetic field $\vec{B}_{DC}$. (Red curve)Projection of trace on $\hat{x} - \hat{z}$ plane is also shown.

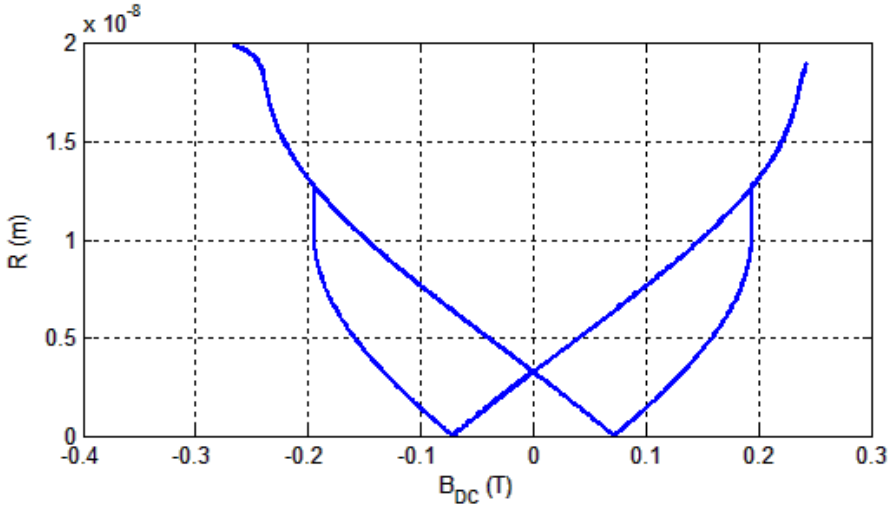

Figure 5.19: Calculated amplitude response of cantilever-magnetic particle system under varying magnetic fields in general model. Results show similarity in some respect to the results of the simplified model.

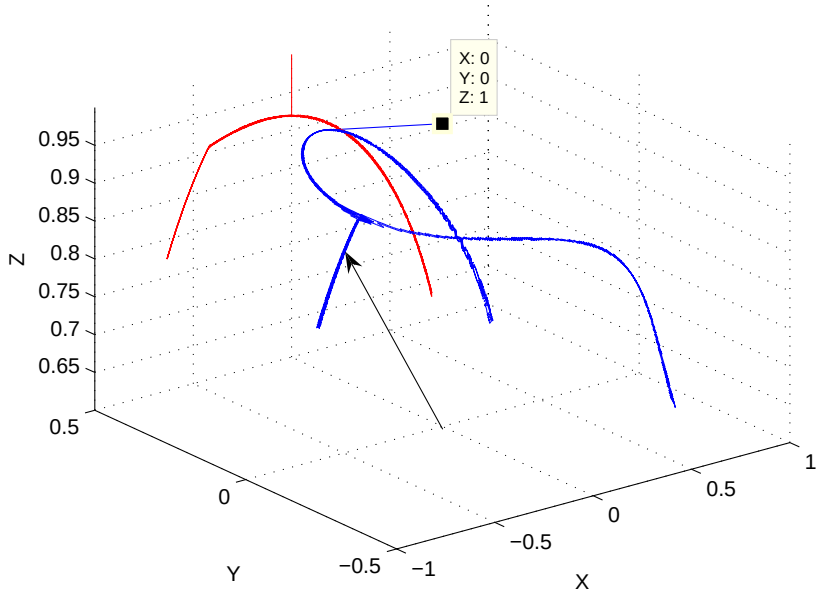

Figure 5.20: Calculated evolution of magnetic moment $\vec{m}$ with initial conditions $\phi_m = 0^o$ and $\theta_m = 0^o$. Red curve is the projection of evolution trace on $\hat{x} - \hat{z}$ plane.

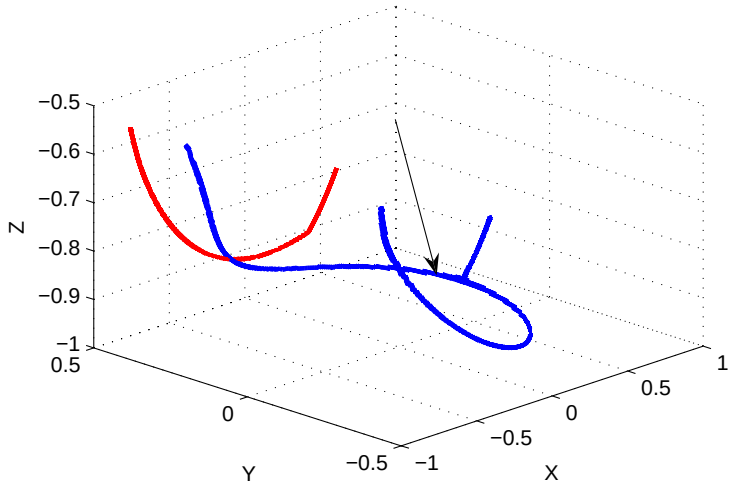

Figure 5.21: Calculated evolution of magnetic moment $\vec{m}$ with initial conditions $\phi_m = 90^o$ and $\theta_m = 90^o$. Red curve is the projection of evolution trace on $\hat{x} - \hat{z}$ plane.

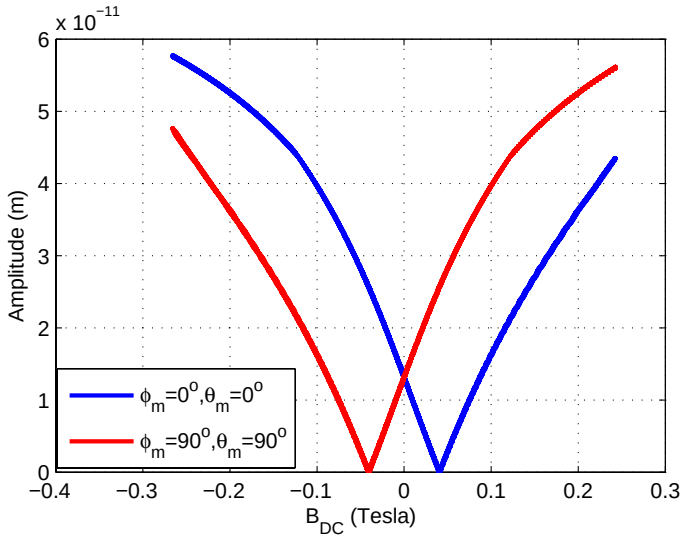

Figure 5.22: Mirror symmetric amplitude response of cantilever-magnetic particle system can occur with different initial conditions chosen for same simulation parameters.

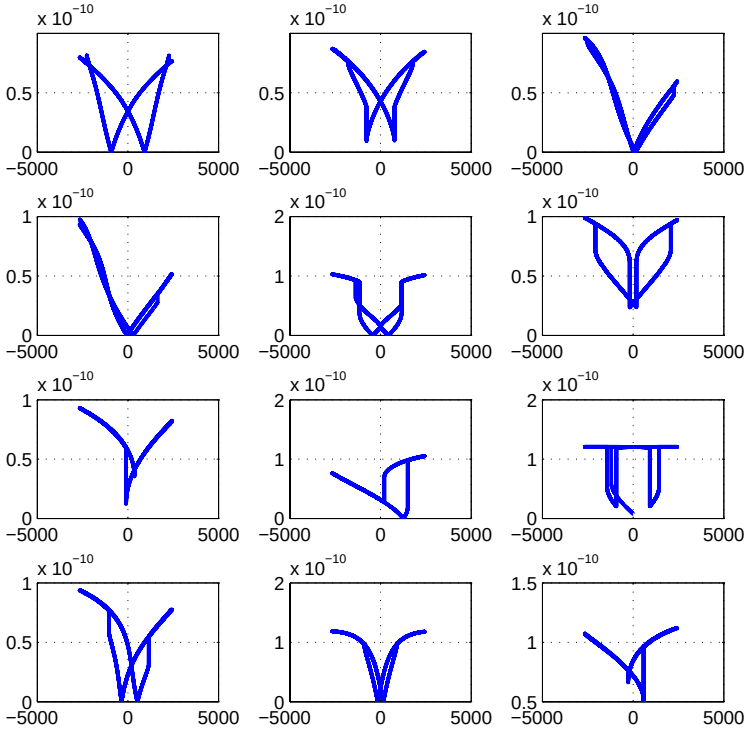

Figure 5.23: Various amplitude (m) vs. B field (Gauss) responses are given for some simulation parameters.

5.2.2 Fluxgate Measurement Configuration

The fluxgate measurement configuration is same as the characterization configuration except there is only vertical AC magnetic field $\vec{B}_{AC}$ applied as shown in Fig. 5.24. $\vec{B}_{AC}$ is sum of sinusoidal magnetic field of 0.15 T at 1kHz and driving AC magnetic field of 0.5 mT at 2nd resonance frequency of the cantilever. It is assumed that local field of sample is in the direction of $\vec{B}_{AC}$. Local magnetic field values of +0.01 T and −0.01 T were superimposed on the magnetic field $\vec{B}_{AC}$. Simulations were made with the simplified model ($K_{eff} = 5.10^4 J/m^3$). Results can be seen in Fig. 5.25.

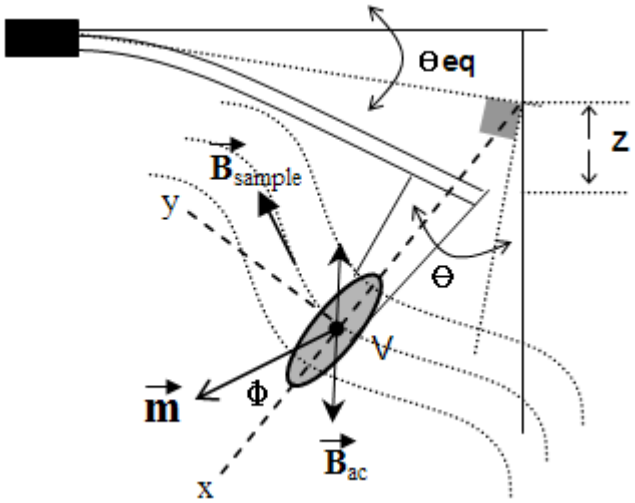

Figure 5.24: Fluxgate measurement configuration in a local magnetic field $\vec{B}_{\text{sample}}$ of a sample is shown.

As can bee seen from the results shown in Fig. 5.25 magnetic particle flips its magnetic moment $\vec{m}$ two times in one period of the sinusoidal magnetic field at 1kHz corresponding to two sudden change of phase of 180^o in the phase signal. Presence of the local magnetic field B_{sample} shifts the timing of these phase alternations, thus an asymetry in phase signal occurs (change of duty cyle in this case) as in fluxgate magnetometry. Local field of the sample B_{sample} can be deduced from the even harmonics of the phase signal (see Fig. 5.26).

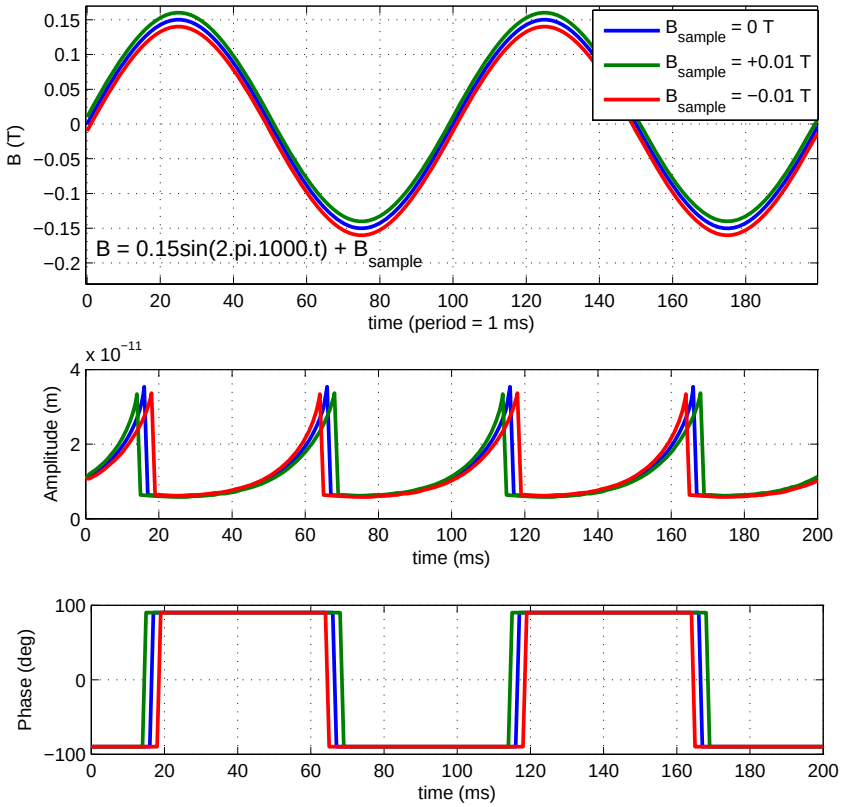

Figure 5.25: Fluxgate measurement simulation result is shown. Presence of external field results in asimetry in amplitude and phase responses.

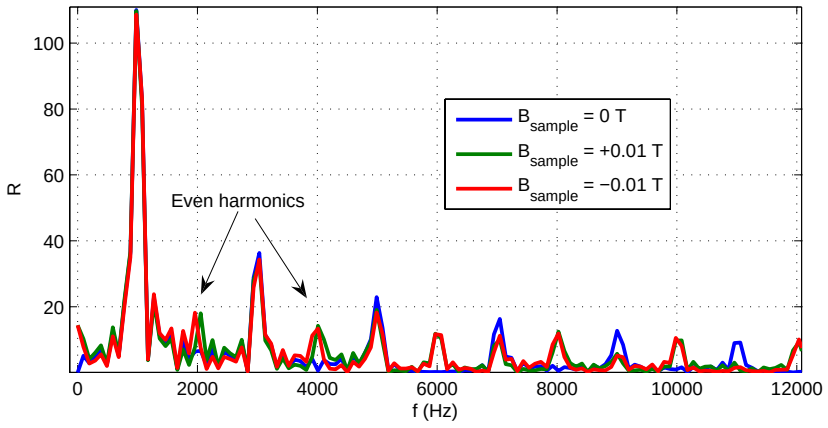

Figure 5.26: FFT of the phase of 2$^{\text{nd}}$ resonance signal shows creation of even harmonics at the presence of local magnetic field B_{sample}.

Chapter 6

Results

This chapter explains the fabrication process of MFM tips having submicron nickel particles attached using standard Focused Ion Beam (FIB) techniques, measurement of their magnetic responses in a DC magnetic field $\vec{B}_{DC}$ and multifrequency fluxgate magnetic imaging results with these FIB tailored magnetic tips.

6.1 Fabrication of MFM Tips by FIB

Three MFM tips were fabricated and used in this thesis. They are named as 1^{st}, 2^{nd}, and 3^{rd} MFM tips. Sections of nickel thin films were attached on the apex of commercial cantilever tips by standard FIB techniques used in sample preparation for Transmision Electron Microscopy (TEM). FIB system (FEI Nova Lab 600) used in these processes is shown in Fig. 6.1. Steps of fabrication process are

1. *Growth of nickel thin films :* Nickel thin films of desired thickness (330 nm and 156 nm) were built by evaporation on the substrates of silicon wafer ($< 100 >$) and Si_3N_4 in high vacuum conditions ($10^{-6}torr$). Chemical spectroscopy and compositional mapping of the evaporated film was

Figure 6.1: FIB system used in the processes.

made with Energy Dispersive X-ray Analysis system (EDAX). EDAX results are shown in Fig. 6.2. TEM image of as-prepared nickel film reveals polycrystalline structure of the coating (see in Fig. 6.3).

2. *Release cutting :* After a deposition of protective layer of platin Pt on target section of the nickel film, two trenches are cut out by Ga^+ ion milling. Then U shape undercutting is made at a glazing angle through trenches to make the target section suspended at one side (see Fig. 6.4-c,d and Fig. 6.6-e).

3. *Attachment of the probe tip on the target section of nickel film:* After release cutting of target section, a micro probe (OmniProbe) is manually manipulated towards target section and tip of the probe is welded with Pt deposition to the free end of target section (see Fig.6.7-a). Holding part of the target section is no longer necessary so it is cut to seperate the suspending target section from the substrate completely.

4. *Attachment of the target section of Ni film on the apex of cantilever tip :* After removal of target section via manipulator probe from the surface, it is placed at an appropriate angle (90^o) on the apex of cantilever tip and welded again with Pt deposition at the contact side (see Fig. 6.4-e,f and Fig. 6.7-b). Required part of the target section is then severed with Ga^+

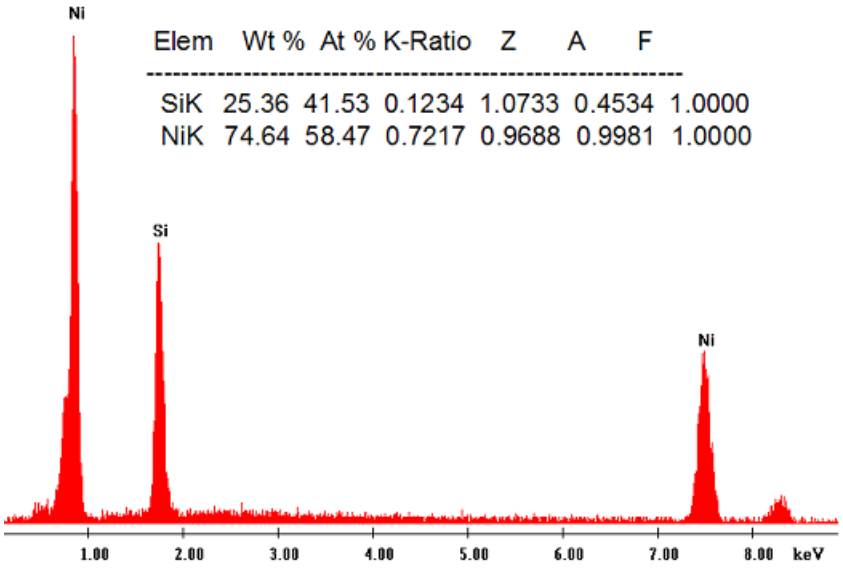

Figure 6.2: Results of Energy Dispersive X-ray Analysis of the nickel film evaporated on silicon crystal. Contributions from silicon substrate and nickel film are clearly seen.

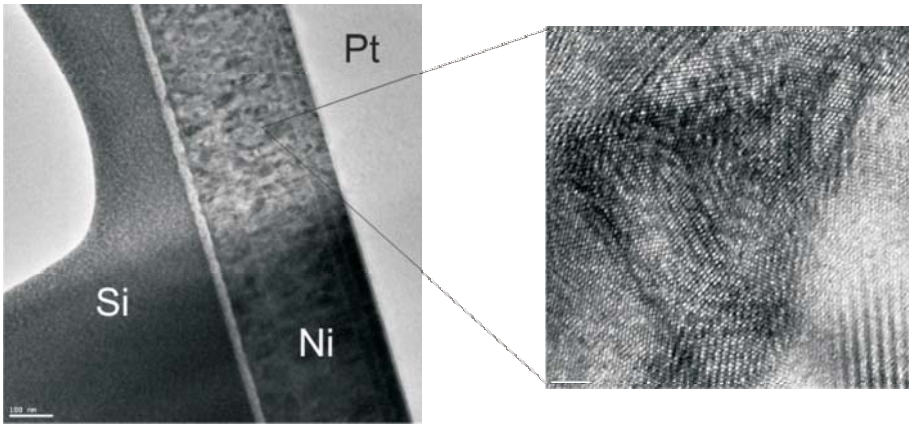

Figure 6.3: Results of TEM imaging of the nickel thin film on silicon wafer: Polycrystalline structure of the nickel coating can be seen.

ion milling to separate it from manipulator probe tip (see Fig. 6.7-c and Fig. 6.5-a).

5. *Final modification :* The last step of the process is to further modify the target section attached on the cantilever tip at front and lateral sides so a section of nickel film of desired geometry is obtained (see Fig. 6.5-c,d,e,f and Fig. 6.8-e,f).

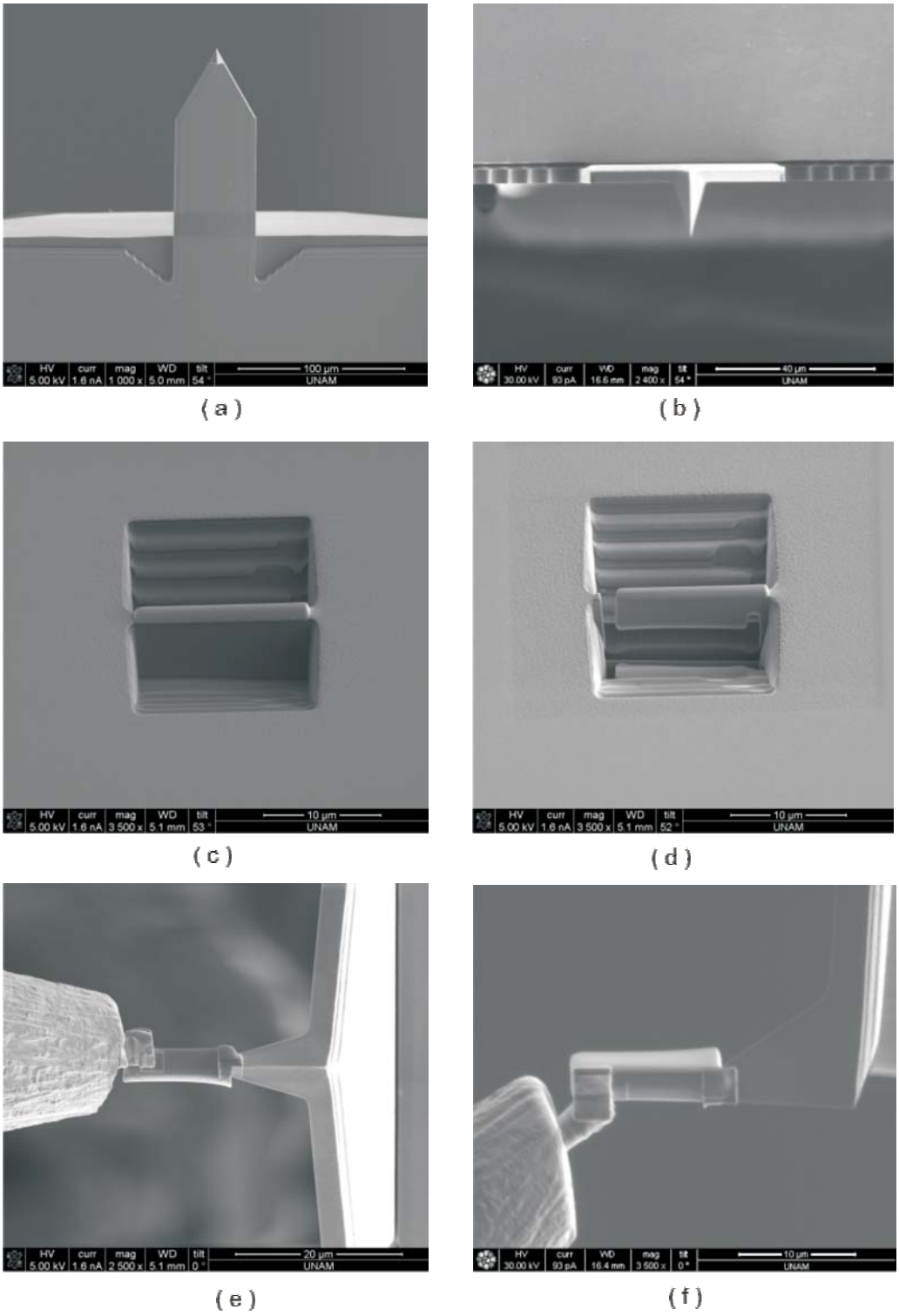

Figure 6.4: Fabrication process of 1st tip: (a) Front view of commercial cantilever to be modifed. (b) Top view. (c) 1st cutting phase of nickel film coating. (d) 2nd phase, i.e. release cutting. (e) Manipulation and attachment of the target section on the cantilever tip. (f) A different perspective of the attachment.

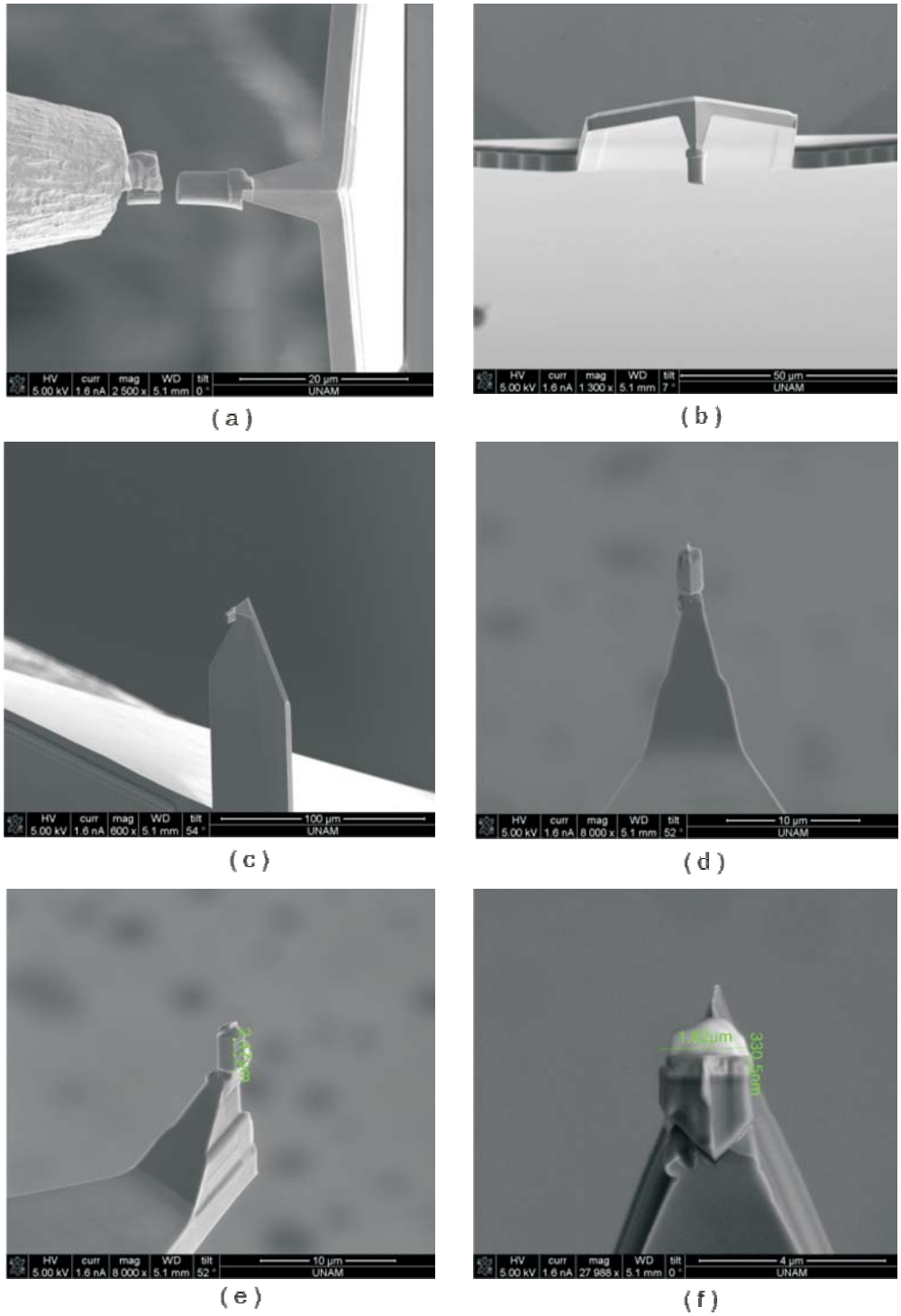

Figure 6.5: Fabrication process of 1st tip (Continued...): (a) Removal of the manipulator probe from the target section and the cantilever tip. (b) Top view. (c) A perspective view of the attachment. (d) Modification of the attached section resulting in a sharper cap for improvement of resolution. (e) A different view of the attachment on the tip. (f) Backscattered Electron Detector (BSED) bottom view of attached and modified section is showing more compositional contrast which marks the light grey Ni film in the middle of white Pt protective layer and dark grey Si substrate.

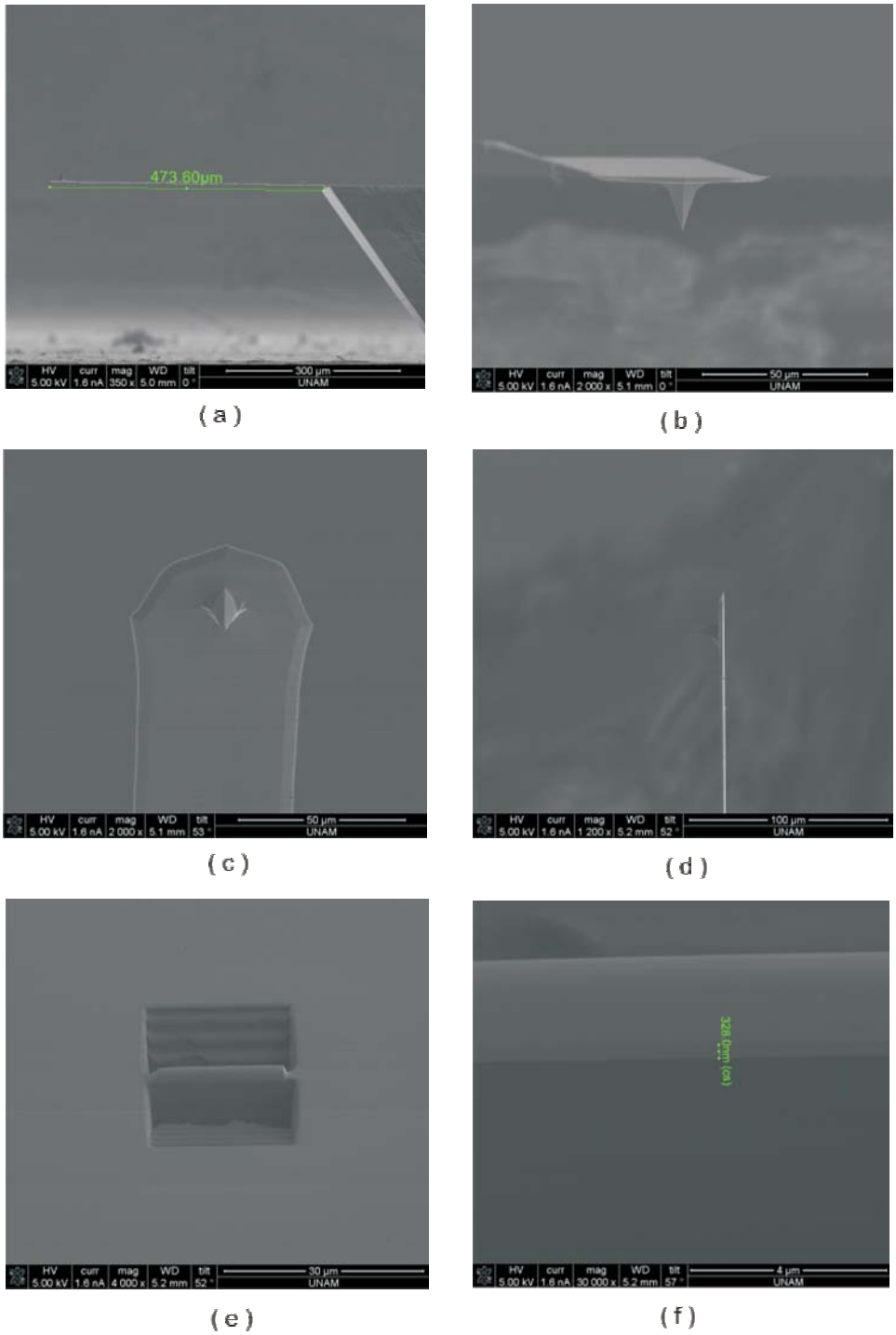

Figure 6.6: Fabrication process of 2nd tip:(a) Front view of commercial cantilever to be modifed. (b) Head view. (c) Front view. (d) Side view. (e) Cutting out trenches at both side of target section.(f) BSED image showing compositional contrast of the nickel film sandwiched between Pt layer of protection and Si substrate.

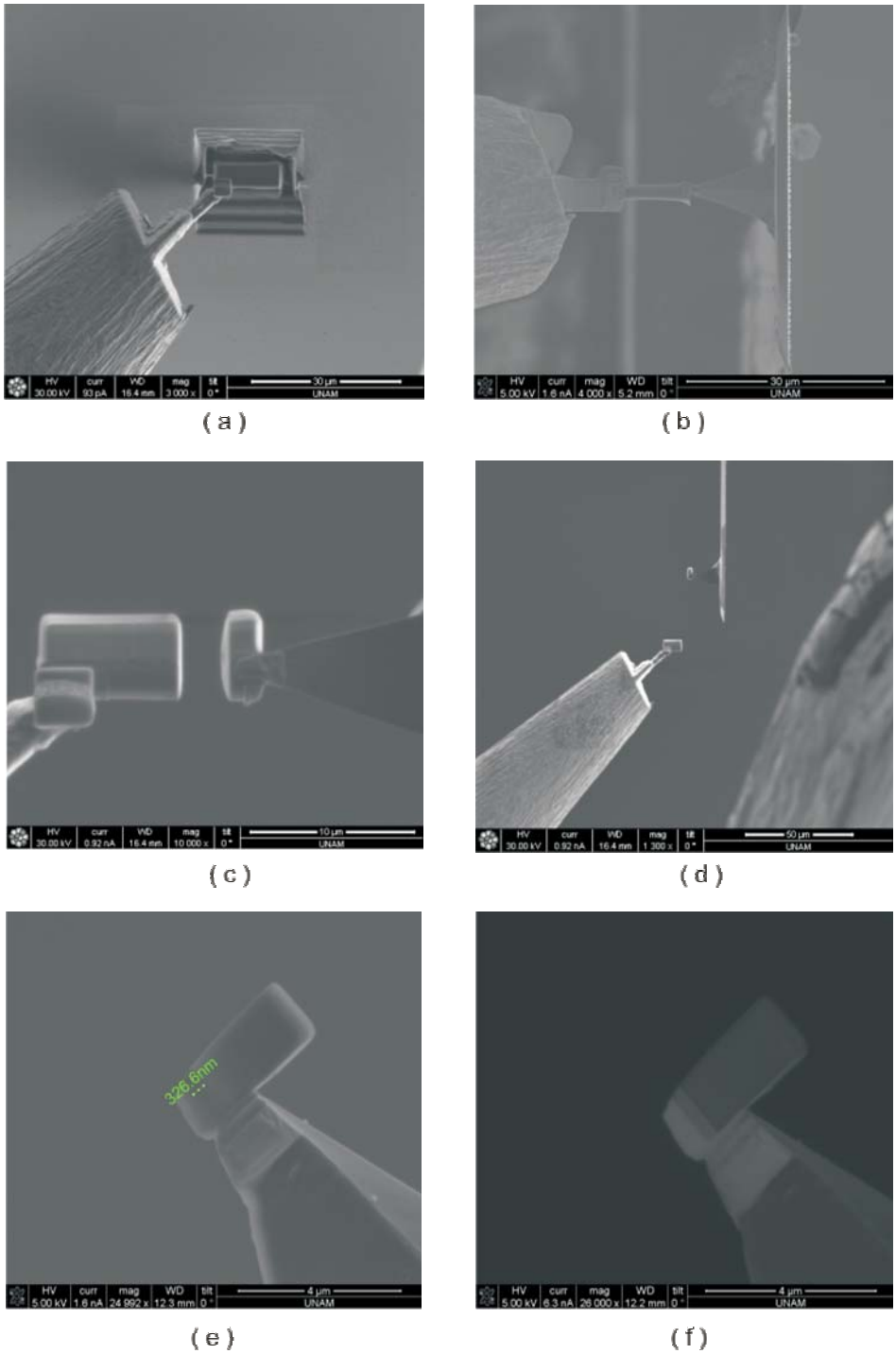

Figure 6.7: Fabrication process of 2nd tip (Continued...): (a) Attachment of manipulator probe via Pt deposition on the suspended target section. (b) Alignment and attachment of magnetic target section on cantilever tip. (c) Seperation of manipulator probe from target section and cantilever tip. (d) Removal of manipulator probe. (e) Side view of attached section showing nickel sandwiched between Pt layer of protection and Si substrate. (f) BSED image showing compositional contrast.

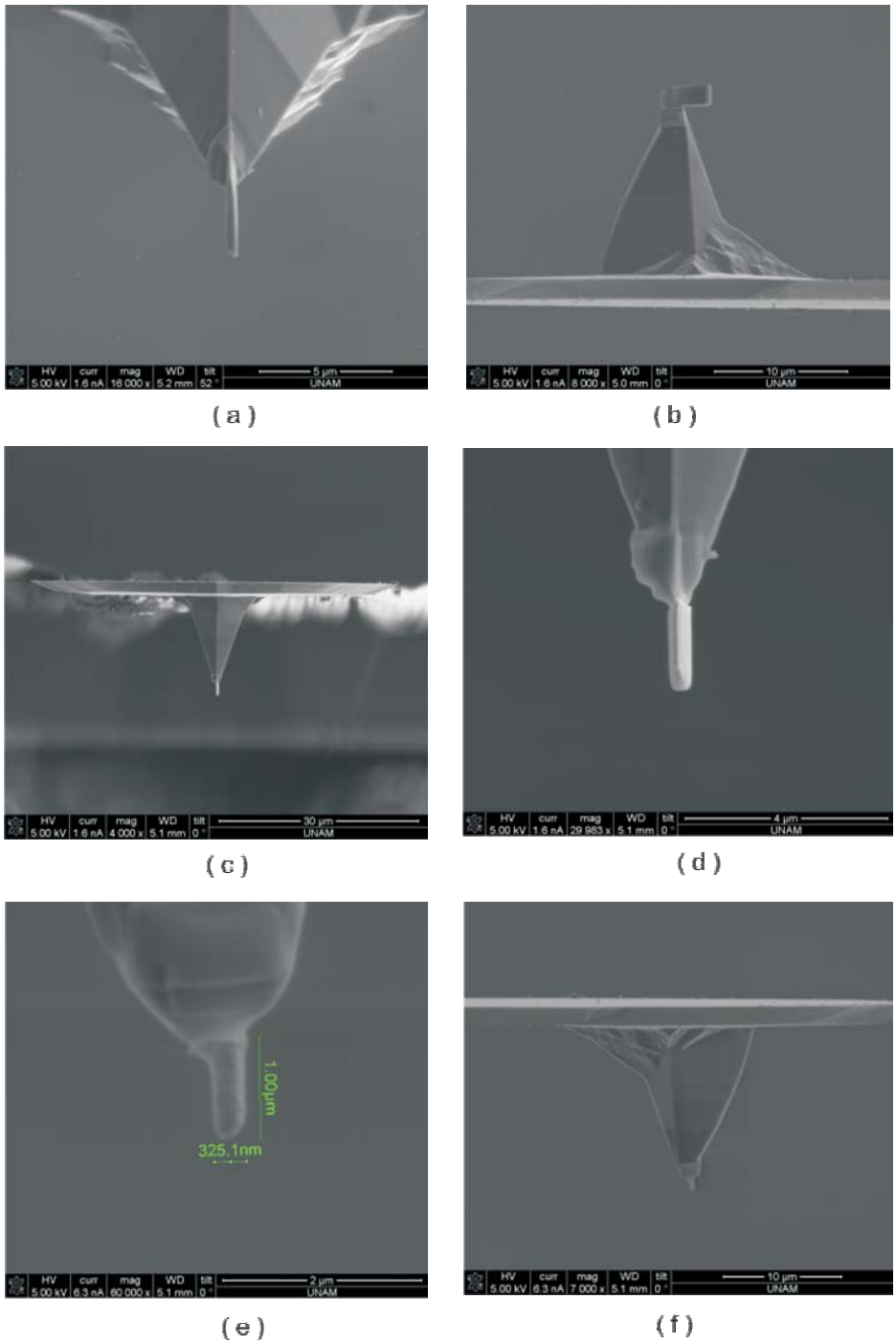

Figure 6.8: Fabrication of 2nd tip (Continued...)(a) Front view of trimmed section with focused ion beams. (b) Side view. (c) Top view. (d) Close view. (e) View of final modification of attached section resulting only nickel column. (f) Side view of alignment between the nickel column and the cantilever plane.

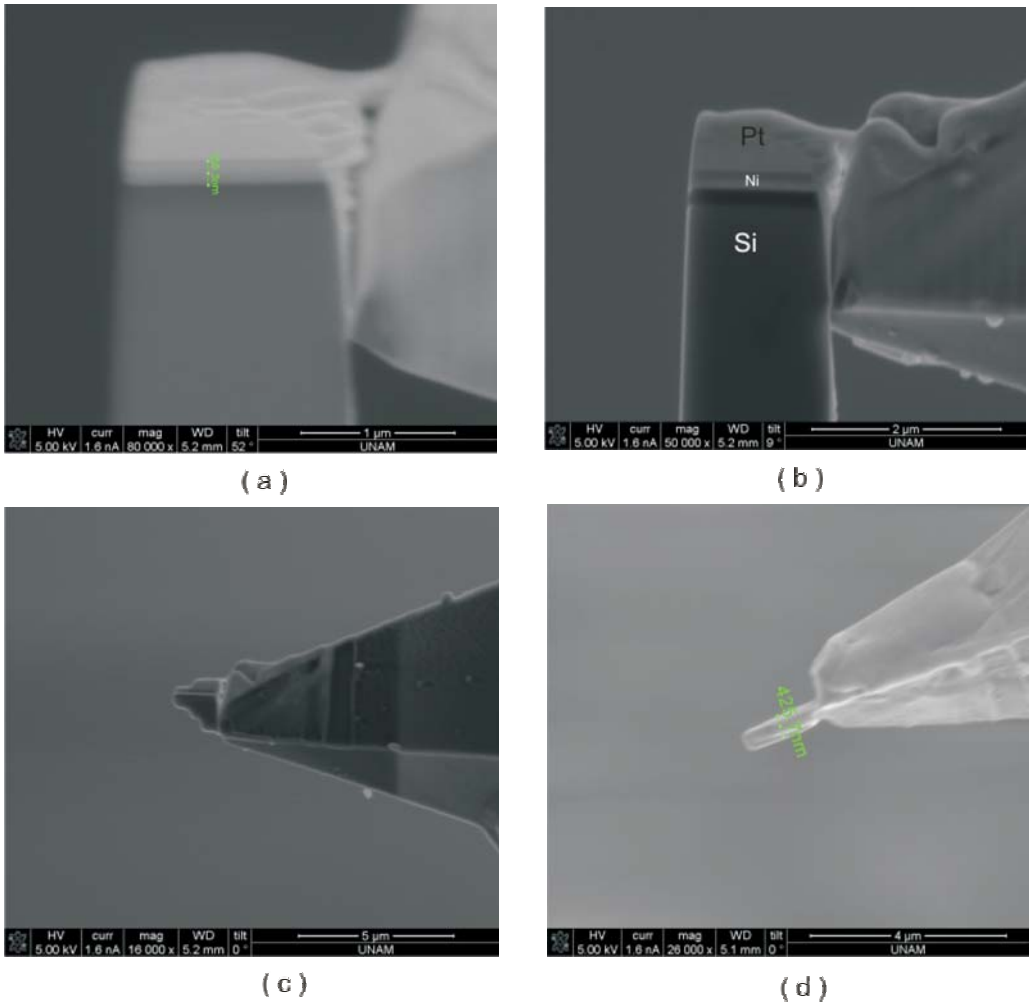

Figure 6.9: Fabrication of the 3rd tip : (a) BSED image showing compositional contrast. (b) Nickel film is seen between Pt layer of protection and silicon nitrate/silicon (c) Side view. (d) Front view.

6.2 Characterization of FIB Tailored Tips

AFM system used for cantilever magnetometry and fluxgate measurements can be seen in Fig. 6.10 and cantilever magnetometry configuration is displayed schematically in Fig. 6.11

Figure 6.10: MFP-3D AFM system shown in the figure was used for fluxgate measurements and cantilever magnetometry [53].

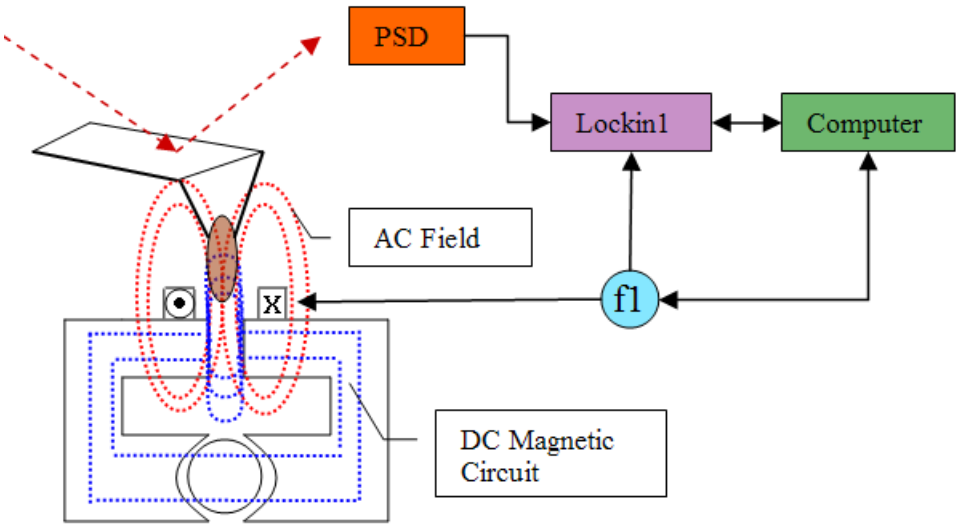

Figure 6.11: Cantilever magnetometry configuration used for magnetic characterization of FIB tailored MFM tips.

For signal acquisition a phase sensitive detector, i.e lock-in amplifier (Stanford Reseach Systems, SR844) was used with a function generator (Stanford Reseach

Systems, DS345) having 1μ Hz sensitivity as a reference source. The coil used for the generation of AC field was drived by function out of the function generator. External DC field (Sensored Variable Field Module-VFM [32]) was controlled via commercial software of the AFM system. In order to control all devices and to automize experiments such as frequency scans, a custom software was developed with Microsoft Visual Studio C#.net. This software uses GPIB interface for digital comunication with devices and also communicates with the commercial software of the AFM system (via *Automation Server-Client* property) to acquire the strength of DC magnetic field (applied by VFM).

For the mechanical calibration of MFM tips routine operations of commercial software of the system were used. First of all, sensitivity parameter, i.e. AmpInvols (Amplitude Inverse Voltage) giving deflection in nm corresponding to an equivalent voltage signal was found measuring deflection versus tip-sample separation which is given by very sensitive LVDT (Linear Variable Differential Transformer). Results can be seen in corresponding figures. Then thermal spectrums of cantilevers were obtained and used for spring constant k determination which was given as a result of equipartition theorem. At the same time resonance frequencies f_n of modes can be measured. After fine tuning operations done by the software, i.e. fitting as if each mode was a damped simple harmonic oscillator spring constants k and quality factors Q of cantilevers were obtained. Results can be seen in tables Tab. 6.1, Tab. 6.2 and Tab. 6.3.

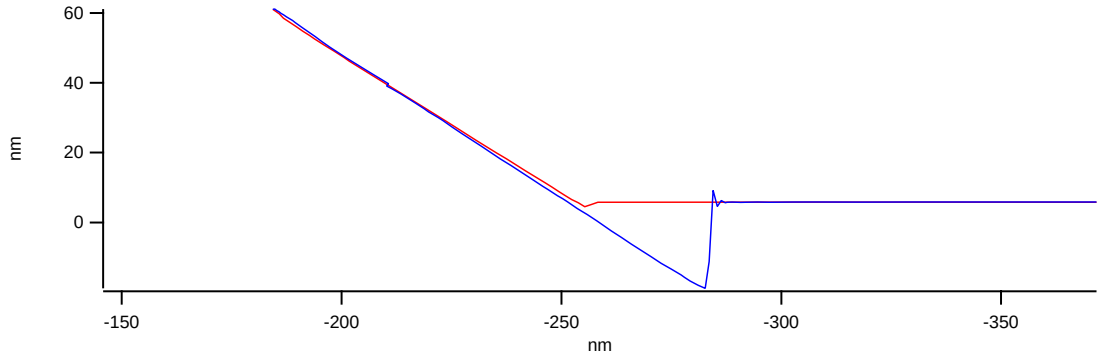

Figure 6.12: Deflection versus tip-samle separation plot is used for calculation of the sensitivity parameter, i.e. *AmpInvols*(132.09 nm/V).

f_1	157.603	kHz
k_1	5.88	N/m
Q_1	225.5	-
f_2	891.2	kHz
k_2	121.17	N/m
Q_2	352	-
L	$160 \cdot 10^{-6}$	m
AmpInvols	132.09	nm/V
t_{coating}	330	nm
w_{coating}	1.2	μm
l_{coating}	3.15	μm
Substrate	Si $<100>$	-

Table 6.1: Properties of the cantilever and the section of nickel film attached on the 1st tip are listed.

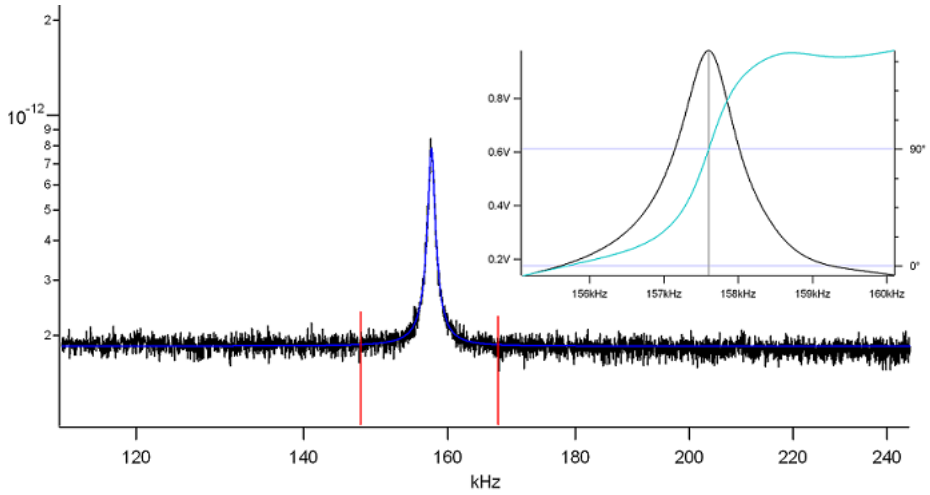

Figure 6.13: Thermal spectrum of 1st FIB tailored MFM tip. Inlet shows details of fine tuning.

The 1st tip to be magnetically characterized can be seen in Fig. 6.4 and Fig. 6.5. Properites of the 1st tip and the nickel film section attached are given in Tab. 6.1. As prepared for multifrequency MFM 1st tip had a very high and stiff 2nd resonance mode ($f_2 > 900$ kHz). Therefore FIB operations reducing thickness were conducted after first measurements of cantilever magnetometry which can be seen in Fig. 6.14 and Fig. 6.15. As it is observed resonance frequency of cantilever is same and there is no considerable Q factor change since it is related with the slope of phase curves on the resonance frequency. But an interesting shifts of phase curves in vertical direction can be seen. Cantilever magnetometry data taken after thickness modification of the 1st tip can be seen in Fig. 6.16 and Fig. 6.17.

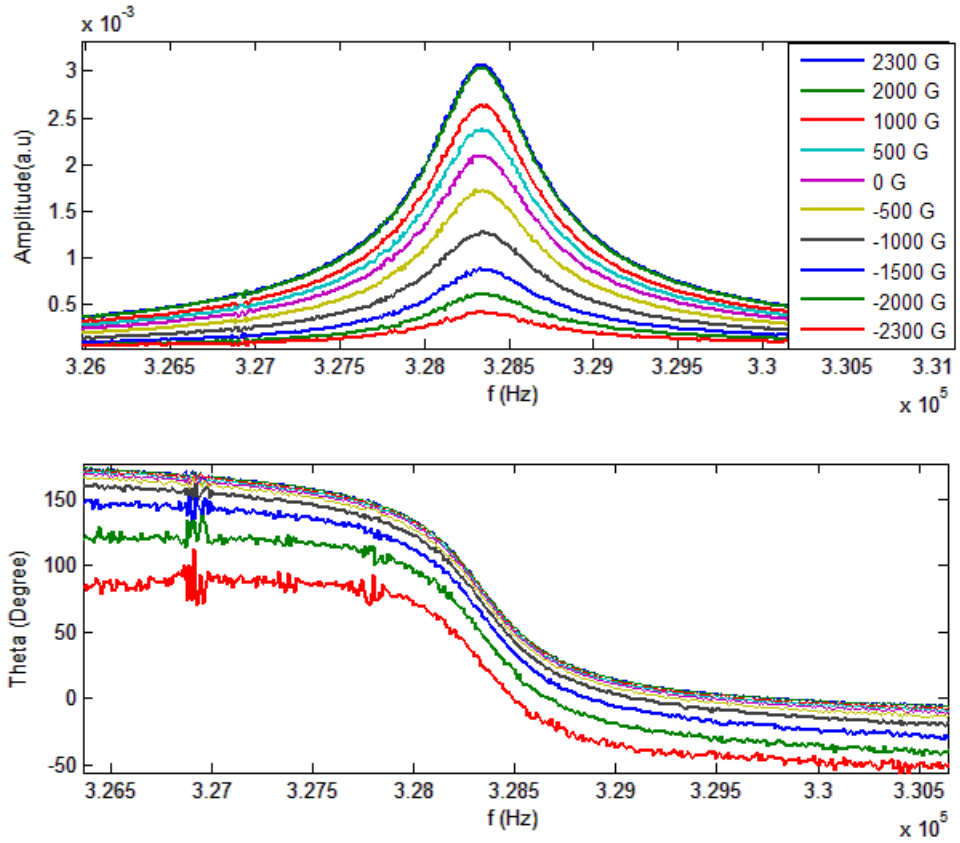

Figure 6.14: Amplitude, phase versus frequency scans of 1st tip were conducted at different DC field values.

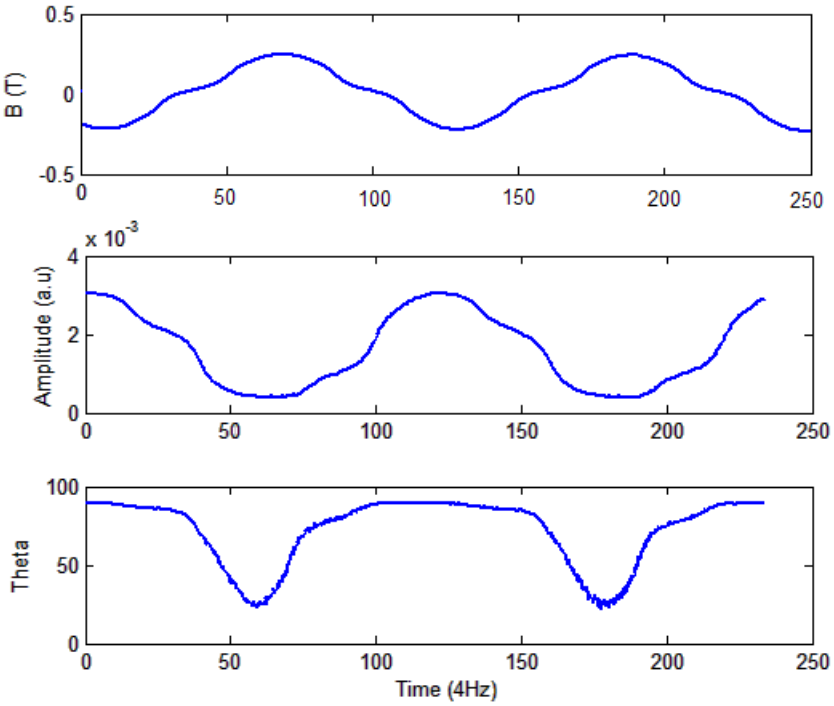

Figure 6.15: Amplitude and phase signals of 1st tip at first resonant frequency of the cantilever under quasi-sinusoidal temporal variation of field (Sampling frequency is 4Hz).

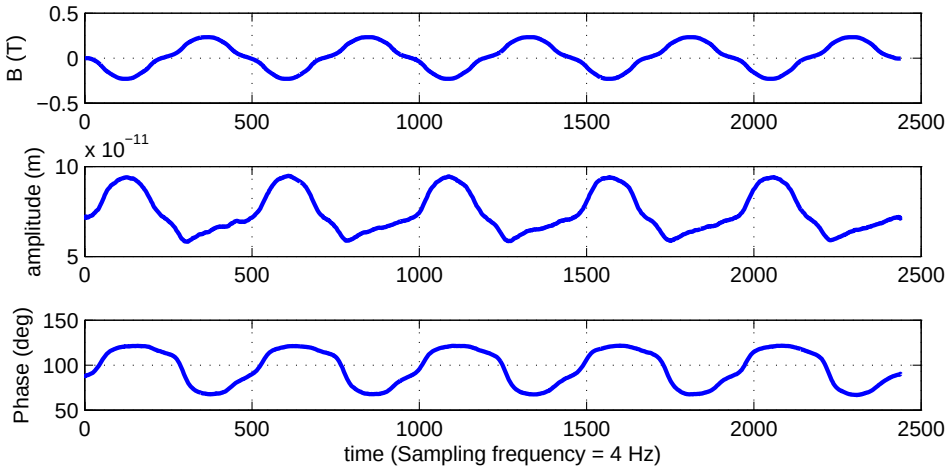

Figure 6.16: Applied field B, amplitude and phase versus time graphs for the 1st FIB tailored tip.

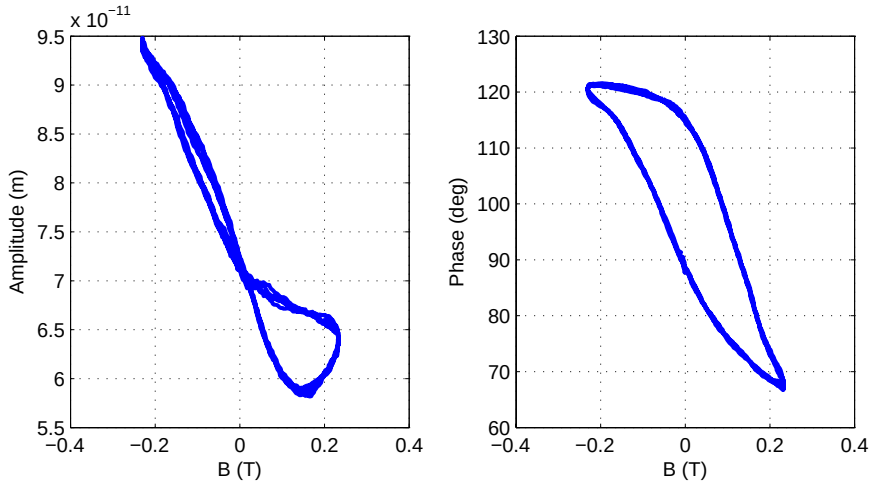

Figure 6.17: Amplitude and phase versus B magnetic field graphs for the 1st FIB tailored tip.

Properties of 2nd FIB tailored tip are listed at Tab. 6.2. Thermal graph showing first four resonance modes is seen in Fig. 6.18. Cantilever magnetometry data for the first resonant mode can be seen in Fig. 6.19 and Fig. 6.20.

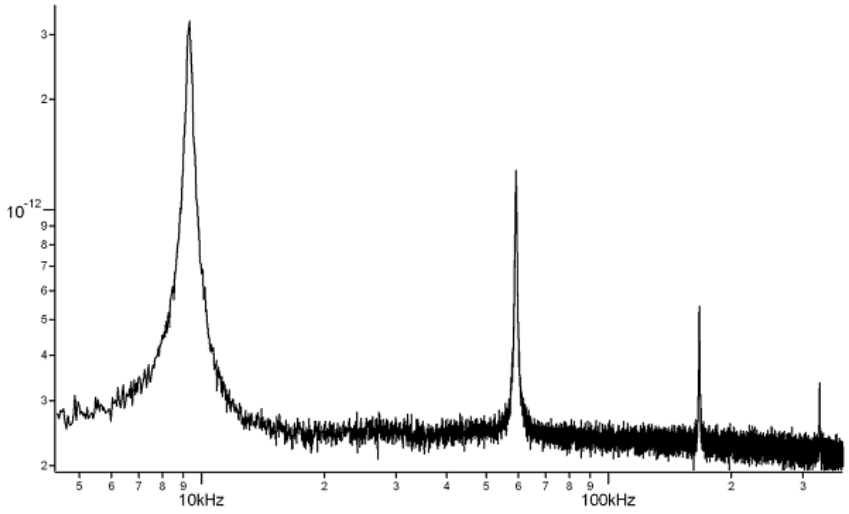

Figure 6.18: Thermal spectrum of 2nd FIB tailored MFM tip showing the first 4 mechanical modes.

f_1	9.337	kHz
f_2	59.396	kHz
k_2	0.2	N/m
Q_2	96.2	-
f_3	167.341	kHz
k_3	0.6	N/m
Q_3	225.5	-
L	$473.6 \cdot 10^{-6}$	m
AmpInvols	602	nm/V
t_{coating}	330	nm
w_{coating}	330	nm
l_{coating}	1	μm
Substrate	Si $<100>$	-

Table 6.2: Properties of cantilever and section of nickel coating attached on the 2nd tip are listed.

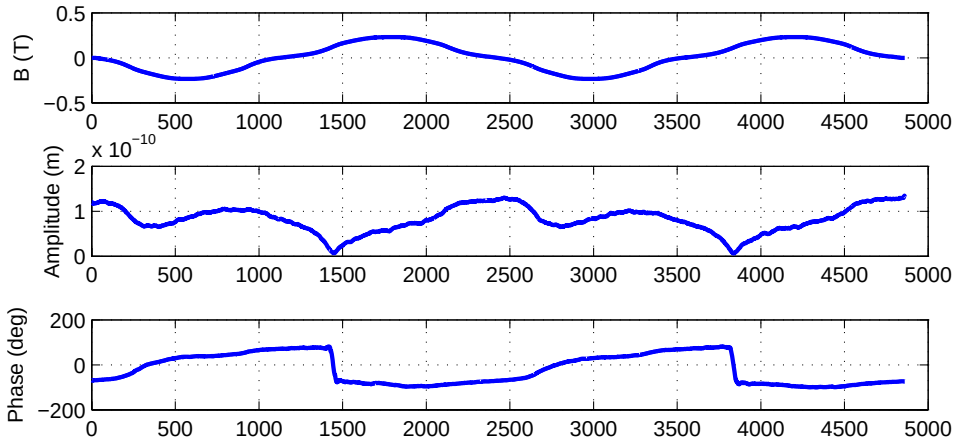

Figure 6.19: Applied field B, amplitude and phase versus time graphs for the 2nd FIB tailored tip.

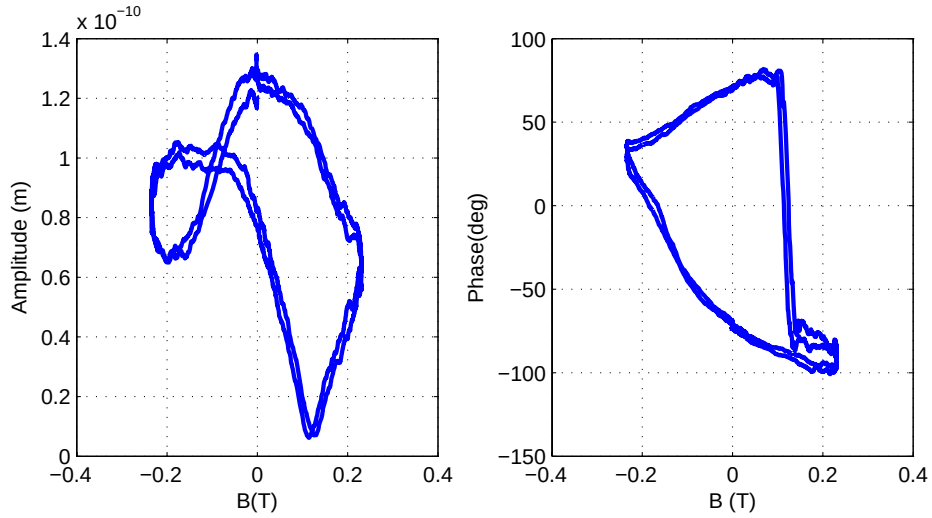

Figure 6.20: Amplitude and phase versus B magnetic field graphs for the first resonance mode of 2nd FIB tailored tip.

Properties of 3rd FIB tailored tip are listed at Tab. 6.3. Thermal graph showing first four resonance modes and graph of deflection vs. tip-sample seperation are seen in Fig. 6.22 and Fig. 6.21, respectively. Cantilever magnetometry data for the first and second resonant mode can be seen in Fig. 6.23 and Fig. 6.24, respectively.

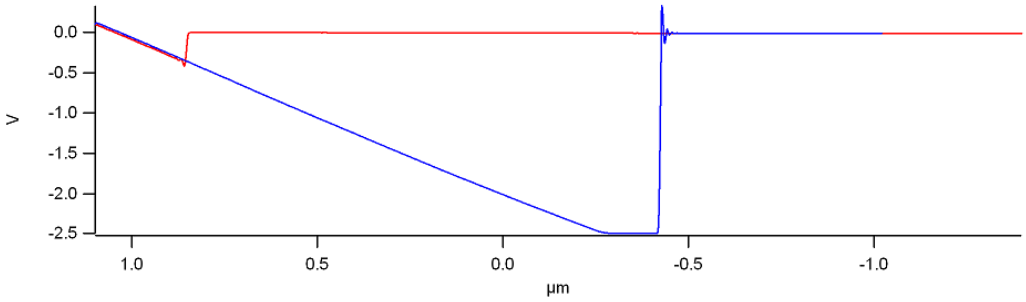

Figure 6.21: Deflection versus tip-samle separation plot is used for calculation of the sensitivity parameter, i.e. *AmpInvols*(602 nm/V).

A good agreement between experimental cantilever magnetometry data and results of simulations can not be obtained especially in phase responses. At first the eddy currents were considered to be the possible reason because back side of the cantilevers were fully coated with Al to increase their reflectance. But it

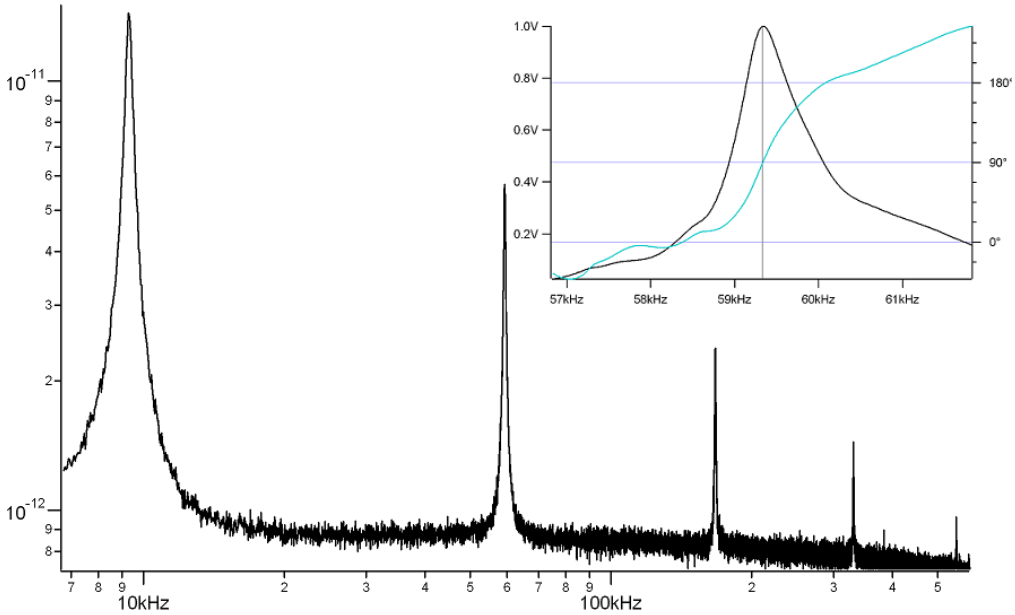

Figure 6.22: Thermal spectrum of 3rd FIB tailored MFM tip showing the first 4 mechanical modes. Inlet shows details of fine tuning at 2nd resonance frequency.

f_1	9.323	kHz
f_2	59.341	kHz
k_2	0.15	N/m
Q_2	95.8	-
f_3	167.339	kHz
k_3	0.59	N/m
Q_3	200.7	-
L	$473.6 \cdot 10^{-6}$	m
AmpInvols	561.32	nm/V
t_{coating}	120	nm
w_{coating}	400	nm
l_{coating}	1.5	μm
Substrate	Si_3N_4	-

Table 6.3: Properties of cantilever and section of nickel coating attached on the 3rd tip are listed.

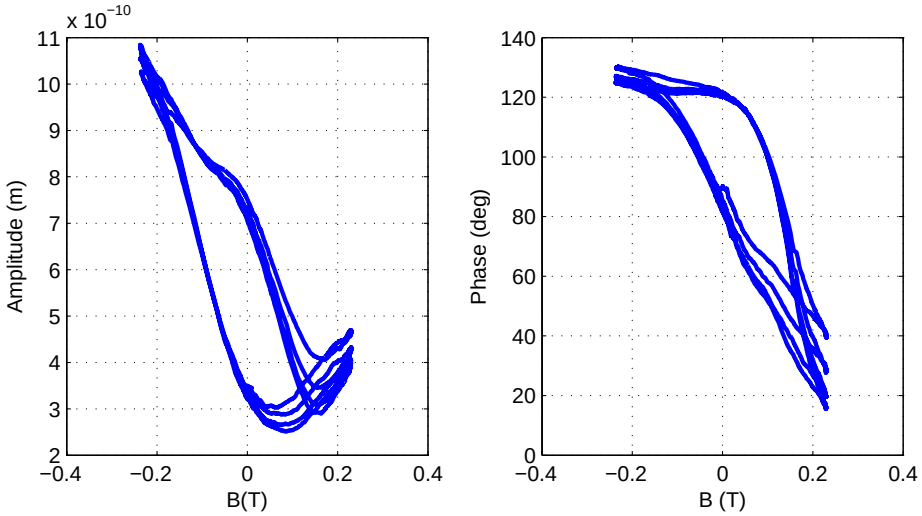

Figure 6.23: Amplitude and phase versus B magnetic field graphs for the first resonance mode of 3rd FIB tailored tip.

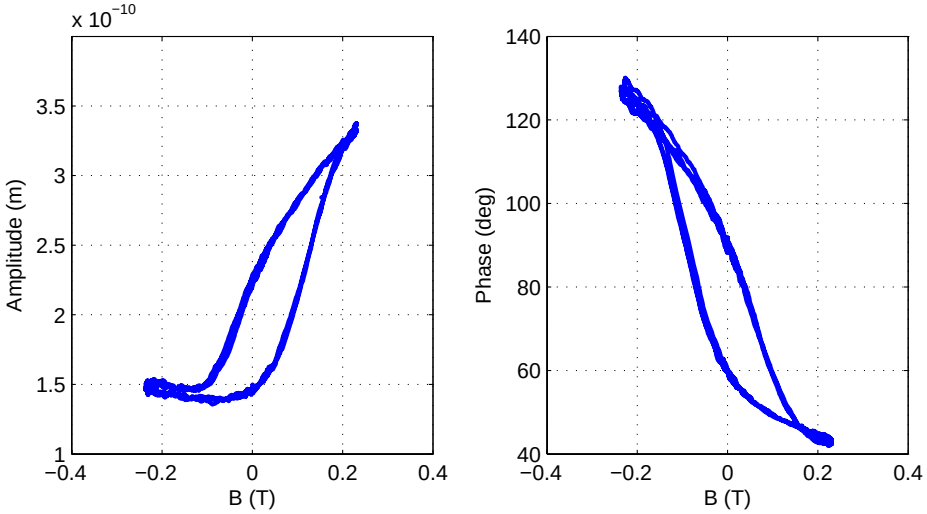

Figure 6.24: Amplitude and phase versus B magnetic field graphs for the second resonance mode of 3rd FIB tailored tip.

was found later that even bare silicon cantilever (without Al coating) had also some magnetic amplitude and phase response detectable on the same order of magnitudes (see in Fig.6.25). So a further study on the subject is required. To solve the observed problem micron size coils only for the magnetic characterization can be used in the future. As a complementary information amplitude and phase vs. magnetic field graphs for the cantilever coated with low coercivity material (permaloy) is given in Fig. 6.26. It is worthy to note that first and second modes cantilever datas of 3rd tip have some symmery property as mentioned in simulations results before.

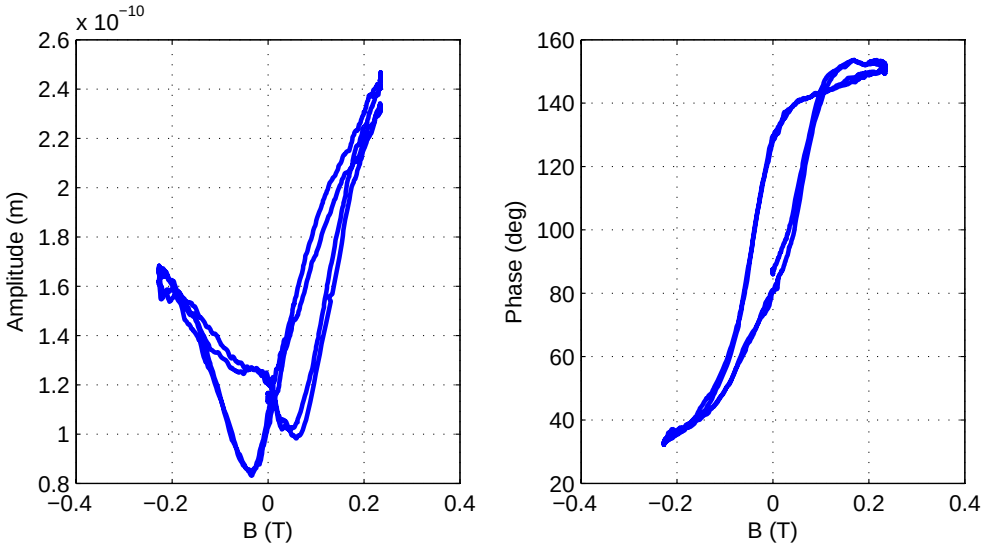

Figure 6.25: Amplitude and phase versus B magnetic field graphs for the normal bare silicon tip.

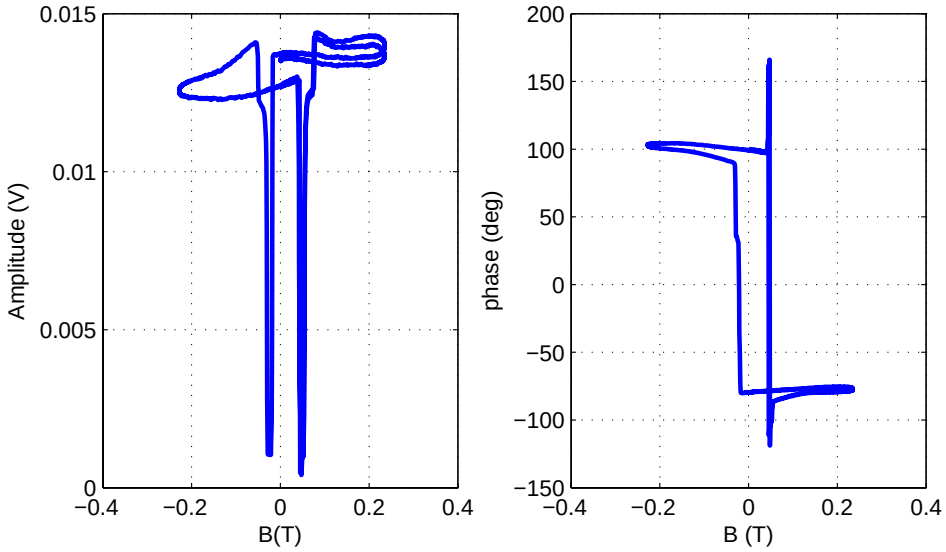

Figure 6.26: Amplitude and phase versus B magnetic field graphs for the cantilever coated with low coercivity material, permaloy. 180^o reversal of magnetization can be seen on the phase curve.

6.3 Multifrequency MFM Imaging with Fluxgate Principle

Experimental setup we used for multifrequency MFM is shown in Fig: 6.27. In this multifrequency imaging method 1^{st} resonant flexural mode is used for topography signal acquisition and 2^{nd} resonant flexural mode is used for measuring magnetic field interaction simultaneously. A sinusoidal voltage signal is applied to shake piezo at the frequency f_1 of the fundemantal mode of cantilever, and a vertical AC magnetic field at frequency f_2 is used for applying torque on the nickel partice. Outputs of two lock-in amplifiers are then fed into user inputs of controller, and then topograpy and magnetic images of sample are constructed by the commercial software of the AFM system.

Before conducting multi-frequency experiments conventional two pass lift-off methode was used in order to obtain topograpy and magnetic image on a harddisk sample. Results can be seen in Fig. 6.28 and Fig. 6.29. As a first observation convolution of tip with surface is seen because FIB tailored tip is not sharp enough,

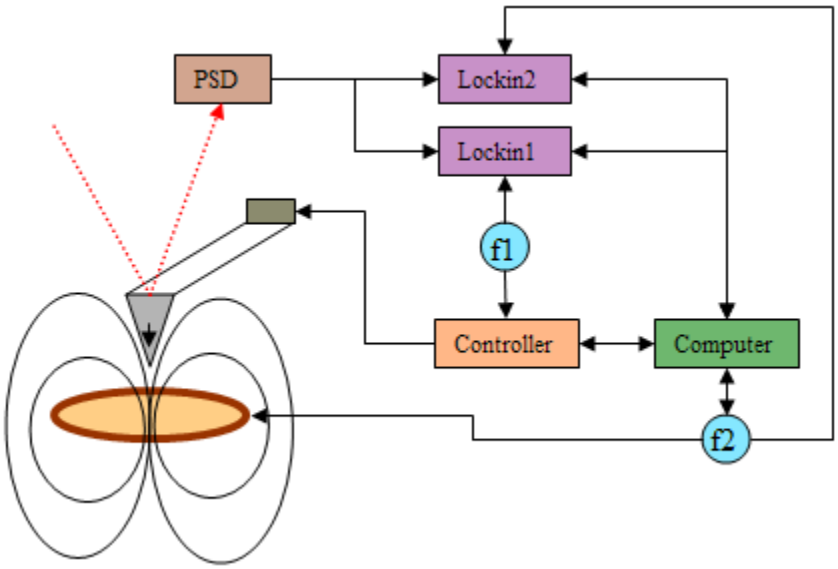

Figure 6.27: Experimental setup used for multi-frequency MFM.

but nevertheless a good magnetic contrast of bit patterns can be obtained.

For the multifrequency imaging a modulating magnetic field B_{AC} of frequency 891.2 kHz, i.e. at 2^{nd} resonance frequency of the first cantilever was applied as the amplitude and the phase of AC deflection signal were being fed into the MFM software for the construction of the images. Coupling of magnetic interaction with topograpy signal can be seen in Fig. 6.30. Images of the amplitude and the phase of 2^{nd} resonance frequency signal are seen in figures Fig. 6.31 and Fig. 6.32.

The strength of topographical coupling to magnetic image was observed to increase as we decreased the amplitude setpoint parameter or increased the driving force of tip at 1^{st} resonance frequency. On the other hand the strength of magnetical coupling to topography was observed to increase as the strength of magnetic field was increased. It seems possible to decrease coupling between signals if optimum parameters for the amplitude setpoint, the driving force and the magnetic field strength of modulation are chosen. Also bandwidth (BW) of the feedback loop keeping the setpoint amplitude constant for topograpy acquisition may be reduced or a cantilever having higher frequency for 2^{nd} resonance mode may be chosen to improve the decoupling of signals.

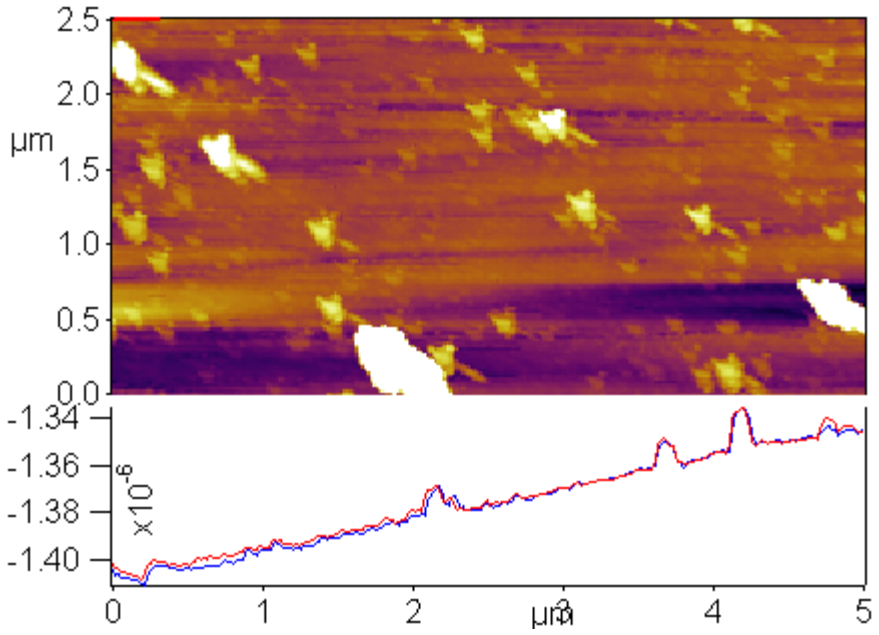

Figure 6.28: Topograpy of a harddisk surface was taken with 1st FIB tailored tip. Convolution of the tip with the sample surface can be seen as a rabbit ear like shapes on the dust particles. Red and blue curves are the profiles of forward and backward scans of the same line, respectively.

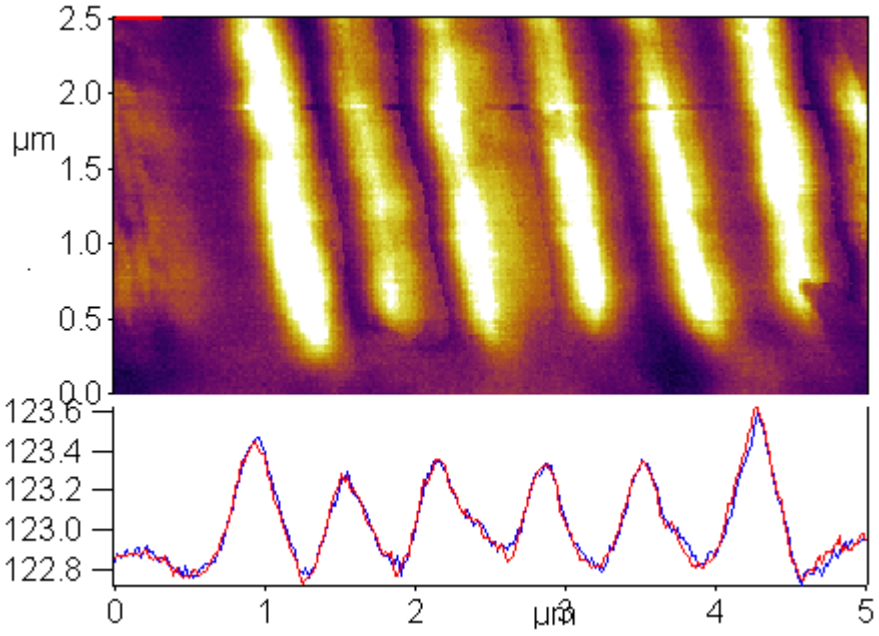

Figure 6.29: Image showing magnetic bit patterns on the harddisk surface was taken with 1st FIB tailored tip with conventional two pass lift-off methode. Red and blue curves are the profiles of forward and backward scans of the same line, respectively.

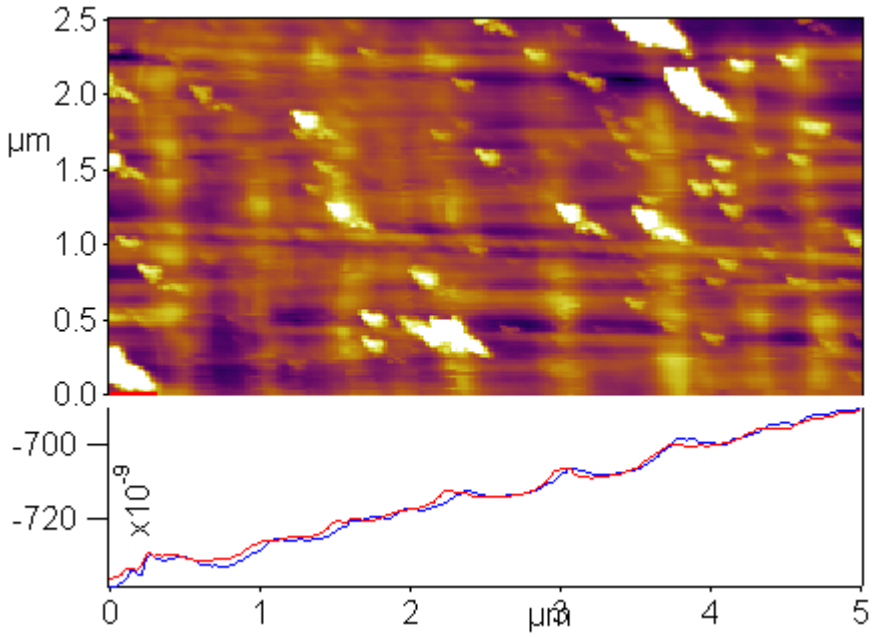

Figure 6.30: Topograpy of a harddisk surface was taken while magnetically modulating FIB tailored tip at 2nd resonance frequency f_2 (showing coupling effect of the magnetic interaction). Red and blue curves are the profiles of forward and backward scans of the same line, respectively.

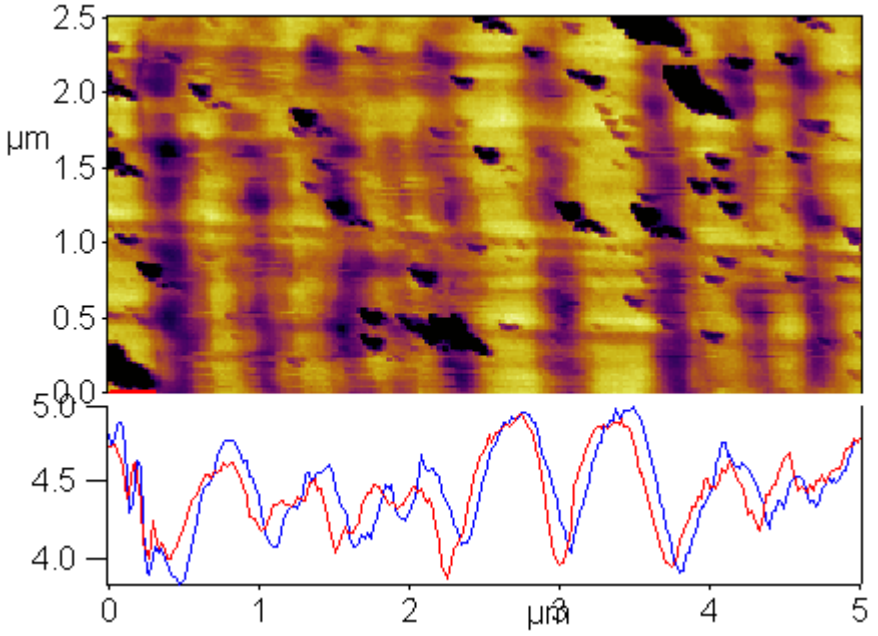

Figure 6.31: Amplitude image of the signal at 2nd resonance frequency f_2 (showing topographical coupling as dark areas). Red and blue curves are the profiles of forward and backward scans of the same line, respectively.

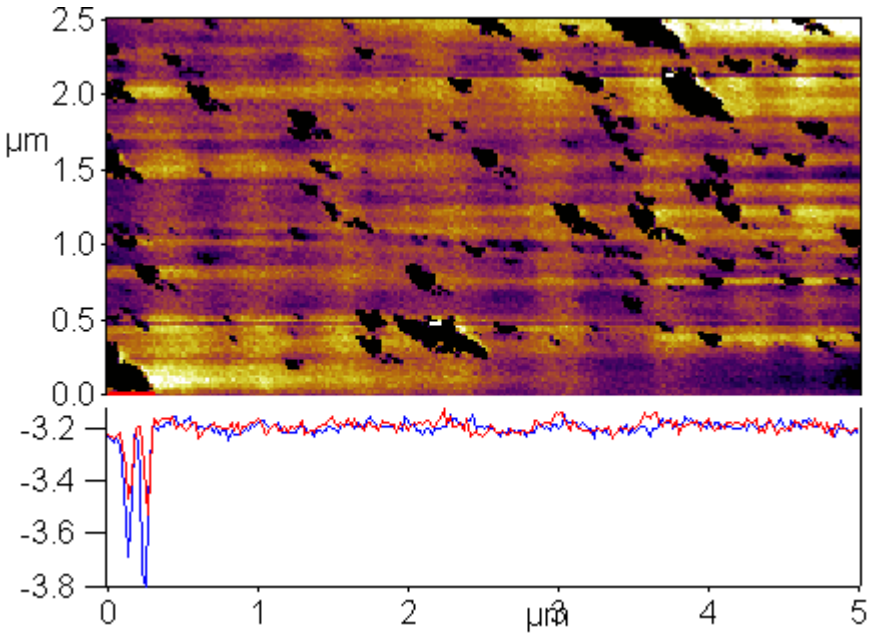

Figure 6.32: Phase image of the signal at 2nd resonance frequency f_2 (showing topographical coupling). Red and blue curves are the profiles of forward and backward scans of the same line, respectively.

Chapter 7

Conclusions and Future Work

As stated in the Introduction Chapter of this thesis, there are two intrinsic problems of MFM, i.e. apriori unknown magnetization of cantilever tips and coupling of magnetic forces with other short and long range forces of tip-sample interaction. In addition to these mentioned problems the conventionally applied two pass lift-off technique of MFM using tips coated with magnetic materials suffers from topographical artifacts, thermal drifts and characteristic dependance on calibration samples. Therefore an alternative technique called multifrequency fluxgate MFM is aimed to developed in this thesis.

At first simulations based on the coherent rotation theory of single domain magnetic particles were made, and dynamics of magnetization reversal and hysteresis were studied. Then a methode of FIB system used for TEM sample preperation was developed to attach submicron magnetic particles on the apex of the cantilever tips and specifically used to fabricate MFM tips with desired size of nickel particles. Nickel particles used for the magnetic interactions were especially cut out from the surface of evaporated nickel films. Using thin films as a source of magnetic material for MFM tips has two fold advantage. Firstly compositional and structural analysis of the thin films can be made using EDAX, TEM and XRD techniques (we used EDAX and TEM). Secondly before or after the evaporation of films on appropriate substrates thermal treatment for crystallization can be made and magnetic annealing processes to control or to improve magnetic

properties can be applied. We used as-evaporated nickel films. It is also possible that using conventional methode of MFM magnetic domain patterns of thin films can be observed beforehand and then used for the determination of the location of target section to be cut. We believe that fabrication of an ideal tip for MFM can be accomplished in this way.

For the characterization of FIB tailored tips a variant of cantilever magnetometry was used. Driving the cantilever using AC magnetic field of 5-10 Gauss in a slowly changing horizontal magnetic field, amplitude and phase responses were measured and then compared to simulations. But a reasonable agreement could not be established. It was found later that even for the cantilevers without any magnetic coating or attached magnetic particles, a magnetic reponse of same order of magnitude occurs. Magnetic effect of the bare silicon cantilevers can not be ignored so a further study on the subject is needed.

Multifrequency imaging of magnetic interactions simultaneously with the acquisition of topography was experimentally demonstrated. Resonance frequencies of the 1^{st} and 2^{nd} flextural modes were used as different source channels. Coupling strengths of the signal can be adjusted changing setpoint parameters of MFM system and the strenght of the magnetic field used for modulation. For a true fluxgate measurement of local magnetic fields, magnetic particles having sizes near superparamagnetic limit ($radius < 70nm$) are needed because high currents must be applied in order to create magnetic field values enough to reverse magnetization of the high anisotropic particle attached. This poses some experimental difficulties such as cooling and perturbation on the magnetization of sample under investigation. As known every experimental technique has drawbacks of its own.

Recently combination of the spectroscopic resolution of MR with the spatial resolution of AFM gave birth a new technique called Magnetic Resonace Force Microscopy (MRFM) which has potential of 3D imaging of atoms in molecules and even single nuclear spin detection. Fluxgate principles can also be used with these resonance techniques to improve their abilities. A fluxgate mechanism dependent on nuclear spins would be very exciting.

Since exchange forces responsible of spin ordering are short range forces, measurement of these forces as in Magnetic Exchange Force Microscopy needs new technological improvements. Fabrication of new special MFM tips can be used to probe these interactions. Even as a read out for quantum computing, i.e qubits new variants of MFM can be considered and implemented.

Bibliography

[1] S. Foner. Versatile and sensitive vibrating-sample magnetometer. *Rev. Sci. Instruments*, 30:536, 1959.

[2] Y. Martin and H. K. Wickramasinghe. *Appl. Phys. Lett*, 50(20), 1987.

[3] L. Harriot H. F. Hess H. L. Loa J. Kao R. E. Miller A. M. Chang, H. D. Hallen and T. Y. Chang. *Appl. Phys. Lett*, 62:1974, 1992.

[4] A. Amar R. C. Black A. Mathai F. C. Wellstood, Y. Gim. *IEEE Trans. Appl. Supercond.*, 7(2), 1997.

[5] J. S. Best D. A. Thomson. *IBM J. Res. Develop*, 44(3), 2000.

[6] S. D. Sarma I. *Žutić*, J. Fabian. *Rev. Mod. Phys*, 76(2), 2004.

[7] J. L. Garbini S. Chao, W. M. Dougherty. *Rev. Sci. Instrum.*, 75:1175, 2004.

[8] C. F. Quate G. Binnig and C.Gerber. *Phys. Rev. Lett.*, 56:930, 1986.

[9] T. Kebe and A. Carla. *J. Appl. Phys. 3,*, 95(3), 2004.

[10] C. Liu and et al. *J. Appl. Phys.*, 91(10), 2002.

[11] M. Mück U. Hartmann T. Öddenhenrich, H. Lemke and C. Heiden. *Appl. Phys. Lett.*, 57:24, 1990.

[12] K. Kjoller Q. Zhong, D. Inniss and V. B. Elings. *Surf. Sci.*, 290, 1993.

[13] T. D.Stowe T. W. Kenny B. C. Stipe, H. J. Mamin and D. Rugar. Magnetic dissipation and fluctuations in individual nanomagnets measured by ultrasensitive cantilever magnetometry. *Phys. Rev. Lett.*, 86(13):2874–2877, Mar 2001.

[14] E. Straver. *Cantilever-based Measurements On Nanomagnets and Superconductors*. PhD thesis, University of Stanford, 2004.

[15] J. R. Lozano and R. Garcia. *Phys. Rev. Lett.*, 100:76102, 2008.

[16] R. Prokscha and et al. *Appl. Phys. Lett.*, 69(17), 1996.

[17] F. Primdahl. *J. Phys. E: Sci. Instrum*, 12:241, 1979.

[18] G. Bertotti. *Hysteresis in magnetism : for physicists, materials scientists, and engineers*. Academic Press, San Diego, 1998.

[19] C. Kittel. *Introduction to solid state physics*. John Wiley and Sons, Inc., 8 edition, 2005.

[20] R. C. O'Handle. *Modern magnetic materials, principles and applications*. John Wiley and Sons, Inc., 2000.

[21] D. J. Griffiths. *Introduction to electrodynamics*. Prentice Hall, New Jersey, 1999.

[22] B. M. Moskowitz. *Hitchhiker's Guide to Magnetism*. Institute for Rock Magnetism, 1991.

[23] M. Barthelme. *Magnetic force microscopy and micromagnetic simulations on domains of structured ferromagnets*. PhD thesis, University of Hamburg, 2003.

[24] A. H. Morrish. *The Physical Principles of Magnetism*. Wiley, New York, 1965.

[25] N. Pilet. *The Relation Between Magnetic Hysteresis and the Micromagnetic State Explored by Quantitative Magnetic Force Microscopy*. PhD thesis, University of Basel, 2006.

[26] P. Escudier. *Ann. Phys.*, 9(3):125–173, 1975.

[27] J. Crangles. *The magnetic properties of solids.* Edward Arnold, 1977.

[28] F. J. Giessibl. *Rev. Mod. Phys*, 75(3), 2003.

[29] O. Sahin and et al. *Phys.Rev.B*, 69(16), 2004.

[30] Magnetic force microscopy: Quantitative results treatment. Technical report, NT-MDT.

[31] V. M. Muller B.V. Derjaguin and Y. P. Toporov. *J. Colloid. Interf. Sci.*, 53:314, 1975.

[32] J. Honeyman and R. Proksch. *Variable Field Module (VFMTM) theory, applications, installation and operation.* Asylum Research Co.

[33] B. Bhushan and H. Fuchs. *Applied Scanning Probe Methodes 2.* Springer, 2006.

[34] H. Benaroya S. M. Han and T. Wei. Dynamics of transversly vibrating beams using four engineering theories. *J. Colloid. Interf. Sci.*, 225(5):935–988, 1998.

[35] S. D. Solares and G. Chawla. Dual frequency modulation with two cantilevers in series: a possible means to rapidly acquire tipsample interaction force curves with dynamic afm. *Meas. Sci. Technol.*, 19, 2008.

[36] Asylum Research Co. *Bimodal Dual AC Imaging.*

[37] U. Bostanci M. K. Abak, O. Aktaş and A. Dâna. Nanoscale charging hysteresis measurement by multifrequency electrostatic force spectroscopy. *Appl. Phys. Lett*, 92:093108, 2008.

[38] M. Radmacher E. Florin and B. Fleck. *Rev. Sci. Instrum.*, 65(3), 1993.

[39] A. K. Sinensky and A. M. Belcher. *Nanotechnology*, 2, 2007.

[40] T. R. Rodriguez and R. Garcia. *Appl. Phys. Lett*, 84(3), 2004.

[41] J. E. Lenz. A review of magnetic sensors. *IEEE Proceedings.*, 78(6), 1990.

[42] F. Primdahl. The fluxgate magnetometer. *J. Phys. E: Sci. Instrum*, 12, 1979.

[43] F. Primdahl. The fluxgate mechanism, part i: The gating curves of parallel and orthogonal fluxgates. *IEEE Trans. Magnetics.*, 6(2), 1970.

[44] D. I. Gordon and R.E. Brown. Recent advances in fluxgate magnetometry. *IEEE Trans. Magnetics.*, 8(1), 1972.

[45] Brown University, Department of Physics. *A simple fluxgate magnetometer*, 2006.

[46] P. Kabos M. Löhndorf, J. Moreland and N. Rizzo. Microcantilever torque magnetometry of thin magnetic films. *J. Appl. Phys*, 87(9), 2000.

[47] C. Rossela and et al. Active microlevers as miniature torque magnetometers. *J. Appl. Phys*, 79(11), 1996.

[48] R. Fainchtein J. A. Marohna and D. D. Smith. An optimal magnetic tip configuration for magnetic-resonance force microscopy of microscale buried features. *Appl.Phys.Lett.*, 73(25), 1998.

[49] N. E. Jenkins T. Nga Ng and J. A. Marohn. Thermomagnetic fluctuations and hysteresis loops of magnetic cantilevers for magnetic resonance force microscopy. *IEEE Trans. Magnetics.*, 42(3), 2006.

[50] R. C. Hibbeller. *Mechanics of Materials*. Prentice Hall, 1991.

[51] K. J. Bruland D. Rugar O. Züger S. Hoen J. A. Sidles, J. L. Garbini and C. S. Yannoni. Magnetic resonance force microscopy. *Rev. Mod. Phys.*, 67(1):249–265, Jan 1995.

[52] H. Schmidt. Magnetization reversal by coherent rotation in single-domain magnets with arbitrary anisotropy. *J. Appl. Phys*, 93(4), 2003.

[53] Asylum Research Co. $MFP-3D^{TM}$ *Atomic Force Microscope Installation and Operation Manual*.

Appendix A

Matlab codes for simulations

A.1 The Simple Model

```
%%%%%%%%%%%%%%%%%%%%%%%%%%%%%%%%%%%%%%
function [deg,R,A]=magShake(B)
%need a function of B field as an input
%deg=pahse of oscillation
%R=Amplitude
%A angle between easy axis and eq. magnetic moment

invols=1/(602*1e-9);%Volt/m
uo=4*pi*1e-7;
Ms=0.52*1e6;%0.6/uo;

a=330e-9;%Lx
b=330e-9;%Ly
c=1000e-9;%Lz
V=a*b*c;
%[Dx,Dy,Dz]=rectDemagFactors(a,b,c);%for rect. particles,(not included).
%Keff=(1/2)*uo*Ms^2*(Dy-Dx)%Uniaxial for rectangular
```

```
%for elisoidal particles
V=(4/3)*pi*a*b*c*5;
r=c/a;
dc=(1-r*asin(sqrt(1-r^2))/(sqrt(1-r^2)))/(1-r^2);
da=(1-dc)/2;
Keff=(1/2)*uo*Ms^2*(da-dc)*2;

k=10;%N/m Spring constant
L=150e-6;%length of cantilever
Leff=L/1.5;
Ldeff=L/1.377;
Q=200;%quality factor
Oeq=11*pi/180;%initial tilt of cantilver

%for 3D visualization
%[Bp,phi] = meshgrid(-2500e-4:10e-4:2500e-4, -pi:pi/1000: pi);
%u=-Bp.*Ms.*V.*sin(Oeq+sin(2.*phi).*(Keff.*V)./(k.*L.^2)+phi)
%+Keff.*V.*sin(phi).^2
%+Kb.*V.*sin(2.*(phi+Ob)).^2k.*L.^2.*(sin(2.*phi).*(Keff.*V)
% ./(k.*L.^2)).^2./2;
%mesh(Bp,npi2pi(180*phi/pi),u)
%hold on

[A]=findRotAngle(Oeq,Keff,Ms,V,Leff,k,B*1e-4);%find minimums

%For drawing the path of eq. points
%[B,A]=findMinPhases(Oeq,Keff,Ms,V,L,k,Bmax);
%u1=-B.*Ms.*V.*sin(Oeq+sin(2.*A).*(Keff.*V)./(k.*L.^2)+A)
%+Keff.*V.*sin(A).^2
%+k.*L.^2.*(sin(2.*A).*(Keff.*V)./(k.*L.^2)).^2./2;
%plot3(B,npi2pi(180*A/pi),u1,'k','LineWidth',2);
```

```
n=(Keff*V)/k*Leff^2;

%amplitude response
R=Ms.*V.*(5e-4).*abs(sin(Oeq+n.*sin(2.*(A))+A))./(k.*Ldeff)
./sqrt((B*1e-4.*Ms.*V.*sin(Oeq+n.*sin(2.*(A))...
    +A)./(k.*Leff.^2)+1./2./Q.^2).^2+(1-1./2./Q.^2)./Q.^2);

%Phase response
angle=atan(-sqrt(1-1./(2.*Q.^2))./(1/(2*Q)
+Q.*Ms.*V.*B.*1e-4.*sin(Oeq+n.*sin(2.*A)+A)./(k.*Leff.^2)));
deg=npi2pi(180*angle/pi);
%
for i=1:length(deg)
    if(sign(sin(Oeq+n.*sin(2.*A(i))+A(i)))<0)
        deg(i)=180+deg(i);
    end
end
%}

figure
subplot(2,1,1);
plot(R)
subplot(2,1,2);
plot(deg)
%plot(npi2pi(180*A/pi))
%plot(B,R*invols)
%%%%%%%%%%%%%%%%%%%%%%%%%%%%%%%%%%%%%%%%%%%%%%%%%%%%%%%%%%%
function [A]=findRotAngle(Oeq,Keff,Ms,V,L,k,B)
%To find eq. points of energy function

add=pi/1000;
iniAngle=0*pi/180;
A=zeros(1,length(B));
```

```
A(1)=iniAngle;
j=2;
for i=1:1:length(B)-1

    phi=A(j-1);
    val=-B(j).*Ms.*V.*sin(Oeq+sin(2.*(phi))
     .*(Keff.*V)./(k.*L.^2)
    +(phi))+Keff.*V.*(sin(phi).^2)
    +k.*L.^2.*(sin(2.*(phi)).*(Keff.*V)./(k.*L.^2)).^2./2;

    minval1=val;
    phi1=phi;
    minval2=val;
    phi2=phi;

    while(1)
        phi1=phi1+add;
        val=-B(j).*Ms.*V.*sin(Oeq+sin(2.*(phi1))
         .*(Keff.*V)./(k.*L.^2)+phi1)
        +Keff.*V.*sin(phi1).^2
        +k.*L.^2.*(sin(2.*(phi1)).*(Keff.*V)./(k.*L.^2)).^2./2;
        if(val<=minval1)
            minval1=val;
        else
            phi1=phi1-add;
            break;
        end
    end
    while(1)
        phi2=phi2-add;
        val=-B(j).*Ms.*V.*sin(Oeq+sin(2.*(phi2))
         .*(Keff.*V)./(k.*L.^2)+phi2)
        +Keff.*V.*(sin(phi2).^2)
```

```
        +k.*L.^2.*(sin(2.*(phi2)).*(Keff.*V)./(k.*L.^2)).^2./2;
        if(val<=minval2)
            minval2=val;
        else
            phi2=phi2+add;
            break;
        end
    end
    if(minval1<=minval2)
        A(j)=phi1;
    else
        A(j)=phi2;
    end

    j=j+1;

end;
```

A.2 The General Model

```
%%%%%%%%%%%%%%%%%%%%%%%%%%%%
function [theta]=findEqPoints(Bdc,phiS,thetaS
,phiC,thetaC,K1,K2)

invols=1/(561.32*1e-9);%Volt/m
a=120e-9;%Lx
b=400e-9;%Ly
c=1500e-9;%Lz
V=a*b*c;
%[Nc,Nb,Na]=rectDemagFactors(a,b,c);(Not included)
%Nc+Nb+Na=1
```

```
Ms=0.52*1e6;%0.6/uo;
k=0.15;%N/m (k)
L=474e-6;
Leff=L/1.50;
Ldeff=L/4.788;%1.377;
Q=95.8;
Oeq=11*pi/180;
%{
phiS=0*pi/180;
thetaS=0*pi/180;%Shape axis
phiC=10*pi/180;
thetaC=0*pi/180;%Crystal axis
K1=-35*1e3;Cubic anisiotropy constants
K2=0*-2.3*1e3;
%}
Bac=5e-4;%Tesla

mphi=zeros(size(Bdc));
mtheta=zeros(size(Bdc));
theta=zeros(size(Bdc));

tminDir=0;
eqP=0*pi/180;eqT=0*pi/180;
t=0:pi/10:2*pi;

for i=1:length(Bdc)
    r=1*pi/180;
    while(1)
        Eeq=totalEnergy1(eqP,eqT,Oeq,Ms,V,Leff,k,Bdc(i)
        ,Na,Nb,Nc,phiC,thetaC,phiS,thetaS,K1,K2);
        out=-1;

        for j=1:length(t)
```

```
    E = totalEnergy1(eqP+r*cos(t(j)),eqT+r*sin(t(j))
    ,Oeq,Ms,V,Leff,k,Bdc(i),Na,Nb,Nc,phiC
     ,thetaC,phiS,thetaS,K1,K2);
    if(E<Eeq)
        Eeq=E;
        tminDir=t(j);
        out=1;
    end
    if( out~=1 && E==Eeq )
        out=0;
    end
end

if(out==-1)%all larger

    mphi(i)=eqP;
    mtheta(i)=eqT;

    break;
elseif((out==1))%a low found
    eqP=eqP+r*cos(tminDir);
    eqT=eqT+r*sin(tminDir);

else%escape from saddle point
    break;
    if(r<10*pi/180)
        r=r+pi/180;
    else
        break;
    end

end
```

```
    end
end

mx=sin(mtheta).*cos(mphi);
my=sin(mtheta).*sin(mphi);
mz=cos(mtheta);
%{
figure
plot3(mx,my,mz);%plots trace of moment vector in 3D
hold
plot3(mx,0.5*ones(size(Bdc)),mz,'r');%For projection on xz
%plot3(mx,my,-1.2*ones(size(Bdc)),'m');
grid
xlabel('X');
ylabel('Y');
zlabel('Z');
%}
%

for i=1:length(Bdc)
    if(Bdc(i)==0)
       theta(i)=0;
    else
       theta(i)=-(mz(i).*cos(Oeq)+mx(i).*sin(Oeq))./(mx(i)
       .*cos(Oeq)-mz(i).*sin(Oeq)+k.*Leff.^2
       ./(Bdc(i).*1e-4.*Ms.*V));
    end
end
%
subplot(1,2,1)
R=Bac.*Ms.*V.*abs(mz.*sin(Oeq+theta)-mx.*cos(Oeq+theta))
./(k.*Ldeff)./sqrt((Bdc.*1e-4.*Ms.*V.*(mx.*cos(Oeq+theta)
-mz.*sin(Oeq+theta))./(k.*Leff.^2)...
```

```
      +1./(2.*Q.^2)).^2+(2.*Q.^2-1)./(2*Q.^4));
  plot(Bdc,R*invols);
%figure
%hold
%plot(Bdc*1e-4,R,'r');grid;
subplot(1,2,2)
tanP=-sqrt(1-1./(2.*Q.^2))./Q./(Bdc.*1e-4.*Ms.*V.
*(mx.*cos(Oeq+theta)-mz.*sin(Oeq+theta))
./(k.*Leff.^2)+1./(2.*Q.^2));
P=atan(tanP);
plot(180*P/pi)
%drawnow

%
%%%%%%%%%%%%%%%%%%%%%%%%%%%%%
function [E]=totalEnergy1(mphi,mtheta,Oeq,Ms,V,Leff,k,Bdc
,Na,Nb,Nc,phiC,thetaC,phiS,thetaS,K1,K2)

uo=4*pi*1e-7;
%Direction cosines of m in XYZ
mx=sin(mtheta).*cos(mphi);
my=sin(mtheta).*sin(mphi);
mz=cos(mtheta);

acx1=cos(thetaC).*cos(phiC);
acx2=cos(thetaC).*sin(phiC);
acx3=-sin(thetaC);
acy1=-sin(phiC);
acy2=cos(phiC);
acy3=0;
acz1=sin(thetaC).*cos(phiC);
acz2=sin(thetaC).*sin(phiC);
acz3=cos(thetaC);
```

```
%Direction cosines of m in crystal unisotropy axis.
alf1=acx1.*mx+acx2.*my+acx3.*mz;
alf2=acy1.*mx+acy2.*my+acy3.*mz;
alf3=acz1.*mx+acz2.*my+acz3.*mz;

asx1=cos(thetaS).*cos(phiS);
asx2=cos(thetaS).*sin(phiS);
asx3=-sin(thetaS);
asy1=-sin(phiS);
asy2=cos(phiS);
asy3=0;
asz1=sin(thetaS).*cos(phiS);
asz2=sin(thetaS).*sin(phiS);
asz3=cos(thetaS);

%Direction cosines of m in shape unisotropy axis.
beta1=asx1.*mx+asx2.*my+asx3.*mz;
beta2=asy1.*mx+asy2.*my+asy3.*mz;
beta3=asz1.*mx+asz2.*my+asz3.*mz;
%
if(Bdc==0)
    theta=0;
else
theta=-(mz.*cos(Oeq)+mx.*sin(Oeq))
./(mx.*cos(Oeq)-mz.*sin(Oeq)+k.*Leff.^2
./(Bdc.*1e-4.*Ms.*V));
end
%}
%Add constant to make energy all positive
%for drawing purposes only
KC0=0;%*(0.333*V*abs(K1)+0.037*V*abs(K2));
KS0=abs(Bdc)*1e-4.*Ms.*V*0;
```

```
%Energy U to be minimized....
E = KS0-Bdc*1e-4.*Ms.*V.*(cos(Oeq+theta).*mx-sin(Oeq+theta)*mz)...
   +(V.*uo.*Ms.^2/2).*(Na*(beta1).^2+Nb*(beta2).^2
   +Nc*(beta3).^2)...
   +KC0+K1.*V.*(alf1.^2.*alf2.^2+alf3.^2.*alf2.^2
   +alf3.^2.*alf1.^2)
   +K2.*V.*(alf1.^2.*alf2.^2.*alf3.^2)...
   +k.*(Leff.*theta).^2/2;


%%%%%%%%%%%%%%%%%%%%%%%%%%%%%%%
```